1-1-2011

Design and fabrication of a prototype aluminum nitride-based pressure sensor with finite element analysis and validation

Xinyu Du
Wayne State University,

Recommended Citation

Du, Xinyu, "Design and fabrication of a prototype aluminum nitride-based pressure sensor with finite element analysis and validation" (2011). *Wayne State University Dissertations.* Paper 408.

DESIGN AND FABRICATION OF A PROTOTYPE ALUMINUM NITRIDE-BASED PRESSURE SENSOR WITH FINITE ELEMENT ANALYSIS AND VALIDATION

by

XINYU DU

DISSERTATION

Submitted to the Graduate School

of Wayne State University,

Detroit, Michigan

in partial fulfillment of the requirements

for the degree of

DOCTOR OF PHILOSOPHY

2012

MAJOR: ELECTRICAL ENGINEERING

Approved by:

____
Advisor Date

____
Co-Advisor

____

____

____

DEDICATION

I would like to dedicate my dissertation work to my parents, my wife and my sons whose love, moral support, motivation and encouragement has been helping me overcome all the difficulties that I encountered during this work.

ACKNOWLEDGMENTS

I feel very much indebted to my advisors - Dr. Hao Ying and Dr. Gregory Auner for offering me such a wonderful opportunity to carry on my Ph. D. study and for their enlightenment and encouragement throughout my dissertation work. I would like to express my deep appreciation to my committee members, Dr. Mark Cheng, Dr. Robert Erlandson and Dr. Golam Newaz for their valuable advices, scientific investigation and being on my committee.

I would also like to thank Smart Sensors and Integrated Microsystems (SSIM) members who have provided support during my study. It is their mentoring, training, discussion and collaboration that made my student days a fun and rewarding journey. Especially I am obliged to Dr. Guopeng Hu for measurement system setup, Dr. Yuriy Danylyuk for AlN film deposition, Dr. Qianghua Wang and Dr. Jianzeng Xu for PSMBE training, Mr. Bill Funk and Mr. Jason Zakens for clean room facilities training, Dr. Shih-Chia Chang, Dr. Changhe Huang, Dr. Michelle Brusatori and Dr. Joseph Smolinski for their valuable suggestions and help.

I would like to express my appreciations to my current supervisor Dr. Yilu Zhang and other colleagues in GM R&D for their support and encouragement.

Last but not least, I am especially grateful to my wife Yuxiu for all she did for me throughout these years.

.

TABLE OF CONTENTS

LIST OF TABLES

LIST OF FIGURES

CHAPTER 1 INTRODUCTION

1.1 Problem Statement

Since 1985 when the first robot PUMA 560 was employed to place a needle during brain CT biopsy, the surgical robots have become ubiquitous in clinical surgeries [3-4]. During a robotic surgery, the robot holds and moves tools instead of human surgeons. Formally speaking a surgical robot is that “a powered computer controlled manipulator with artificial sensing that can be reprogrammed to move and position tools to carry out a range of surgical tasks” [5]. As a mechanical device the surgical robot possesses numerous advantages over human surgeons including stability, accuracy, precision, reliability and small incision, therefore, is suitable in remote surgeries, minimally invasive surgeries and unmanned surgeries.

Despite of the existing successful clinical applications, however, the interaction, i.e. artificial sensing, between the robot and the patient is still very limited. With the help of various cameras, vision is almost the only feeling that a robot can have. The rigid endoscope camera (e.g. [6]) is a common one used to track the robot motion, monitor the operation process and provide a three dimensional view for surgeons. Although the vision feedback can do some help in complex tasks e.g. tying a suture, lacking of other feedbacks prevents the emergence of autonomous robots evolved from passive robots. For instance tactile and tensile feedbacks are desired by surgeons in a gastrointestinal surgery. Nevertheless by now surgeons can only rely on the video feedback from robots to estimate the tension exerted on the tissue. To avoid the patient’s injury, particular care must be taken with tissue handling [3, 7]. Another example is the minimally invasive surgery where feeling tissue is critical to complete the operation. In references [5, 8] a robot called “Da Vinci” system is developed by Intuitive Surgical Incorporated and employed in minimally invasive ‘closed’ heart surgery whose arm only carries an endoscope while other two arms carry scissors and grippers.

How to let a surgical robot possess realistic sense of feel like our skin is at the forefront of research. In order to imitate the human skin, various signals e.g. the strength of pressure, change of strength, speed and acceleration should be measured. All these signals are then processed with the help of artificial intelligent approaches to restore the tissue’s texture. Accurately measuring these physical signals is the basis of constructing an artificial skin so that a high precision pressure is desirable. In this work we will explore some design and fabrication techniques on an effective pressure sensor which will be installed on our surgical robotic arm in the future.

A pressure sensor is a transducer to convert the imposed pressure quantity to the electrical signal. Currently there exist various types of pressure sensors e.g. piezoresistive sensors [9], capacitive sensors [10], electromagnetic sensors [11], surface acoustic wave (SAW) sensors [12], optical pressure sensors, etc. Among all these types SAW sensors have unique superiorities which include but not limited to competitively low cost, high sensitivity, intrinsically reliability, compact size and fast response in high dynamical environment. For example in [13] a 434 MHz quartz SAW device is employed as a precision pressure sensor. Another successful example is the wireless pressure sensor based on reflective delay line design in [14] where the measurement range is from 0 to 350 kPa. Despite the success of existing pressure sensors, these SAW sensors can’t be directly applied in the surgical robotic application since the surgical robotic arm may bring the sensor into the human body where the sensor have to have the capability to operate in the liquid environment. The SAW mode existing in these sensors is normal to the sensor surface resulting in large attenuation in liquid environment [15]. This intrinsic drawback can be overcome by using SH-SAW dual mode sensor. In the dual mode sensor, a strong shear-horizontal mode is found to coexist with the SAW mode which has the displacement parallel to the sensor surface so that the most energy is reserved even in the liquid environment [2]. This property makes the dual mode device work in an aqueous environment without losing the high sensitivity as the SAW mode device. Recently, a type of dual mode devices based on the piezoelectric material Aluminum Nitride (AlN), have been designed, fabricated and successfully applied it in the application of bacterial sensing [16-17]. As a natural extension, in this work, we will modify and apply AlN-based dual mode sensor in the surgical robotic application.

1.2 The History of SAW Device Development

SAW devices are some tools that utilize surface acoustic wave to generate electrical signal in response to some input quantities e.g. chemical concentrations[18], mass [2, 19], relative humidity [20-21], pressure [13, 22-23], temperature [24] etc. For SAW devices SAW plays an important role that can couple with any media in contact with the surface of the device. This coupling strongly affects the amplitude and velocity of the SAW so that it allows the SAW device to detect the change of input quantities.

SAW mode was firstly discovered by Lord Rayleigh[25] in 1885 (so called Rayleith wave). It is guided along the free surface of a material and decayed rapidly with distance to surface. The wave is nondispersive and involves longitudinal and shear components. The longitudinal component is similar to sound wave in air in which the displacement is parallel to the propagation direction. The velocity depends on material, but typically in the range of 5000 to 10000 m/s [26]. The shear component is like the motion of a violin string in which the displacement is normal to the propagation direction. Generally its velocity is around 3000 to 6000 m/s.

The most common way to generate or acquire SAW is utilizing the piezoelectric material where the mechanical and electrical fields are coupled at the atomic level. There are two SAW-related phenomena intrinsic in piezoelectric materials: direct piezoelectric effect and converse piezoelectric effect. The direct piezoelectric effect is that the material can generate electric potential in response to mechanical stress applied that was demonstrated in 1880 by brothers Pierre Curie and Jacques Curie. The converse piezoelectric effect means that a material produces the stress and strain when an electric field is applied, which was mathematically deducted based on the fundamental thermodynamic principles by Gabriel Lippmann in 1881 [27]. The first application of piezoelectric material is the sonar in 1917 where crystalline quartz (piezoelectric material) is used to generate sound beams. However, the real SAW electronic device was developed in 1965 contributed to the invention of Interdigital Transducer (IDT) by R. M. White and F. W. Voltmer. In [28] White et al. discovered that SAW can be excited and detected efficiently by using comb-like electrodes named IDT placed on the surface of a piezoelectric substrate. This invention makes the SAW device fabrication accomplishable. Thenceforward, a vast amount of effort was put into the research and development of SAW devices and the SAW devices were widely used in electronic circuits as filters, oscillators and transformers [26, 29], e.g. by now all TV receivers have SAW filters.

In the late 1970s, Wohltjen and Dessy [30] designed and applied the SAW delay line device for chemical vapor sensing. For such a sensor SAW is generated and acquired by IDT at each end of the device. The chemical object then can be detected according to the change of the output electrical signal in terms of frequency or phase. More recently, the SAW sensors have been improved significantly and extensively applied to diverse fields due to its small size, low cost, high sensitivity and wide variety of measurement.

There exist variety of piezoelectric materials, natural or manmade each of which possess distinct properties and advantages. A comparison between various materials on piezoelectricity is listed in the Table 1.1. Quartz (crystalline SiO_2) is one of common natural piezoelectric materials[1]. The main advantage of quartz is the low temperature coefficient compared to other common piezoelectric materials. The price is relatively low due to its widespread usage. The crystallographic orientations generally have ST cut for SAW devices and AT or BT cut for TSM resonators [1, 31]. Lithium Niobate ($LiNbO_3$) is another widely used piezoelectric material. Its electromechanical coupling coefficient is much larger than quartz though the temperature coefficient is larger too. $LiTaO_3$ and $Li_2B_4O_7$ are piezoelectric materials with high speed phase velocity [32]. Gallium Arsenic (GaAs) is a material suitable for integrated circuit but the electromechanical coupling coefficient is relative small. Zinc Oxide (ZnO) and Aluminum Nitride (AlN) are two particular materials for SAW sensors with thin film structure. ZnO has relatively high electromechanical coupling coefficient and widely used in the field of ultrasonic transducers [33-34]. However, the film always exhibits the electrical conductivity due to the presence of zinc or lattice defects [35].

Table 1.1 The comparison between various piezoelectric material on wave velocity, mechanical properties and piezoelectric coefficients [1].

Substrate (Substrate Cut)	*v* (m/s)	K^2 (%)
Quartz (ST, X)	3158	0.11
Lithium Niobate (-Y, Z)	3488	4.8
Gallium Arsenide (Z, X+22.5°)	2763	0.022
ZnO	3000	0.4
AlN (C)	5740	0.25

Piezoelectric Material	Elastic Matrix (10^{11} Pa)						Piezoelectric Matrix				Permittivity Matrix		Density kg/m^3
	C_{11}	C_{12}	C_{13}	C_{14}	C_{33}	C_{44}	e_{31}	e_{33}	e_{15}	e_{22}	ε_{11}	ε_{33}	
Lithium Niobate	2.03	0.57	0.75	0.09	2.42	0.6	0.2	1.3	3.7	2.5	39	20.4	4647
ZnO	1.57	0.89	0.83		2.08	0.38	-0.51	1.22	-0.45		7.35	7.79	5270
AlN	4.1	1.49	0.99		3.89	1.25	-0.58	1.55	-0.48		9	11	3257

AlN is a semiconductor piezoelectric material and competitive in SAW sensing applications for its intrinsic properties. AlN on a-Al_2O_3 substrate has high SAW velocity (5910 m/s), moderate electromechanical coupling coefficient (around 1.0%) and linear temperature coefficient [17, 36-37]. In undoped state, AlN performs as an insulator (electrical resistivity 1013 ohm·cm), therefore it was employed in a metal-insulator semiconductor structure in some hydrogen sensing applications [38-39]. AlN is also a good candidate for the sensing application that requires operation in extreme conditions because it has the largest energy bandgap among the III-V nitrides (6.2 eV comparing to silicon 1.11 eV, silicon carbide 2.86 eV or gallium arsenide 1.43 eV) [40]. In solid state physics, the band gap is regarding to the energy difference (in electron volts) between the valence band and the conduction band [41]. Generally a large band gap material, greater than 3 eV, can be regarded as the insulators. Some other properties of AlN are shown in Table 1 [42-45].

Table 1.2 The List of AlN Basic Properties

Structural Properties	Density (g/cm^{-3})	3.257
	Modulus of Elasticity (GPa)	331
	Elastic Constant (GPa) C_{11}	410±10
	Elastic Constant (GPa) C_{12}	149±10
	Elastic Constant (GPa) C_{13}	99±4
	Elastic Constant (GPa) C_{33}	389±10
	Elastic Constant (GPa) C_{44}	125±5
	Poisson's Ratio	0.22
	Common Crystal Structure	Wurtzite
	Lattice constant (Å)	a = 3.112 c = 4.982
	Hardness (Kg/mm^2)	1100
	Water Absorption	None
Optical Properties	Density of States Conduction Band (cm^{-3})	4.1×10^{18}
	Effective hole mass	$m_{hz} = 3.53\ m_0$ $m_{hx} = 10.42\ m_0$
	Density of states V band(cm^{-3})	4.8×10^{20}
	Optical phonon energy (meV)	113
	Refractive index (vis-ir)	~2.15
Electrical Properties	Breakdown field (V/cm)	$1.2\text{-}1.8\times10^{6}$
	Mobility electrons holes (cm^2/VS)	135 /14
	Dielectric constant (static/high frequency)	8.5-9.14/4.6-4.84
	Energy Band Gap (eV)	6.13-6.23
	Resistivity (Ohm·cm)	1013
Thermal Properties	Thermal conductivity (W/mK)	175
	Thermal expansion (20-400°C)	$(4.2\text{-}5.3)\times10^{-6}$
	Debye temperature (K)	980
	Melting Point (°C)	2200
Piezoelectric	Coupling Coefficient (C/m^2) e_{15}	-0.33~-0.48
	Coupling Coefficient (C/m^2) e_{31}	-0.38~-0.82
	Coupling Coefficient (C/m^2) e_{33}	1.26-2.1
	Relativity Permittivity Coefficient ε_{11}	9

	Relativity Permittivity Coefficient ε_{22}	9
	Relativity Permittivity Coefficient ε_{33}	11

1.3 The Scope and Contributions of This Work

By considering aforementioned materials and techniques, naturally, an AlN-based SAW device becomes our main interest in the robotic pressure sensor application. The success of the bacteria sensing application using AlN-based SAW devices [2] also indicates its possibility and prospects. Therefore, in this work, a prototype AlN based pressure sensor will be designed and fabricated.

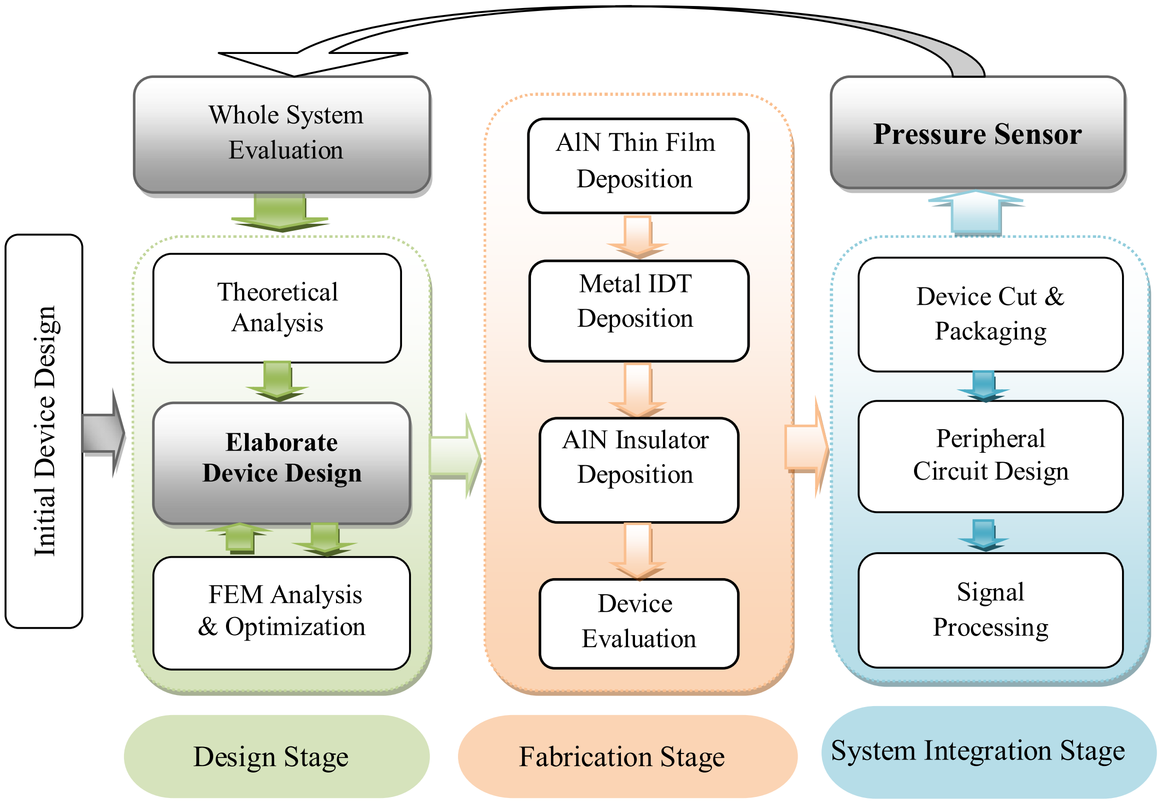

Fig. 1.1 The flow chart of development process for a prototype AlN-based pressure sensor

This work adopts the development process shown in Fig. 1.1. Firstly, the fabrication technique for previous AlN dual mode sensor will be reviewed, modified and applied in the novel pressure sensor design. Since the sensor works in the aqueous environment, the electrical isolation will be the main concern in the design process. In addition the theoretical derivation and analysis are performed to qualitatively verify the whole design. In order to achieve the quantitative analysis, the finite element method (FEM) will be studied and implemented with the software Comsol Multiphysics®. Two-dimensional (2D) and three-dimensional (3D) FEM simulation will be conducted. Based on these verification results the practical AlN-based SAW device will be fabricated in our SSIM clean room. In order to test and calibrate the AlN based pressure sensor, a prototype measurement system will be set up in this work. Different detection methods will be investigated and compared in terms of system sensitivity, measurement range and thermal stability. Some signal processing algorithms will be developed or revised to realize the system implementation. The relative peripheral circuits will be designed and employed in this work too.

CHAPTER 2 THE DESIGN AND THEORETICAL ANALYSIS OF THE AlN-BASED PRESSURE SENSOR

The proposed pressure sensor consists of three parts: rubber probe, AlN based SAW device and circuit board which are shown in Fig. 2.1. Here the cylinder-like rubber probe is attached to the plastic support which is fixed on the circuit board. It can prevent the hard surface of the device from scratching the body tissue. The gap between the probe and the device surface provides the pressure sensor an adjustable offset which will omit the tiny disturbance and increase the stability of the measurement. The constant contacting area makes the pressure reading only depend on the exerted force therefore more consistent. The AlN-based SAW device can convert the change of pressure exerted on the surface into the change of electrical signal's signature (e.g. frequency, phase, amplitude, etc.). When the device is in contact to the patient's body tissues, the electrical signal out of the device will be changed accordingly. By controlling the motion of robotic arm, the information combining force and speed can be collected and analyzed by the signal processing and machine learning model in the robot or remote controller. The textile or hardness can be thereby extracted. The electrical circuit board is the base of the device as well as provides the functions for excitation signals, conditioning signals and transmitting signals.

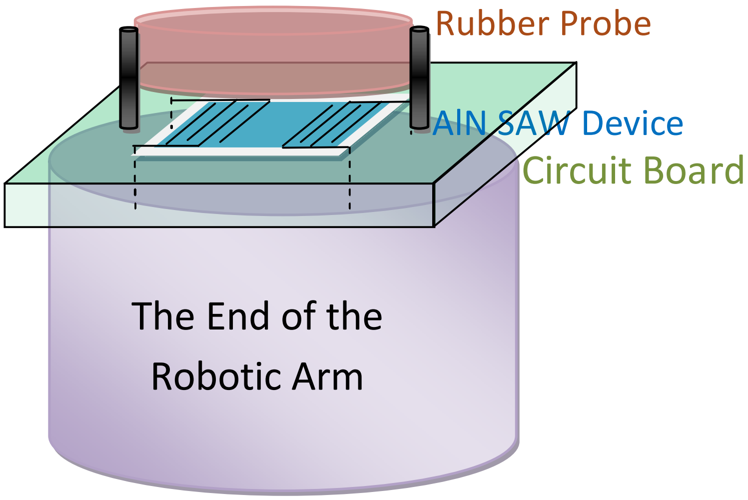

Fig. 2.1 The schematics of a prototype AlN-based pressure sensor

As a core component the AlN SAW device plays an indispensable role in the whole pressure sensor. In this chapter we will provide the detailed information on the SAW device from design to analysis.

2.1 The Structure of the AlN-Based SAW Device

The structure of the proposed AlN-Based SAW device is shown in the Fig. 2.2. This sandwich-like device includes substrate, piezoelectric material, metal IDT and insulator. The root of such design philosophy can be traced back to the 1960’s [46] and it has been proved that with proper design and elaborative fabrication the device can successfully excite and retrieve SAW using other piezoelectric materials (e.g. ZnO [46]).

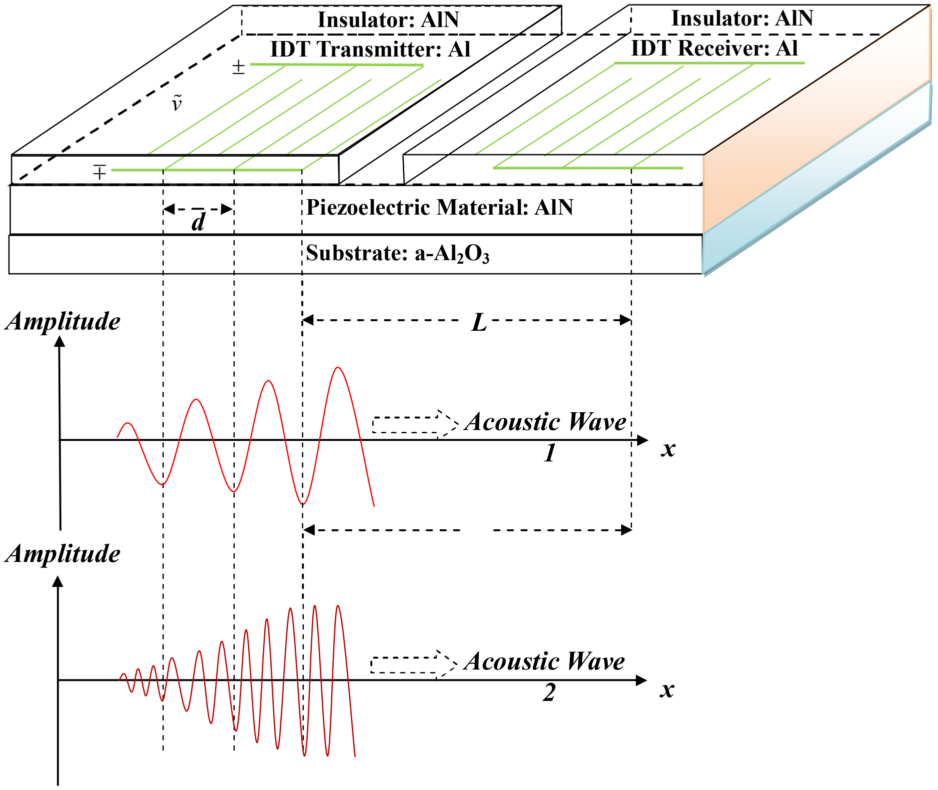

Fig. 2.2 The structure of an AlN-based SAW device and the process of exciting acoustic wave by IDT.

One important reason for selecting such a structure is that AlN has to be crystallized on some substrates in the form of hexagonal Wurtzite [47] (though sometimes occasionally in the form of cubic Zincblende [35]). Here, the crystal or crystalline solid refers to a solid material whose constituent atoms, molecules or ions are arranged in an orderly repeating pattern along all three spatial dimensions. The process of forming a crystalline structure is called crystallization. To be better to illustrate the structure of AlN and its substrate, the Miller indices, notation system in crystallography that will be employed in the rest of this work is briefly described here.

In crystallography, the Miller indices [48] is extensively used to specify planes and directions which includes three integers *l*, *m* and *n* written as (*l m n*). By convention, negative integers are written with a bar, e.g. $\bar{1}$ for -1. All three integers are usually written in the lowest term, i.e. their greatest common divisor should be 1. A plane (*l m n*) means that it intercepts three axes at *l*, *m*, *n*, or some multiple thereof, respectively. The value 0 means the plane do not intersect that axis. For hexagonal structures, a four-index scheme called Bravais-Miller index (*h k i l*) is used to label planes. Here *h*, *k* and *l* are identical to the Miller index, *i* is a redundant index which is equal to –*h*-*k*. For example, the A plane in Fig. 2.3 intercepts x and y axis at 1 and parallel with z axis. Hence, *h* = *k* =1, *i* = -*h*-*k* =-2 and *l* = 0.

The wurtzite structure of AlN has high symmetry compatible with the existence of spontaneous polarization [47]. It generally occurs when the hexagonal layers are stacked in a periodic sequence (..ABAB..). (0001) C plane of AlN is a common direction in most growths for different substrate which have been proved by from the past works in our group [2, 42, 49]. The atoms in C plane AlN are arranged in bilayers consisting of two closely spaced layers where one is with cations and another with anions. Therefore, the surface of AlN may be all nitrogen or aluminum depending on the contacted surface. Note that in an anisotropic solid like AlN the surface-wave velocity depends on the direction of propagation [46].

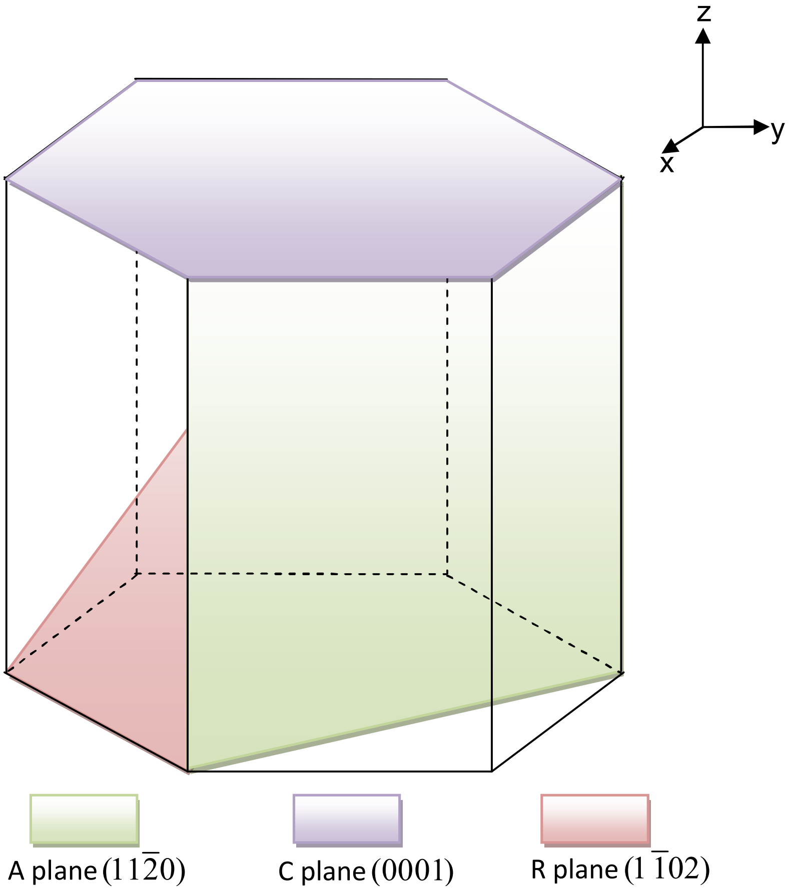

Fig. 2.3 The typical plane orientation in the unit cell of sapphire.

Several substrates can be used for AlN growth, e.g. Si, SiC, GaN, ZnO, MgO, etc. SiC is considered as the best substrate for AlN heteroepitaxy growth since the lattice mismatch with AlN is only 3.5% [50]. Its drawback is the extreme high price ($USD1090 for one 3-inch wafer in 2008). Today sapphire is the most popular substrates for synthesizing heteroepitaxial AlN growth due to the adequate thermal and chemical stability at high growth temperatures, excellent structural and surface morphology and availability in large quantities [47]. Three major orientations of sapphire have been used which are C plane (0001), A plane $(11\bar{2}0)$ and R plane $(1\bar{1}02)$ shown in Fig. 2.3. The crystal orientations of sapphire and AlN are parallel but the lattice mismatch with AlN is about 12%. Note that sapphire is also an anisotropic material [51], therefore, different cut of substrate make the device different. It was found in [16] that the AlN-based device growing on A plane sapphire has the capability to work in aqueous environment due to the existence of SH-SAW mode [17, 49]. Overall our AlN-based SAW device will be grown on A plane sapphire.

As we pointed out in chapter 1, the IDT is the pivotal technique to convert the electrical signal to acoustic wave and convert the acoustic wave back to the electrical signal[1] [28]. The comb-like IDT shown in Fig. 1.2 is generally made from a lithographically patterned metal thin film, e.g. aluminum or gold [1]. The typical thickness is 1000 Å which makes the IDT offer low enough electrical resistance and light mechanical load to the surface. Considering the balance between the electrical resistance and cost, in this work, the aluminum IDT is preferred.

There are two ends for IDT, transmitter end and receiver end. Generally, they are geometrically symmetric. When a radio-frequency (RF) voltage $\tilde{v}$ is connected to the IDT transmitter end, each pair of transducer finger may be considered to be a discrete power source. All fingers on the top side or bottom side have the same electrical potential since they are connected with the same electrode. The piezoelectric substrate underneath the fingers with the same electrical potential will have the same strain. Therefore, an acoustic wave will be generated in the substrate (e.g. acoustic wave 1 shown in Fig. 2.4). The wavelength λ of the acoustic wave is equal to the distance between two adjacent IDT pairs *d* since the wavelength is defined as the distance between consecutive corresponding points of the same phase [52], that is

$$\lambda = d \tag{2.1}$$

The frequency f_0 of the acoustic wave is [52],

$$f_0 = \frac{1}{T} = \frac{v}{\lambda} \tag{2.2}$$

Take (2.2) into (2.1), we have

$$f_0 = \frac{v}{d} \tag{2.3}$$

where v is phase velocity of the acoustic wave about 5740 m/s for AlN which is determined by substrate materials (some materials are listed in Table 1.2 [1] [49]). Since AlN is an anisotropic material, the velocity can be varied along different propagation direction [53]. It is also worth noting that the electromagnetic wave is five orders of magnitude faster than the acoustic wave, the dimension of the device only relying on electromagnetic wave has to be five orders smaller than the acoustic wave device. That is impossible to fabricate using existing photolithography technique.

From the acoustic wave 2 in Fig. 2.2, we can observe that the acoustic wave has not only the frequency f_0 but also has other frequencies (e.g., 3 f_0). However, since we assume the polarity of the two adjacent IDT fingers is opposite, the other frequencies can only be odd times of f_0, that is,

$$f = (2n+1)f_0, \quad n = 0, 1, \cdots, \infty \tag{2.4}$$

Since the metal IDT is conductive, it is necessary to coat an insulator layer over the IDT to make the device working in aqueous environment. Several types of layers including photo resist LOR 1A, LOR 3B and SiO_2 have been employed and compared in [2] where the coating layer is covering the whole area of the device top surface. It was concluded that the insulator layer brings additional attenuation resulting in performance deterioration. In our work, two improvements are made. First the insulator layer does not cover the whole area of the top surface, instead only the IDT and electrodes areas are covered. Second, inspired by the design in [46] where the IDT are placed between the substrate and piezoelectric material in a ZnO-based SAW device, another layer of AlN is coated though such a design brings some technical difficulties due to different melt temperature in AlN and Al IDT which will be shown in the chapter 4.

2.2. The Detailed Geometrical Dimensions and Other Relevant Selections

After determining the structure and material of the device, the detailed geometry should be defined before fabrication. The wavelength λ in this work is selected as 24 μm so that the device operating frequency is around 250MHz. According to Equations 2.1-2.4 and other considerations which will be stated below the dimensions of IDT are chosen as shown in Table 2.1. An intuitive description of the whole device is shown in Fig. 2.2. Note that for better virtualization the size of the plot in Fig. 2.2 is not directly proportional to the real size. In Fig. 2.2 one can observe that the thickness of the substrate is 330 um which is determined by what wafer is in use. The substrate is generally cut as parallelogram which contains the rectangular area of IDT and electrode parts with the width of 3200 um and the length of 11637 um. In order to reduce the edge reflection the substrate shape is cut as not rectangle.

The IDT finger width and distance are determined by the wavelength λ according to equation (2.1). The IDT finger length and the distance between electrodes are selected from the performance consideration. These two parameters determine the IDT aperture. If the aperture is too small, the diffraction loss will be large. On the other hand, the ohmic loss, i.e. the input/output impedance, will be large [54]. A typical value of aperture is 50-80λ [1-2]. The IDT center distance affects the propagation loss. Large distance brings large loss but too small distance may result in electromagnetic feed through. The number of IDT fingers has impaction on passband width, the more, the narrow, that will be shown in Section 2.3 later.

Table 2.1 All the design parameters for AlN-based SAW device

IDT finger width	6 μm
IDT finger length	1680 μm
Distance between two adjacent IDT fingers	6 μm
Distance between transmitter and receiver IDT	3606μm
Electrode width	720μm
Distance between electrodes	1760 μm
Electrode Length (upper/ lower side)	4014/3654 μm
Nμmber of IDT pairs	50 + 50 = 100
Insulator width	3400 μm
Insulator length	4240 μm
Insulator center distance	2650 μm
Insulator thickness	1 μm

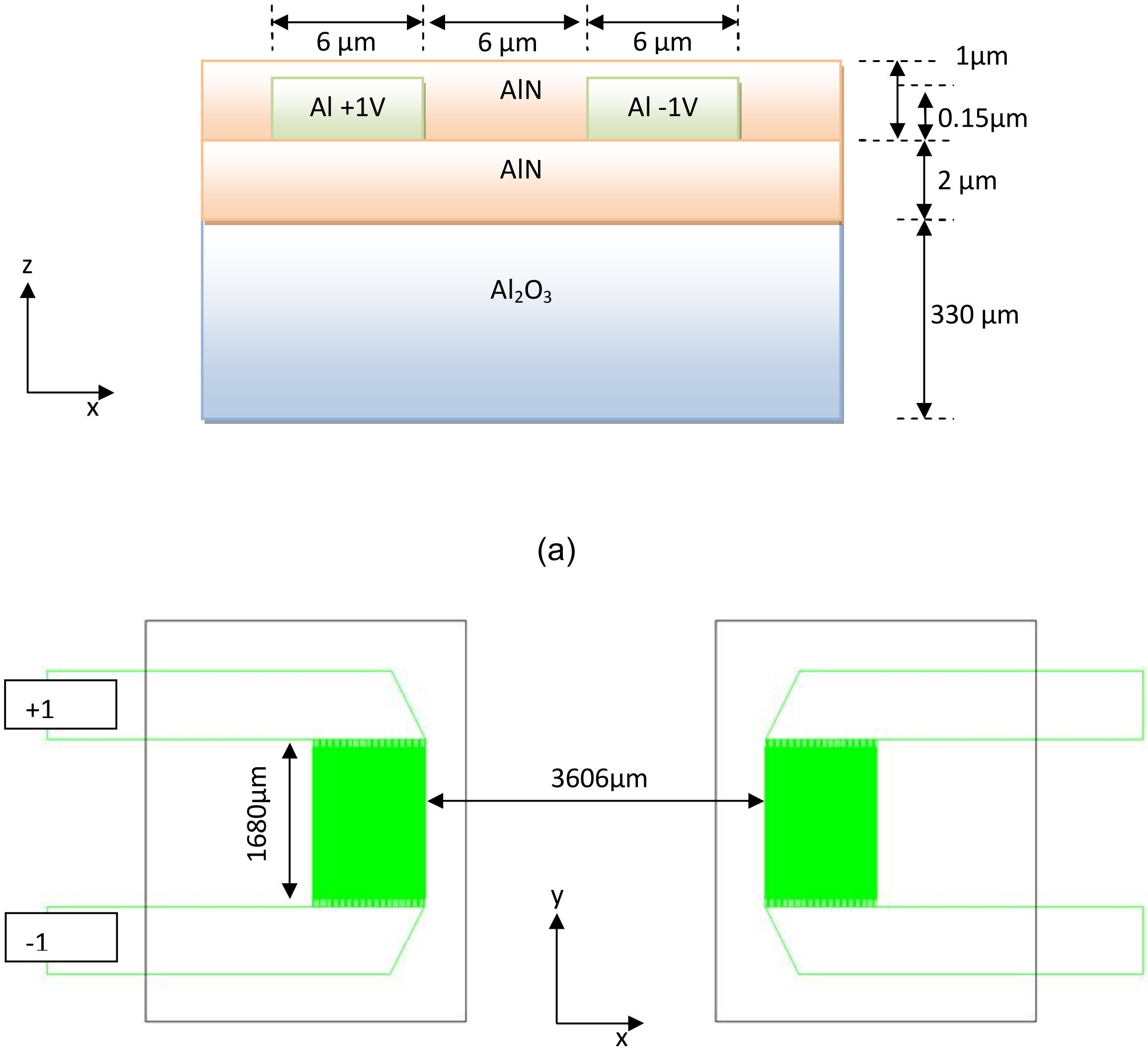

(a)

(b)

Fig. 2.4 The device schematic plots: (a) on x-z plane, and (b) on x-y plane.

In order to enhance the device performance, one modification is made on the original design. Each IDT finger is split into two fingers to reduce the passband ripples [46]. The width of each modified finger becomes half of the original width. The passband ripple is caused by multiple reflections within and between the IDT fingers.

From the previous work on bacterial detection [49], the sensitivity of the AlN-based device is 44 Hz·cm^2/ng for SAW mode and 32 Hz ·cm^2/ng for SH-SAW mode.

The sensing area of the proposed device is 0.4007 cm^2. Therefore the pressure sensor sensitivity is 11.22 kHz/nN and 8.16 kHz/nN for SAW and SH-SAW mode, respectively.

2.3. Delta Function Model Analysis of the Device

The Delta function model is an impulse response analysis. It has been widely applied on different types of SAW devices to achieve qualitative results [55]. Generally, a linear time invariant (LTI) system is able to be characterized completely by its impulse response $h(t)$ since the response to other arbitrary signal for a LTI system can be represented by $h(t)$. Therefore, we derive the impulse response $h(t)$ for a SAW device here, and then obtain its frequency response $H(f)$. In this way, we can investigate the frequency characteristics for a SAW device.

Suppose that an impulse input (+*V*, -*V*) is connected to the IDT transmitter end, each IDT finger will generate an impulse signal with the amplitude A and –A alternatively (shown in Fig. 2.5). The amplitude A is a constant and determined by piezoelectric material and substrate's properties. Note that the impulse inputs can not be (+*V*, 0) since it's contradictive to our assumption that the polarity of two adjacent IDT fingers is opposite. As a result, the output of the IDT transmitter is a series of impulse signal (i.e. SAW) with the period T/2 and amplitude A and -A (Shown in Fig. 2.5). If the number of pairs is equal to *N*, then the last impulse locates at (2*N*-1)*T*. Here the attenuation of amplitude A caused by the substrate is omitted.

Since the impulse response function $h(t)$ is discrete in time, we use $h(n)$ to represent $h(t)$ and the corresponding discrete-time frequency response $H_T(f)$ can be calculated according to the inverse discrete-time Fourier transform equation [56],

$$H_T(f) = \sum_{n=-\infty}^{\infty} h(n) e^{-j\pi nfT}$$

$$H_T(f) = -A \sum_{n=0,2}^{2N-2} e^{-j\pi fTn} + A \sum_{n=1,3}^{2N-1} e^{-j\pi fTn}$$

According to the finite geometric series summation equations, we have,

$$\sum_{n=0,2}^{2N-2} x^n = \frac{1-x^{2N}}{1-x^2}, \; x \neq \pm 1 \qquad (2.5)$$

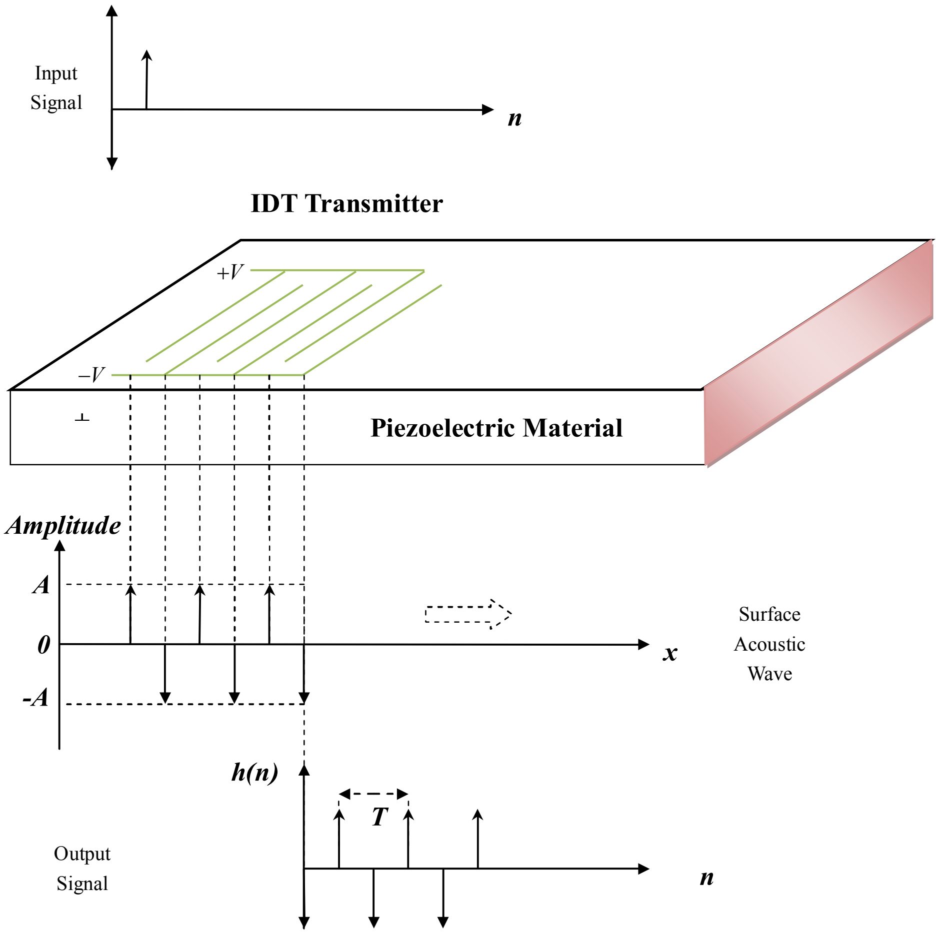

Fig. 2.5 The impulse response of IDT.

$$\sum_{n=1,3}^{2N-1} x^n = x\frac{1-x^{2N}}{1-x^2}, \quad x \neq \pm 1 \tag{2.6}$$

Subtract (2.5) from (2.6), we have,

$$\sum_{n=1,3}^{2N-1} x^n - \sum_{n=0,2}^{2N-2} x^n = (x-1)\frac{1-x^{2N}}{1-x^2} \quad = -\frac{1-x^{2N}}{1+x} \tag{2.7}$$

Then we can simplify $H_T(f)$ using (2.7), that is,

$$H_T(f) = -A\frac{1-e^{-2j\pi fNT}}{1+e^{-j\pi fT}}$$

$$H_T(f) = -A\frac{e^{-j\pi NfT}(e^{j\pi NfT} - e^{-j\pi NfT})}{e^{-j\pi fT/2}(e^{j\pi fT/2} + e^{-j\pi fT/2})}$$

Using Euler’s formula,

$$H_T(f) = -Aje^{-j\pi NfT + j\pi fT/2}\frac{\sin(\pi NfT)}{\cos(\pi fT/2)} \tag{2.8}$$

Equation (2.8) describes the frequency response for transmission end. For the receiver end we can obtain the similar result since when an impulse input exists, a series of impulse signal from the output electrode will be detected. Therefore, we have the frequency response for receiver end,

$$H_T(f) = -Bje^{-j\pi NfT + j\pi fT/2}\frac{\sin(\pi NfT)}{\cos(\pi fT/2)} \tag{2.9}$$

where the pattern of the IDT receiver is assumed the same as the transmitter end, and B is a constant depending on the substrate property.

For the central area, we can treat it as a time-delay system (the delay is equal to *L*/*v*) when attenuation is omitted so that is,

$$H_T(f) = e^{-j2\pi fT\frac{L}{v}} \tag{2.10}$$

Considering (2.26), (2.27) and (2.28), the frequency response of the whole IDT is equal to the multiplication of these three parts, that is

$$H_T(f) = -ABe^{-2j\pi NfT + j\pi fT - 2j\pi fTL/v}\left(\frac{\sin(\pi NfT)}{\cos(\pi fT/2)}\right)^2 \tag{2.11}$$

From equation (2.11), we can obtain some important results,

(1) The IDT exhibits a frequency response with sinc function dependence.

As we know the exponential function only affects the phase not magnitude. Therefore, we only need to investigate $\left(\frac{\sin(\pi NfT)}{\cos(\pi ftT/2)}\right)^2$. From the theory of discrete-time Fourier transform, $\left(\frac{\sin(\pi NfT)}{\cos(\pi ftT/2)}\right)^2$ is a periodical form of sinc function. The period is $\frac{2}{T} = 2f_0$ and the peak of magnitude locates at $f_{peak} = (2n+1)f_0$. This result coincides with the previous analysis (2.4).

(2) The bandwidth is inversely proportional to the number of IDT finger pairs.

The bandwidth f_B is generally defined as the width of the nonzero frequency. Therefore just let $\sin(\pi NfT) = 0$, we can have $f = f_0 / N$. Therefore the bandwidth can be calculated as,

$$f_B = 2 f_0 / N \qquad (2.12)$$

This means if we increase the number of IDT finger pairs the bandwidth will become narrower.

(3) The phase delay depends on N, T, L and v. From the exponential item in equation (2.11) we know that if we increase N, T or L or decrease v, the phase delay will be increased.

2.4. Structural Mechanics Analysis of the Device

As we discussed above, the SAW sensor is a class of acoustic wave devices. The input electrical signal excites the acoustic wave by piezoelectric materials, and passes though the device. The acoustic wave is sensitive to the force exhibited on the device and converted to the electrical signal by piezoelectric material. Therefore, to derive the mathematical model of the whole device, the surface acoustic wave propagation should be derived at first.

As an elastic material, either for Al_2O_3 or AlN, the wave equations are determined by the internal stress and strain. The stress inside the body is caused by an applied load on the body exterior. One can imagine that two adjacent blocks inside the body exert the internal force on each other across an imaginary plane of separation. When the force is parallel to this plane it is called shear stress (τ). When the force is normal to it, it is normal stress (σ). The stresses derive from the cohesive nature of the body's material. With the normal stress, the size of an element in a body will be changed which is called simply strain (ε). With the shear stress, the edge angle of an element in a body will be changed which is known as shear strain γ. According to the Hooke's law, the materials which are considered as elastic are governed by the two following equations,

$$\sigma = E\varepsilon \tag{2.13}$$

$$\tau = G\gamma \tag{2.14}$$

Where *E* is Young's modulus and *G* is modulus of rigidity. They are the intrinsic elastic properties for a material [57]. These two equations completely characterize the elastic behavior of a solid in the small deformation limit (strain is less than 10^{-5}).

In the three-dimensional space the normal stress (strain) and shear stress (strain) for any one point in the body will have multiple components as shown in Fig. 2.2. For better presentation, Cauchy stress tensor *T* is used to define all stress components and strain tensor *S* for all strain components which were introduced by Cauchy around 1822 [58], that is,

$$T = \begin{bmatrix} T_{xx} & T_{xy} & T_{xz} \\ T_{yx} & T_{yy} & T_{yz} \\ T_{zx} & T_{zy} & T_{zz} \end{bmatrix}, \quad S = \begin{bmatrix} S_{xx} & S_{xy} & S_{xz} \\ S_{yx} & S_{yy} & S_{yz} \\ S_{zx} & S_{zy} & S_{zz} \end{bmatrix} \tag{2.15}$$

Each component of *T* is denoted by two subscripts, the first denoting the direction of the force and the second denoting the direction of the area. The component of strain S also has two subscripts. If the two subscripts are the same, the stress and strain are the normal stress and strain i.e. the change is perpendicular to the surface. Otherwise, it is a shear stress (or strain) in two different direction indicated by the two subscripts i.e. the change is parallel to the surface.

From Fig. 2.6, it's obvious that T_{xx} , T_{yy} and T_{zz} are normal stress, other components of *T* are shear stress. Since the stress is a measure of the force on each point inside the body, it is defined as the force exerted per unit area [46], that is,

$$T_{ij} = \frac{F_i}{A_j}, i, j = x, y, z , \qquad (2.16)$$

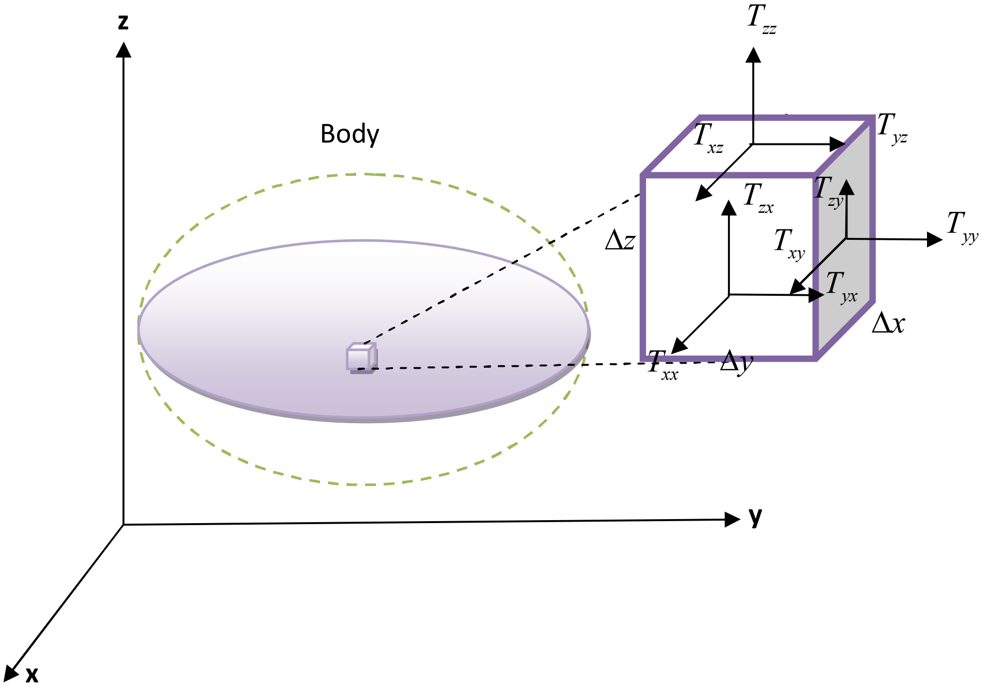

Fig. 2.6 Components of stress in 3D space.

where *A* is the area and *F* is the force. Hence the unit of the stress is Pascal (Pa), which is equivalent to N/m^2.

It's worth noting that the stress only on three surfaces needs to be calculated. That's because the stress on other 3 surfaces (the opposite one) can be directly obtained from the stress on these 3 surfaces in the neighbor cubic (element) according to the Newton's third law. Furthermore, the stress tensor is symmetrical in most cases according to the angular momentum conservation law [59]. From Fig. 2.3, we have four shear stresses making the element rotating about the center in x-y plane.

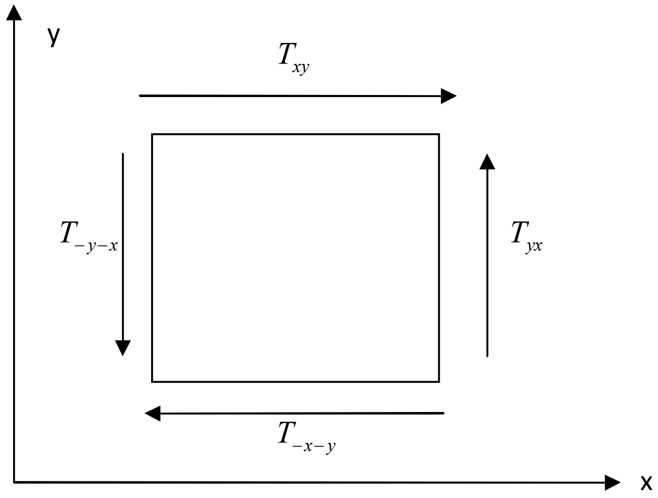

Fig. 2.7 The shear stress in x-y plane.

Based on Newton's second law,

$$M = I\alpha$$

where *M* is the total torque, *I* is the inertia moment and α is the angular acceleration. If the element side length is equal to *h*, that is,

$$\Delta x = \Delta y = \Delta z = h$$

we have

$$
\begin{aligned}
M &= \sum_{i=1}^{4} F_i \frac{h}{2} \\
&= \sum_{i=1}^{4} T_i \frac{h^3}{2} \\
&= \frac{h^3}{2}(T_{xy} - T_{yx} + T_{-x-y} - T_{-y-x})
\end{aligned}
$$

While the inertia moment is related to the element mass (density) by [59],

$$I = \frac{\rho h^5}{6}$$

we have

$$(T_{xy} - T_{yx} + T_{-x-y} - T_{-y-x}) = \frac{\rho h^2}{3}\alpha$$

Since the acceleration can not be infinitely large, when the element side length tends to 0, we can conclude that $T_{xy} = T_{yx}$. $T_{-x-y} = T_{-y-x}$ can be achieved from the neighbor element as we discussed above. Analogously, we have [59-62],

$$T_{xy} = T_{yx}, T_{xz} = T_{zx}, T_{yz} = T_{zy}. \tag{2.17}$$

Note that the equation (2.17) holds for our application but it does not hold true for all the cases, e.g., the presence of couple-stresses or the continuum is a non-Newtonian fluid which will cause the rotationally non-invariant fluids.

Similarly, the strain describes how much deformation differs from the initial state. Therefore, it is related to the displacement by [63-64],

$$S_{xx} = \frac{\partial \mu_x}{\partial x} \tag{2.18) (a}$$

$$S_{yy} = \frac{\partial \mu_y}{\partial y} \tag{b}$$

$$S_{zz} = \frac{\partial \mu_z}{\partial z} \tag{c}$$

$$S_{xy} = S_{yx} = 0.5(\frac{\partial \mu_x}{\partial y} + \frac{\partial \mu_y}{\partial x}) \tag{d}$$

$$S_{xz} = S_{zx} = 0.5(\frac{\partial \mu_x}{\partial z} + \frac{\partial \mu_z}{\partial x}) \tag{e}$$

$$S_{yz} = S_{zy} = 0.5(\frac{\partial \mu_y}{\partial z} + \frac{\partial \mu_z}{\partial y}) \tag{f}$$

where *u* is the displacement. From the equations above, the differential value provides the deformation change at any point. When the deformation change is uniform in the whole body it becomes a division i.e. μ_x / x. For shear strains, the strain value is equal to the average of two deformation change in two directions parallel to the surface. For example, the shear strain on surface *z* is equal to the average of deformation change from the *y* axis in the *x* direction (because it may be different in *x* direction) and the deformation change from the *x* axis in the *y* direction. Note the strain is a ratio therefore it does not have a unit.

We can rewrite the strain-displacement relation (2.18) into matrix form,

$$S = \frac{1}{2}(\nabla u + (\nabla u)^T)$$

where the gradient of a vector

$$\nabla u = \begin{pmatrix} u_x \\ u_y \\ u_z \end{pmatrix} \begin{pmatrix} \frac{\partial}{\partial x} & \frac{\partial}{\partial y} & \frac{\partial}{\partial z} \end{pmatrix} = \begin{pmatrix} \frac{\partial u_x}{\partial x} & \frac{\partial u_x}{\partial y} & \frac{\partial u_x}{\partial z} \\ \frac{\partial u_y}{\partial x} & \frac{\partial u_y}{\partial y} & \frac{\partial u_y}{\partial z} \\ \frac{\partial u_z}{\partial x} & \frac{\partial u_z}{\partial y} & \frac{\partial u_z}{\partial z} \end{pmatrix}. \tag{2.19}$$

and the second term $(\nabla u)^T$ is the transpose of ∇u.

From the symmetry property of both tensors *T* and *S* discussed above, one can observe that only 6 components are independent out of original nine. This is the reduced subscript notation (engineering notation):

$$T_1 = T_{xx}, S_1 = S_{xx} \tag{2.20}$$

$$T_2 = T_{yy}, \; S_2 = S_{yy}$$

$$T_3 = T_{zz}, \; S_3 = S_{zz}$$

$$T_4 = T_{yz} = T_{zy}, \; S_4 = 2S_{yz} = 2S_{zy}$$

$$T_5 = T_{xz} = T_{zx}, \; S_5 = 2S_{xz} = 2S_{zx}$$

$$T_6 = T_{xy} = T_{yx}, \; S_6 = 2S_{xy} = 2S_{yx}$$

Then the Cauchy stress/strain tensor can be represented by Voigt notation:

$$T = \begin{bmatrix} T_1 & T_2 & T_3 & T_4 & T_5 & T_6 \end{bmatrix}^T$$

$$S = \begin{bmatrix} S_1 & S_2 & S_3 & S_4 & S_5 & S_6 \end{bmatrix}^T$$

Hence, the strain-displacement relationship can be rewritten in terms of strain-displacement matrix B since the strain is a vector instead of a tensor.

$$S = B^T u \tag{2.21}$$

where B is,

$$B = \begin{pmatrix} \frac{\partial}{\partial x} & 0 & 0 & 0 & \frac{\partial}{\partial z} & \frac{\partial}{\partial y} \\ 0 & \frac{\partial}{\partial y} & 0 & \frac{\partial}{\partial z} & 0 & \frac{\partial}{\partial x} \\ 0 & 0 & \frac{\partial}{\partial z} & \frac{\partial}{\partial y} & \frac{\partial}{\partial x} & 0 \end{pmatrix}$$

With the Voigt notations of T and S, we can rewrite the Hook's law (2.1) and (2.2) in matrix form which is also called elastic constitutive relation [1],

$$T = CS \tag{2.22}$$

Here the stiffness matrix C has 6×6 = 36 components c_{ij} relating the six components of stress to six strain components. From the principle of conservation of energy, one can obtain [59] that

$$c_{ij} = c_{ji}$$

That means the stiffness matrix have 21 distinct components. The number of independent components can be reduced by taking the crystallographic symmetry of solids into account [65]. If the material is isotropic that means all physical parameters do not depend on the direction, there will be only two independent elastic constants: c_{11} and

c_{44} [66]. If the material is the anisotropic medium (directionally dependant), e.g. sapphire, 7 to 13 independent parameters are required.

In elastic material, e.g. AlN or Sapphire, the wave motion can be described in terms of stress and strain. From the Newton's second law, the net force on a particle is equal to the mass times acceleration, while the acceleration is equal to the second order derivative of displacement *u*. Therefore, for any direction, e.g. *x* direction, we have,

$$F_x = \rho V \frac{\partial^2 u}{\partial t^2} \tag{2.23}$$

where the volume $V = \Delta x \Delta y \Delta z$ and ρ is the density. Considering the relation between force and stress, we have,

$$T_{xx} \Delta y \Delta z + T_{xy} \Delta x \Delta z + T_{xz} \Delta x \Delta y = \rho \Delta x \Delta y \Delta z \frac{\partial^2 u}{\partial t^2}$$

$$\frac{T_{xx}}{\Delta x} + \frac{T_{xy}}{\Delta y} + \frac{T_{xz}}{\Delta z} = \rho \frac{\partial^2 u}{\partial t^2}$$

When the volume tends to 0, we have the equation of motion in *x* direction,

$$\frac{\partial T_{xx}}{\partial x} + \frac{\partial T_{xy}}{\partial y} + \frac{\partial T_{xz}}{\partial z} = \rho \frac{\partial^2 u}{\partial t^2}$$

In the same manner, we have the equation of motion for other two directions. In matrix form, it is

$$\nabla \cdot T = \rho \ddot{u} \tag{2.24}$$

where $\nabla\cdot$ is the divergence operation of second rank tensor.

$$\nabla\cdot T=\begin{pmatrix}\frac{\partial T_{xx}}{\partial x} & \frac{\partial T_{xy}}{\partial y} & \frac{\partial T_{xz}}{\partial z}\\ \frac{\partial T_{yx}}{\partial x} & \frac{\partial T_{yy}}{\partial y} & \frac{\partial T_{yz}}{\partial z}\\ \frac{\partial T_{zx}}{\partial x} & \frac{\partial T_{zy}}{\partial y} & \frac{\partial T_{zz}}{\partial z}\end{pmatrix}$$

In engineering notion it becomes,

$$\rho\ddot{u}=BT$$

Considering the above three equations, we have the elastrodynamic equation,

$$\rho\ddot{u}=BCB^{T}u$$

If we consider the damping in propagation of the wave, we have to change the elastic constitute relation,

$$T=CS+\eta\dot{S} \tag{2.25}$$

The elastrodynamic equation should changed accordingly,

$$\rho\ddot{u}=BCB^{T}u+B\eta B^{T}\dot{u}\,. \tag{2.26}$$

This is the mathematical model of elastic material (e.g. sapphire). When the geometry is complex, it’s difficult to derive the above partial differential equations. The solution can be solved based on some numerical computation methods e.g. finite element method (FEM).

For the piezoelectric material AlN, the mathematical model should contain two more field variables, electric flux density D and electric field intensity E. According to the electromagnetic theory, the quantities D and E are related by material electrical permittivity ε, that is,

$$D = \varepsilon E \text{ .}$$

However, for piezoelectric material where the structure of crystal lacks a center of inversion symmetry [1], the strain changes result in the change of the charge distribution that produces the electrical polarization. This is called direct piezoelectric effect and can be described by,

$$D = eS + \varepsilon E \tag{2.27}$$

where *e* is the piezoelectric stress constant matrix having the unit of charge/(length)2. Similarly, the reversed process, converse piezoelectric effect, is able to be described by,

$$T = CS - e^T E \tag{2.28}$$

where e^T is the transposition of the piezoelectric stress constant matrix indicating the effect on stress by electric field .

(2.27) and (2.28) are called piezoelectric constitute equations. If we consider the quasi-electrostatic approximation,

$$\nabla \times E = 0$$

The electric field E can be expressed as the function of electric potential ϕ , that is[65],

$$E = -\nabla \phi \tag{2.29}$$

According to the Guass's law, the flux density can be expressed as,

$$\nabla \cdot D = \rho_v \tag{2.30}$$

where ρ_v is the charge density and is usually negligible in piezoelectric materials.

Take (2.9) and (2.27) to (2.30) into the equation of motion (2.24), we can erase the variables *E*, *T*, *S* and *D* and obtain the linear differential equations only with respect to *u* and ϕ. To solve these differential equations, two boundary conditions are applied. (1) discontinuity of the electric flux density coincides with the charge distribution on the boundary; (2) continuity of the electric potential [65].

CHAPTER 3 FINITE ELEMENT METHOD-BASED SIMULATIONS AND DESIGN VERIFICATION

3.1 The Basic Theory of Finite Element Method

Finite Element Method (FEM) is a numerical method to solve complicated physical problems with geometry boundary conditions which was introduced in the 1950’s [67-69]. Generally, the problem of interest has the complex geometrical domain where the governing equation is difficult to be solved analytically. One example is our application. With FEM, the whole domain will be divided into some simple sub-domains, e.g. polynomials called finite elements. The algebraic equations are developed using the governing equations of the problem over each finite element. Then all elements are assembled with certain inter-element relationships together [70]. A detailed procedure to solve FEM problems is as follows [70].

The first step is to divide the irregular whole domain into smaller and regular finite elements. There is no unique solution for dividing but different dividing schemes result in different approximation accuracy and different amounts of computational time. Generally the shape, size, location and other configurations for each finite element should be chosen carefully to approximate the domain as close as possible without increasing the computational cost [71]. Mostly the choice of the type of the element coincides with the geometry of the body and the dimensional number. As an example, in the case of stress analysis of the short beam, the three-dimensional solid cube element can be used in this step. The size of the elements influences the accuracy of the solution and computational time. Hence, different sizes of elements are generally used for the whole domain. For a large system, it’s difficult, if not impossible, for an efficient and accurate discretization. Almost all of commercial finite element software can complete this step by build-in automatic mesh programs. The Tessellation and Octree methods [72-74] are the most common method in these software. When the users provide the information on the surface or volume of the material, the automatic mesh generator generates the nodes and elements in the body.

The second step is to choose a simple function for each element to approximate solution. Such a function is called the interpolation function, the approximating function or the interpolation model. Polynomial-type functions have been most widely used in the literature because polynomial function is easier to be differentiated or integrated and it is able to converge to the exact solution. The parameters of interpolation function can be derived from the system equations (e.g. force equilibrium equations) in terms of the nodal values of the elements. Here, nodal points are connecting points between several elements. To converge to the extract solution, the interpolation polynomial needs to satisfy three requirements [75-76] (1) all field variables have to be continuous for each element (e.g. Polynomial functions). (2) All field variables and their partial derivation have to be employed in the interpolation function in the limitation circumstance i.e. the size of all elements is zero. (3) All field variables and their partial derivatives whose order is one less than the highest order have to be continuous at element boundaries.

The third step is to derive the stiffness matrices and load vectors. From the equilibrium conditions or other variation principle, the stiffness matrix and load vector of each element can be derived with three methods. The first one is direct approach which is generally applied in some simple types of elements. The second approach is variation approach. The whole system has to be represented in variation form. The third one is the weighted residual approach. In this method the element matrices and vectors are derived directly from the governing differential equations with Galerkin method or least squares method.

The forth step is to assemble element equations to obtain the overall equilibrium equations. Once the element matrices and vectors are found in global coordinate system, all matrices and vectors can be assembled based on the connection requirement for each element node. This procedure is always the same regardless of the type of problem and the number and type of elements.

The fifth step is to obtain the unknown nodal displacement from the overall equations. Here the governing finite element equations may have three possible scenarios, equilibrium problem, eigenvalue problems or propagation problems. The AlN device model is an application of propagation problems. The propagation problems involves a set of simultaneous linear differential equations which can be solved by any of numerical integration method e.g., Runge-Kutta, Adams-Moulton and hamming methods.

Finally from the known nodal displacements the other variables e.g. element strains, stresses, electrical flux density etc can be computed using the necessary physical equations. In our case, the equations (2.27)-(2.30) may be used to solve these variables.

3.2 The Current Status of FEM Simulations on SAW Devices

In SAW technology, the approximation or simulation the device performance can be done by several methods, e.g. transmission line model [46], equivalent circuit model [77] [78], p matrix method [79], coupling of modes (COM) method[65, 80], finite difference method [81], finite volume method [82], collocation method[83], boundary element method (BEM) [84] and FEM method [85]. FEM has been proved to be a suitable numerical method to derive the influence of geometrical variations of the electrode's shape among these methods.

The first attempt to model SAW propagation using FEM technique can be traced back to 1991[86-87]. A numerical FEM/BEM model is used to carry out the Green's function for the electrical and mechanical response. Sometimes an analytical development of harmonic Green function which is the Fourier transform substitute multiplications by polynomials can be actually calculated. However for a general piezoelectric problem, a double integration of the convolution of the Green's function with various excitations along the surface is required. It is very difficult because of very rapid local variations [88-89].

The similar FEM/BEM mixed simulation can also be found in other references. The leaky SAW devices were simulated and analyzed using 2D FEM in [90]. The FEM is applied to the electrode region to take account of the effect of electrode thickness [91]. BEM was used for the substrate [90]. In 2002, Lin et al. proposed a generalization of FEM/BEM model for multi-electrode-type grating periodic arrays [92]. The electrode is assumed infinitely thin. A mixed FEM/BEM numerical model for the simulation of a periodic array of metallic electrodes was investigated in[93]. The FEM/BEM impedance and power was simulated and analyzed [94] for SH-SAW devices. The IDT thickness from 100 Å to 2000 Å was simulated and agreed with the measured device responses. In [95], the boundary condition of FEM was discussed. The absorbing boundary conditions (ABCs) were used instead of standard boundary condition like Neumann- or Dirichlet conditions.

The FEM simulation not only has shown good agreement with the measurement data, but also precisely predicts the SAW devices' parameters and performance. In [96], the wave propagation parameters and input admittances was accurately predicted by FEM simulation. The phase, attenuation constants, stop-band edges, group and phase velocity can also be simulated. In [97] a 2D FEM simulation was conducted for an AlN/diamond structure. The simulation showed the frequency response and the effect of metallization ratio on the third harmonic response. 3d FEM simulations of vibrations have been successfully applied on a blood vessel [98]. 7198 nodes and 39172 tetrahedral elements are used in the simulations. The diffraction effect was investigated based on the two dimensional angular spectrum of wave method in [99]. The diffraction is the main second order effects which deteriorates stop-band rejection and pass-band ripple.

FEM simulations have been successfully applied in different SAW sensors with various FEM software [100]. The H_2 SAW gas sensor with the structure of $LiNbO_3$ substrate and palladium thin film was simulated by ANSYS® using 3D FEM [101]. Atashbar etc. performed the 3D finite element simulation for a two-port surface acoustic wave delay line sensor on XY $LiNbO_3$ substrate with a palladium thin film [101]. The palladium file is used to absorb H_2 like a sponge. ANSYS® V6.1 was used as the simulation platform. Due to the limitations on the number of nodes that the software can generate, each IDT had 3 finger pairs and the dimensions of the piezoelectric substrate are 104.64 μm in depth and 523.2 μm X 523.2 μm for area. With the simulation the wave propagation mode and velocity can be observed and calculated. The insertion loss of the sensor with/without H_2 was obtained from the impulse response analysis. In [102] , the propagation of laser generated thermoelastic surface acoustic waves was simulated using a multilayered finite element model by ANSYS®. The similar analysis for non-metallic material was conducted in [103-104] . A thin-film structure of ZnO/LiNbO3 device was simulated by software package ANSYS using 3D FEM [107]. The substrate geometry for simulations is 1600LX500DX400W μm and used 72000 elements. The 3 μm thick ZnO layer used 84500 elements. 4 degrees of freedom including displacement in x, y and z planes and voltage was defined for each node. The simulation show good agreement experimental measurements. The software COMSOL Multiphysics® [105] [106] was also used for SAW resonant frequencies simulation. The two-port SH-SAW resonator sensor was simulated using MemMech module in ConventorWare™ [108]. The sensor was fabricated on 64 rotated Y-cut $LiNbO_3$ with the following dimensions 6000μmX820μmX500μm. The IDTs and reflectors were defined using Cr and Au with a thickness of 40 nm and 60 nm respectively. Each IDT end has 8 finger pairs with a periodicity of 40 μm and the acoustic aperture is 700 μm. In the simulation the depth of the substrate is reduced to 100 μm in order to have a finer mesh. There were a total of 65000 elements forming the mesh and the element sizes were 5 μm, 50 μm and 75 μm in the x, y and z directions respectively. The propagation velocity and frequency response were obtained and compared with the measurement. Sanna Harma etc. developed an analytical method [109] to extract he reflection and transmission coefficients by using the output of the software FEMSAW [110]. The energy scattered in to bulk is then formulized as a function of frequency for a $LiNbO_3$ SAW device. The 3D-FEM is applied to an IDT finger overlap in the grating structure. The similar analysis is made in [111].

3.3 2D Simulation for AlN-based SAW Device with COMSOL 4.1

The first FEM software NASTRAN was developed in 1965 by NASA. Nowadays there are a lot of FEM software packages available, commercial or open source, e.g., ABAQUS®, ANSYS®, COMSOL®, FEBuilder®, etc. Considering the functionality, feasibility and price COMSOL Multiphysics® 4.1 is selected as our FEM simulation tool in this work.

In order to simulate the device performance, the most accurate way is to reconstruct the 3D structure of the device with the same design parameters in COMSOL. However, the current computer hardware is unable to provide enough computational capability. Therefore, in this work, we will carry out the simulation in two simplified way: 2D plane strain simulation and 3D simplified model simulation.

Generally, a 3D elastic object can be treated as a 2D plane object with some restrictions and assumptions using either plane strain analysis or plane stress analysis. Plane stress is defined to be a state that one direction of stresses, both normal and shear, are assumed to be zero. Such an assumption occurs when the object is a plane where one dimension is much smaller than other two dimensions. A typical example is the thin plate where its external force is parallel to the plate. Plane strain is defined to be a state that one direction of strains, both normal and shear, are assumed to be zero. This assumption happens when one dimension of the object is much larger than other two dimensions. A representative instance is the water pressure analysis on a dam. The length of the dam is much larger than the section that makes the strain along the length can be omitted. For our applications from the design parameters (Table 2.1) one can observe that the length of IDT finger is much larger than width and thickness. Furthermore based on the analysis in Section 2.3 the surface displacement of SAW happens within the section area of IDT fingers. Hence, the 2D plane strain analysis will be implemented as follows. The computer to run all simulations has one 2.66GHz Intel® Core2 Duo CPU and 3GB memory installed.

3.3.1 FEM simulation for the device without the insulator

When the COMSOL Multiphysics® 4.1 is started up, a new model is selected. From Model Wizard, the options, 2D and piezoelectric devices are chosen. Then in the new model, three parts of the device, IDT, AlN and sapphire are added under Model identifier (shown in Fig. 3.1). The IDT fingers can be added by one rectangle and then expended to 100 pairs by two array operations.

In the material tab, all related materials are added, elastic material Al_2O_3, piezoelectric material AlN and conduct metal aluminum (Fig. 3.2). Each material is assigned to one or more geometries in the tab of geometric scope. Note that the elasticity matrix and piezoelectric constants in the database of COMSOL are slightly different from our desire and therefore will be modified in the material model tabs next.

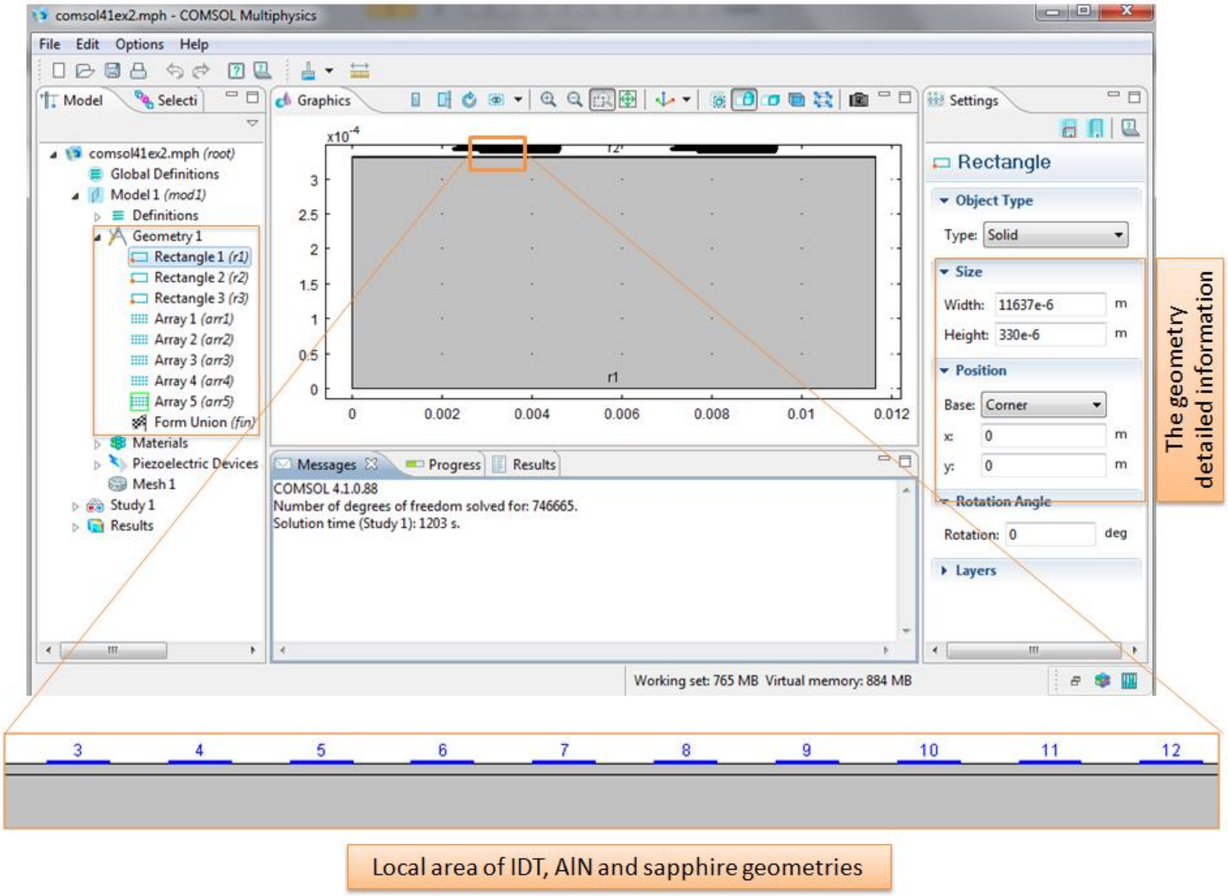

COMSOL 4.1.0.88
Number of degrees of freedom solved for: 746665.
Solution time (Study 1): 1203 s.

Type: Solid

Width: 11637e-6 m

Height: 330e-6 m

Base: Corner

x: 0 m

y: 0 m

Rotation: 0 deg

Working set: 765 MB Virtual memory: 884 MB

Fig. 3.1 The geometry setup for 2D device simulation

In the physics tab, i.e. piezoelectric devices, the plane strain analysis is selected for 2D approximation. The thickness is chosen as the IDT finger length 1680 μm. Three material models are added: Piezoelectric material model, linear elastic material model and linear elastic material model. In the piezoelectric material model, we select the domain for AlN layer. From Fig. 2.3, we select Y-Z plane as the coordinate system. The constitutive relation employs stress-charge form and its associate constant matrices are manually selected (user defined). Although Table 1.1 provides a set of piezoelectric constants, in fact, a variety of different elastic constants are discovered from theoretical [112-118] or experiments [119-123], as well as the piezoelectric constants [124-128].

After numerous trials, the following constants are used in this work. The elasticity matrix is,

$$C_E = \begin{bmatrix} 410 & 140 & 100 & & & \\ & 410 & 100 & & \mathbf{0} & \\ & & 380 & & & \\ & & & 125 & 0 & 0 \\ & * & & & 125 & 0 \\ & & & & & 135 \end{bmatrix} \times 10^9$$

where the constant $C_{66} = \dfrac{C_{11} - C_{12}}{2}$ from the crystal structure and * is the symmetric elements about the diagonal. The coupling matrix is,

$$e = \begin{bmatrix} & \mathbf{0} & & & -0.48 & \\ & & & -0.48 & & \\ -0.58 & -0.58 & 1.55 & & \mathbf{0} & \end{bmatrix} C/m^2$$

The relativity permittivity matrix is,

$$\varepsilon = \begin{bmatrix} 9 & & \\ & 9 & \\ & & 11 \end{bmatrix}$$

and the density is 3260 kg/m^3.

Since the crystal direction of AlN is C plane and the device is parallel to the y-axis (from Fig. 4.4), no further rotation needs to be made on these matrices.

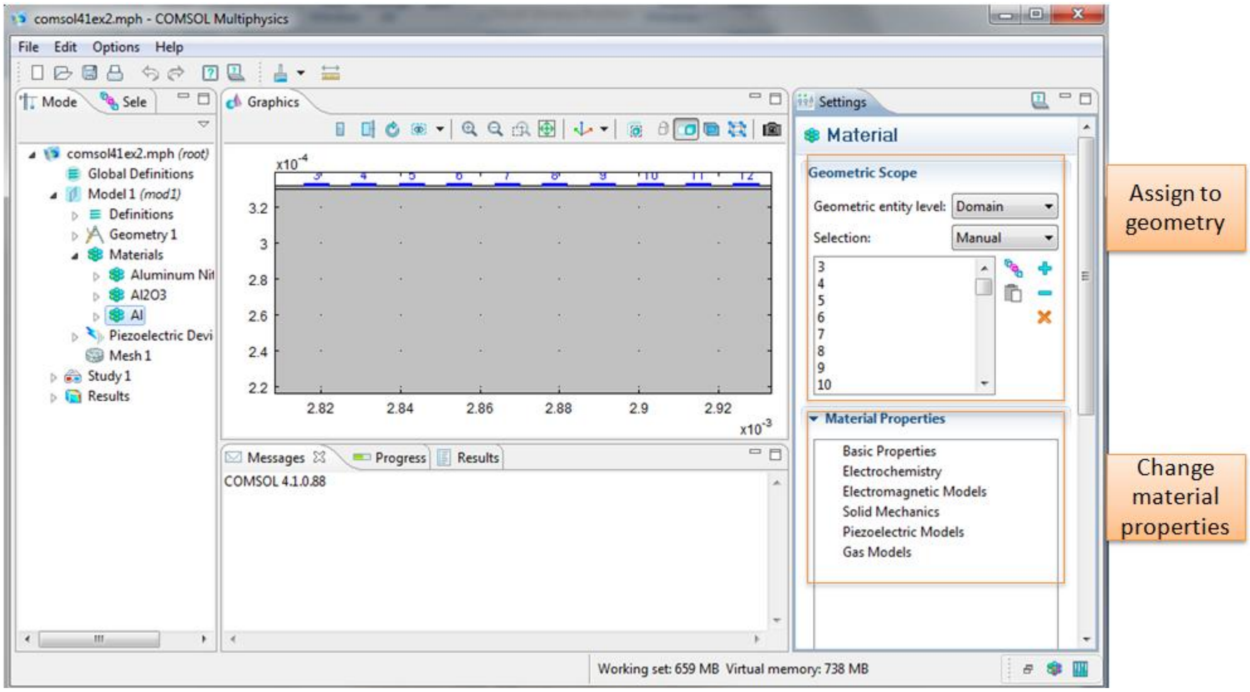

COMSOL 4.1.0.88

Geometric entity level: Domain

Selection: Manual

3
4
5
6
7
8
9
10

Working set: 659 MB Virtual memory: 738 MB

Assign to geometry

Change material properties

Fig. 3.2. Specify material properties for 2D device simulation

In the linear elastic material model 2, the sapphire substrate is selected as the domain. Same as the piezoelectric material, Y-Z plane is employed as the coordinate system. The anisotropic model is selected as per the sapphire property. According to [129], the density is set as 3980 kg/m^3 and the original elastic matrix is defined as follows,

$$D=\begin{bmatrix}496&164&115&&&\\&410&115&&\mathbf{0}&\\&&498&&&\\&&&148&0&0\\&*&&&148&0\\&&&&&166\end{bmatrix}\times10^{9}$$

Since the substrate is A-plane sapphire, i.e. the coordinate axes of the device do not coincide with the material axes, the elasticity matrix D can not be directly input into

COMSOL. A feasible way is to apply Euler angle rotation approach [130-131] to rotate the material axes to the device coordinate. The elasticity matrix is changed accordingly. From Fig. 3.3, one can easily observe that the axes need to be rotated counter clockwise 90 degree about y axis first and 30 degree about z axis to make x-y plane become x''-y'' plane. The elasticity matrix can be obtained from [132] that is,

$$D = \begin{bmatrix} 459.88 & 131.12 & 127.25 & 0 & 0 & -28.36 \\ & 415.88 & 151.75 & 0 & 0 & -9.74 \\ & & 496 & 0 & 0 & 21.22 \\ & & & 161.5 & 7.79 & 0 \\ & * & & & 152.5 & 0 \\ & & & & & 164.13 \end{bmatrix} \times 10^{9}$$

For linear elastic material model 1, no more modification needs to be made except for selecting all IDT fingers as the domain. The material properties are defined through material tabs where the density is 2700 kg/m^3, Young's modulus E is 70 GPa and the Poisson's ratio v is 0.33. It worth noting that the mass of IDT fingers is considered in this work instead of neglected in some references [133-134].

The structural boundary conditions and electric boundary conditions need to be added and defined under the physics, piezoelectric devices shown in Fig. 3.4. Here, we have two structural boundary conditions; fixed constraint which is applied to the bottom boundary due to the device is fixed in the socket and free boundaries which is true for all other boundaries.

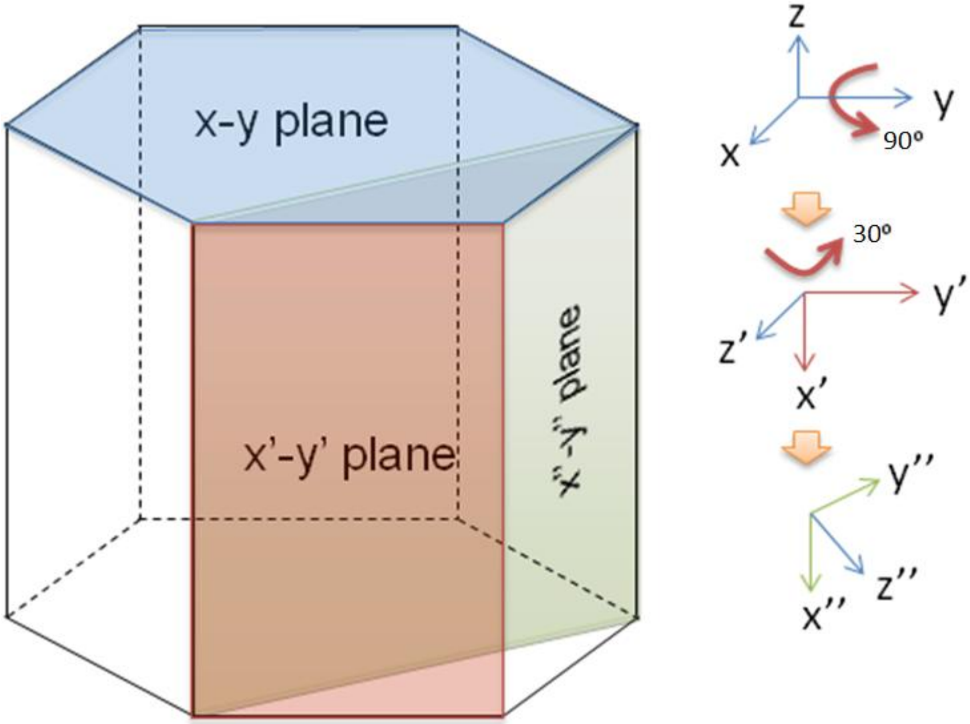

Fig. 3.3 Euler rotation to compute the elasticity matrix for A-plane sapphire

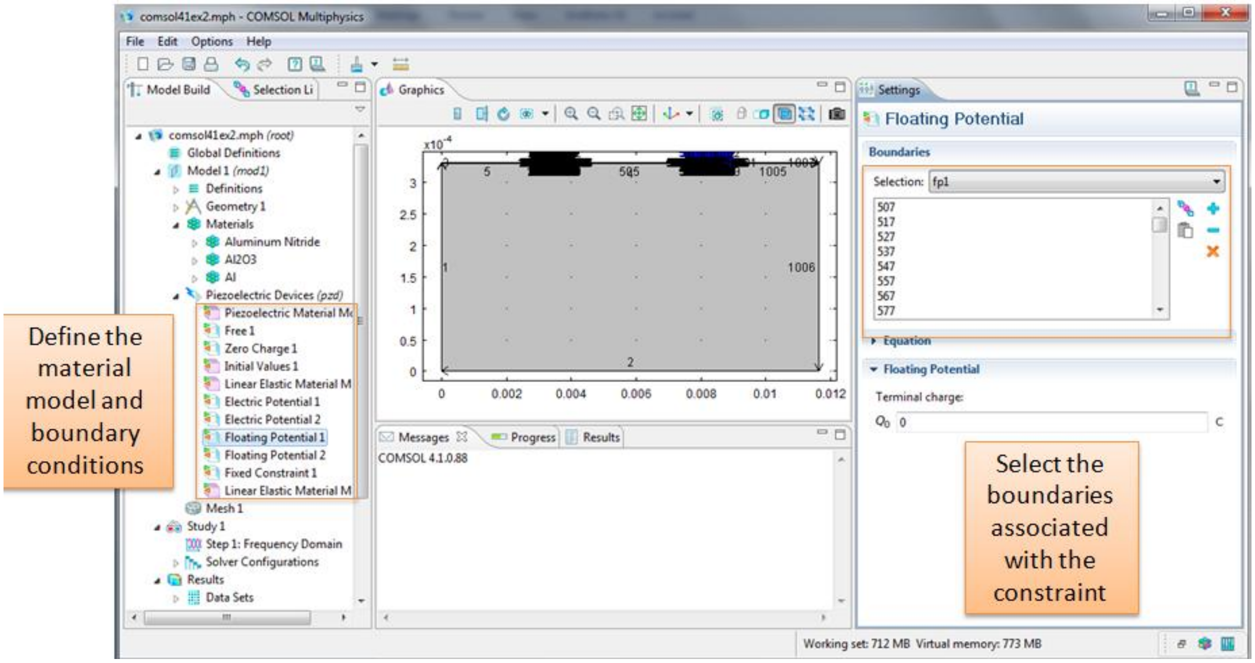

COMSOL 4.1.0.88

Selection: fp1

507
517
527
537
547
557
567
577

Terminal charge:

Q_0 0 C

Define the material model and boundary conditions

Select the boundaries associated with the constraint

Fig. 3.4 Define the boundary conditions and material models

The electrical boundary conditions include electrical inputs: electrical potential 1 and electrical potential 2, electrical outputs: floating potential 1 and floating potential 2, and the zero charge constraint. For each condition, we need to assign the corresponding boundaries. Fig. 3.5 shows that the electrical potential 1 boundaries. The value for electrical potential 1 is set as 1 and the electrical potential 2 is set as -1. For initial values, we set 0 for all variables.

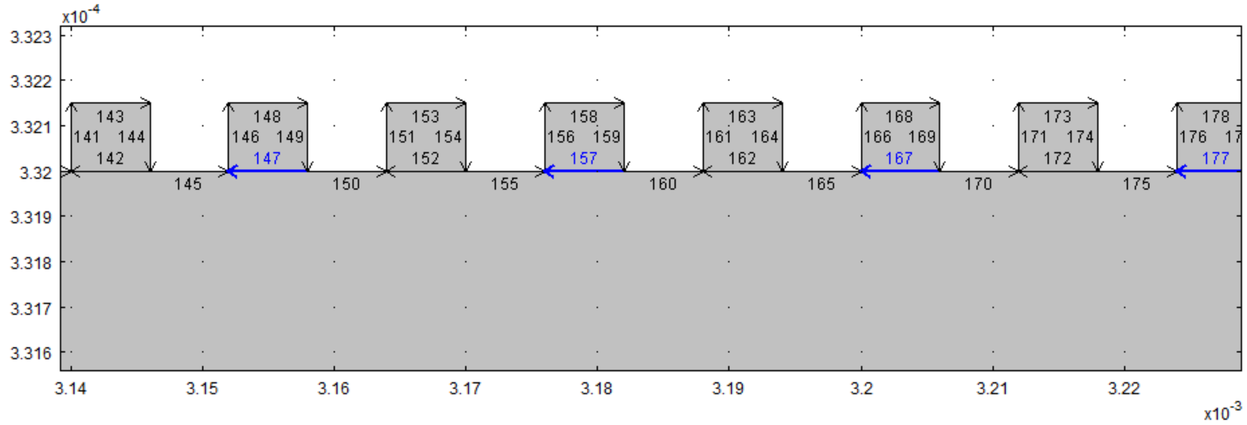

Fig. 3.5 The assignment for the boundary condition electrical potential 1

The next step is to mesh the whole geometry. Here the sequence type is selected as physical-controlled mesh and the element size is chosen as normal. We can also choose user-controlled mesh to generate mesh manually if the automatic mesh is not satisfied. There are totally 139544 elements generated which are shown in Fig. 3.6.

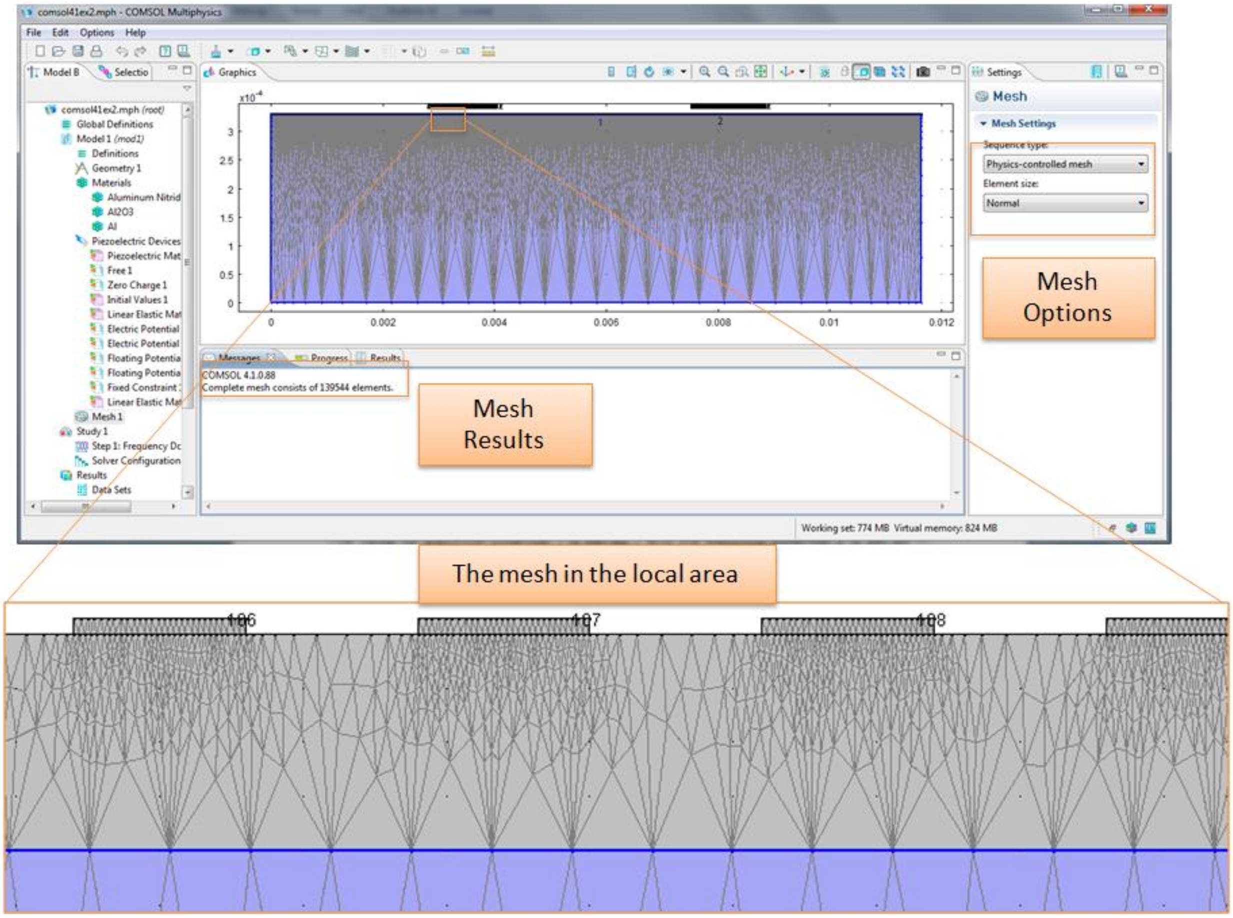

Sequence type: Physics-controlled mesh
Element size: Normal

Mesh Options

COMSOL 4.1.0.88
Complete mesh consists of 139544 elements.

Mesh Results

Working set: 774 MB Virtual memory: 824 MB

The mesh in the local area

Fig. 3.6 The mesh plot for 2D device without the insulator

After meshing the whole domain, some studies, e.g. frequency response analysis or time domain response analysis can be carried out. In this work the frequency response is investigated by adding the frequency-domain model under the study tab. The interested frequency is set from 230MHz to 260MHz. The step is chosen as 1MHz. A parallel sparse direct solver MUMPS is in use for its fast computational speed [135]. The number of degrees of freedom in this study is 746665.

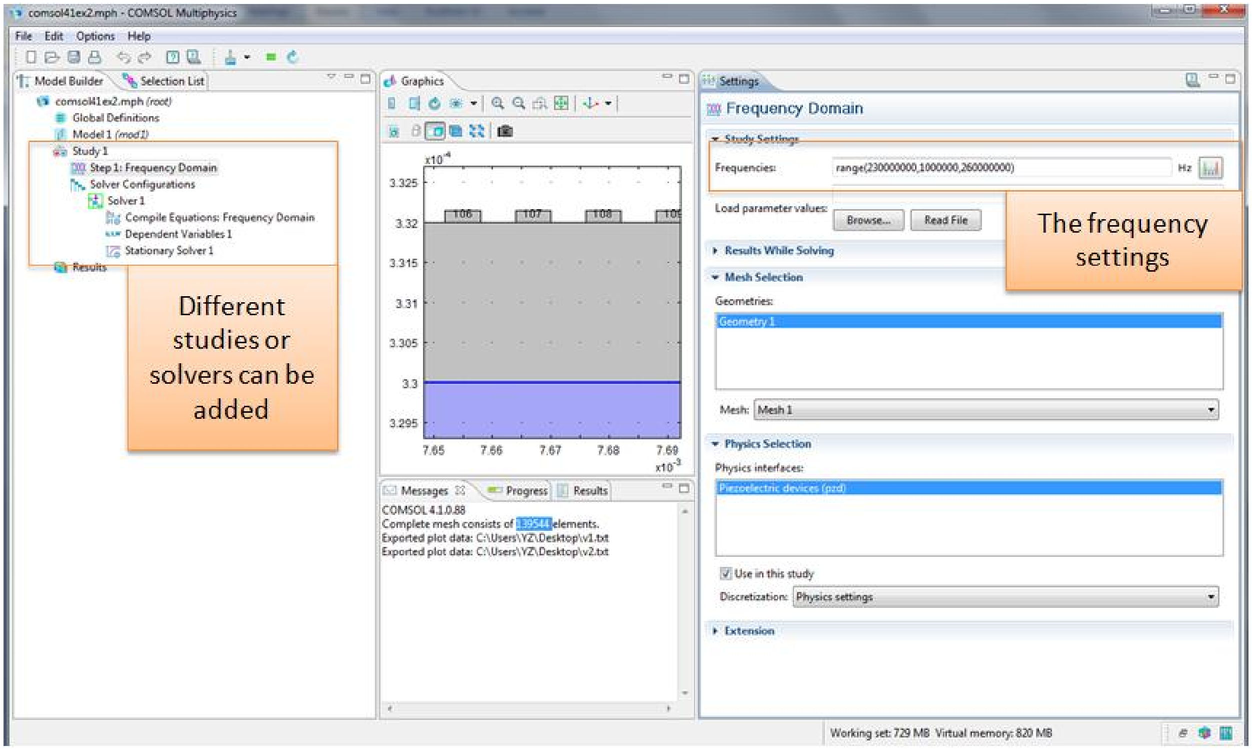

Different studies or solvers can be added

The frequency settings

COMSOL 4.1.0.88
Complete mesh consists of 139544 elements.
Exported plot data: C:\Users\YZ\Desktop\v1.txt
Exported plot data: C:\Users\YZ\Desktop\v2.txt

Frequency Domain

Study Settings

Frequencies: range(230000000,1000000,260000000) Hz

Load parameter values:

Results While Solving

Mesh Selection

Geometries: Geometry 1

Mesh: Mesh 1

Physics Selection

Physics interfaces: Piezoelectric devices (pzd)

☑ Use in this study

Discretization: Physics settings

Extension

Fig. 3.7 The detailed settings for frequency response analysis

We can add 2D plots and 1D plots to display the final result. With a 2D plot, the surface plot of all variables including electrical potential, displacement, stress, strain etc. can be displayed. In Fig. 3.8, the Y displacement (Z direction in 3D) at 242 MHz is shown. The surface acoustic wave can be observed clearly. In Fig. 3.9, the x component of strain tensor is displayed. The periodical pattern indicates the existence of surface wave. As a comparison, the Y displacement at 231 MHz is shown in Fig. 3.10. The strength of displacement is weaker by around 10^{-4} regarding to the 242MHz case. The terminal voltage of the floating potential can be observed with 1D plot shown in Fig. 3.11. The peak located at 242MHz agrees with the previous experimental result 243.325MHz [2]. The simulation error is about 1.325 MHz. Comparing to other FEM simulation references (e.g. [100, 107] more than 2.44MHz error) our simulation is better in terms of the center frequency. The wave propagation attenuation is neglected in the simulation that makes the value of terminal voltage high (Fig. 3.11). Considering the design validation purpose, such simplification is tolerable.

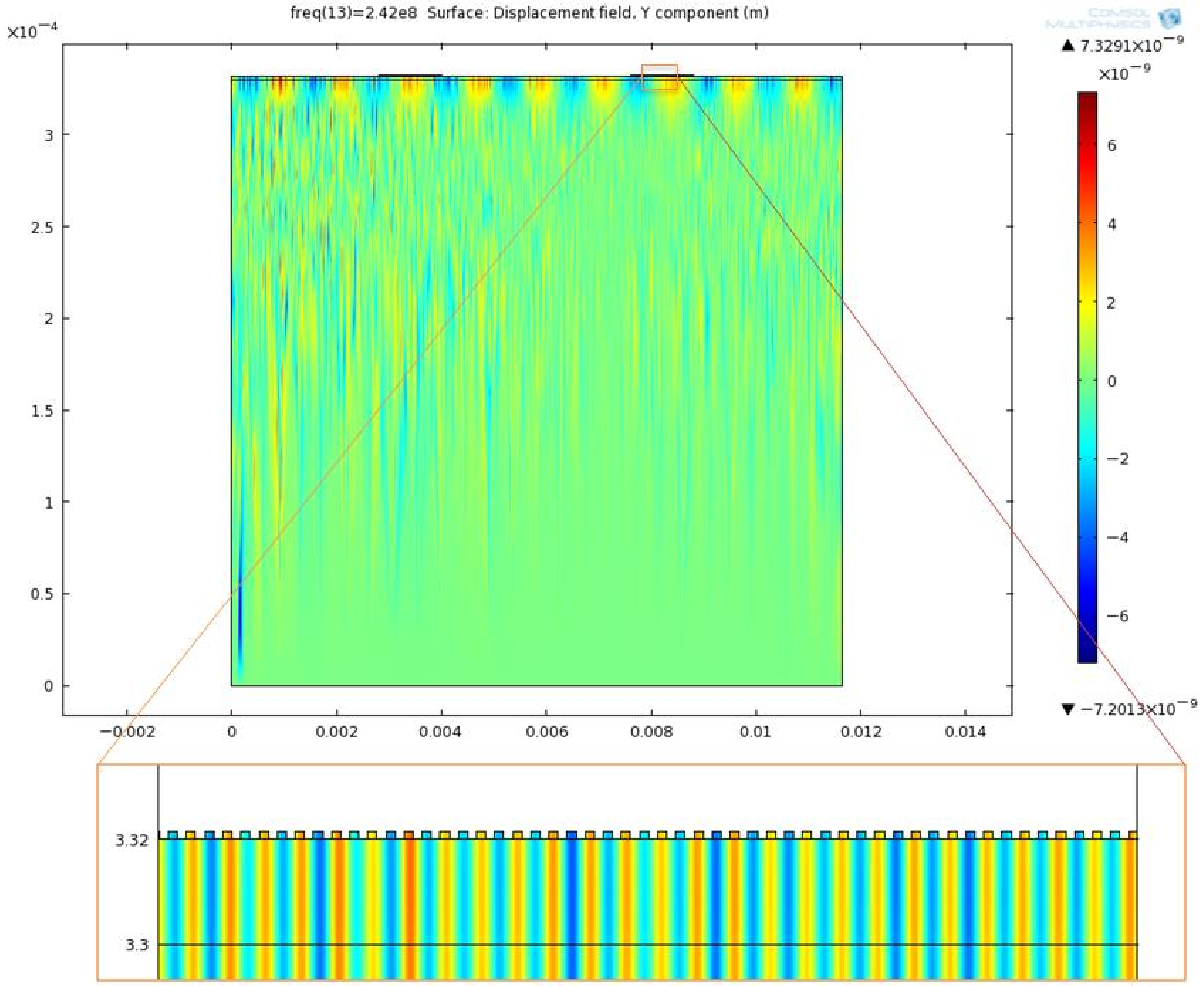

Fig. 3.8 The Y displacement (Z direction in 3D) at 242MHz. The surface acoustic wave can be observed clearly.

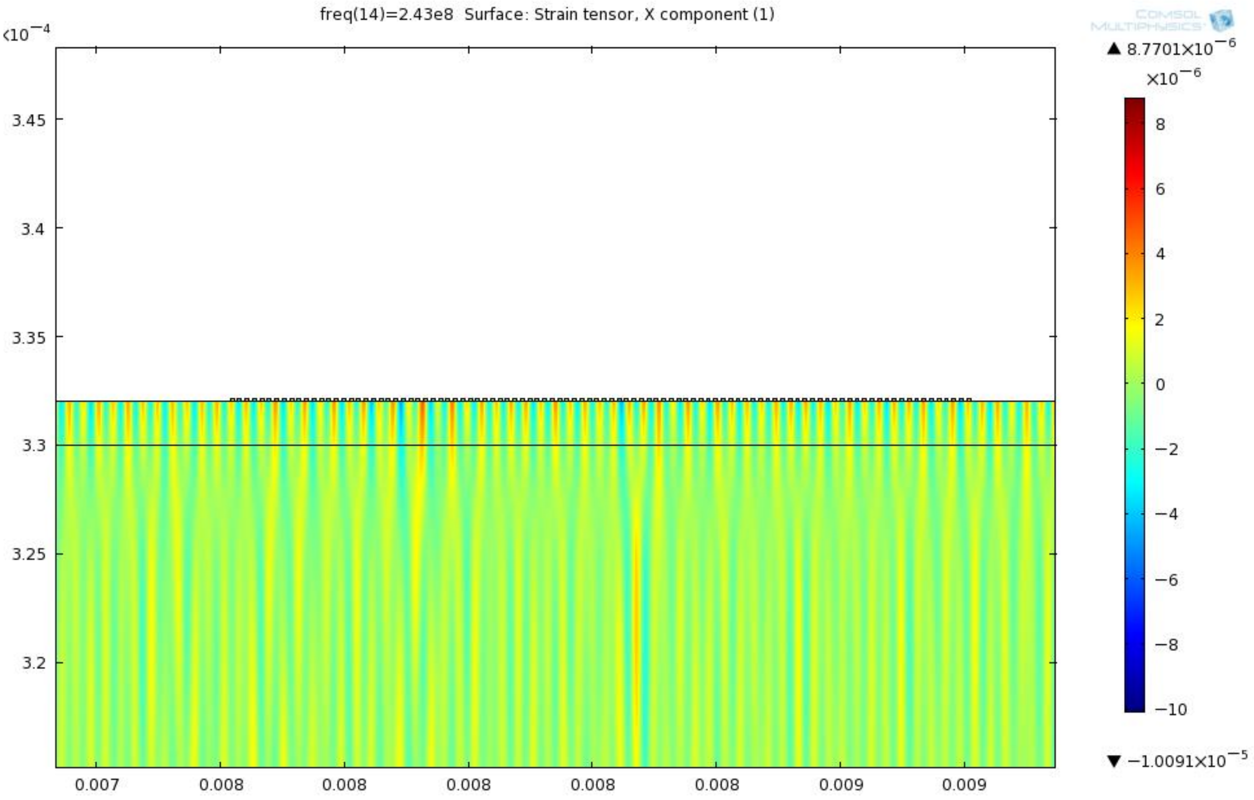

Fig. 3.9 The X component of strain tensors

Under the report tab, the 1D plot can be exported to Matlab® for further analysis. In this work a program to calculate insertion loss is written in Matlab® 2009. The result is shown in Fig. 3.12 (left). Comparing to the experimental results, the SAW mode at 242 MHz is apparently similar. The result proves the effectiveness of design for the device without the insulator.

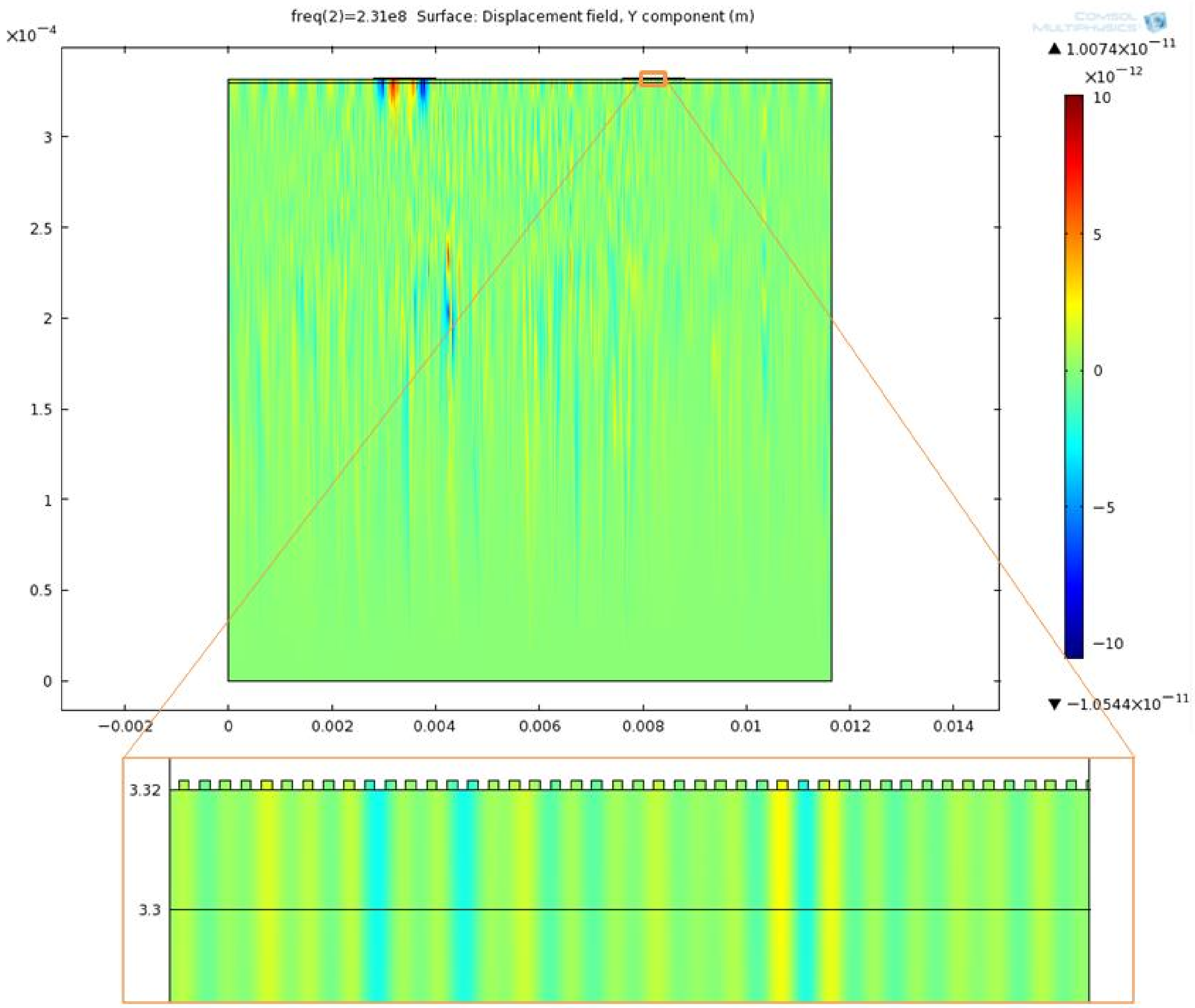

Fig. 3.10 The Y displacement (Z direction in 3D) at 231MHz. The surface acoustic wave is not obvious.

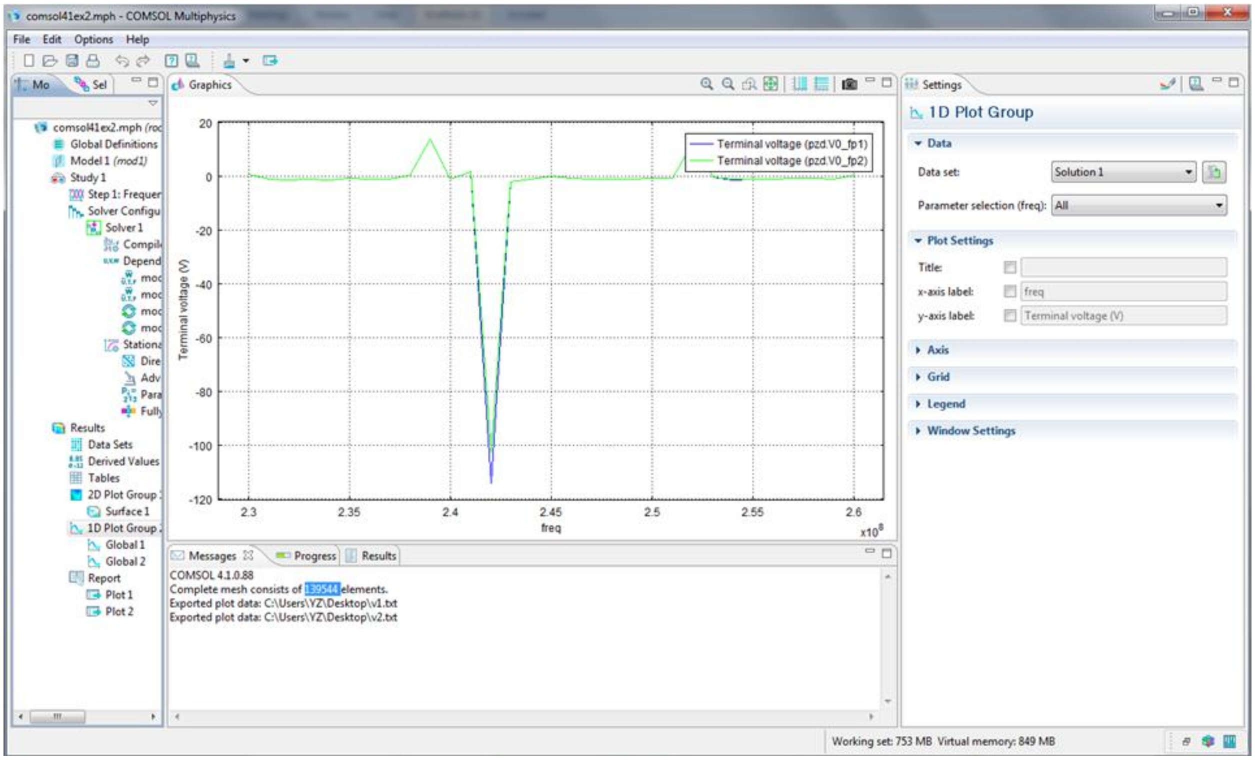

```
COMSOL 4.1.0.88
Complete mesh consists of 139544 elements.
Exported plot data: C:\Users\YZ\Desktop\v1.txt
Exported plot data: C:\Users\YZ\Desktop\v2.txt
```

Data set: Solution 1

Parameter selection (freq): All

Title: ☐

x-axis label: ☐ freq

y-axis label: ☐ Terminal voltage (V)

Working set: 753 MB Virtual memory: 849 MB

Fig. 3.11 The 1D plot of frequency response on the terminal voltage

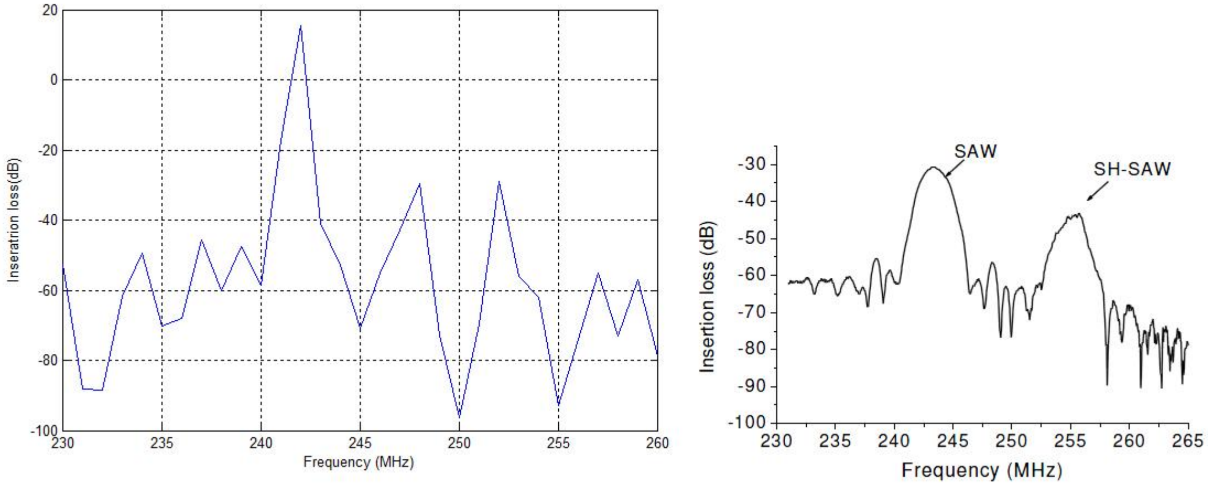

Fig. 3.12 The insertion loss for the device without the insulator (left). The right figure shows the experimental result [2]. The SAW mode from the simulation highly agreed with the experimental result in terms of center frequency.

3.3.2 FEM simulation for the device with the insulator

Based on the simulation model in the previous section, an AlN insulate layer is introduced into the simulation. In Geometry tab, two rectangles are added to cover the transceiver and receiver parts separately (shown in Fig. 3.13) whose parameters are specified according to Table 2.1. Since the insulator is also AlN, the boundary conditions for electrical potentials and floating potentials need to be changed to cover all boundaries (shown in 3.14).

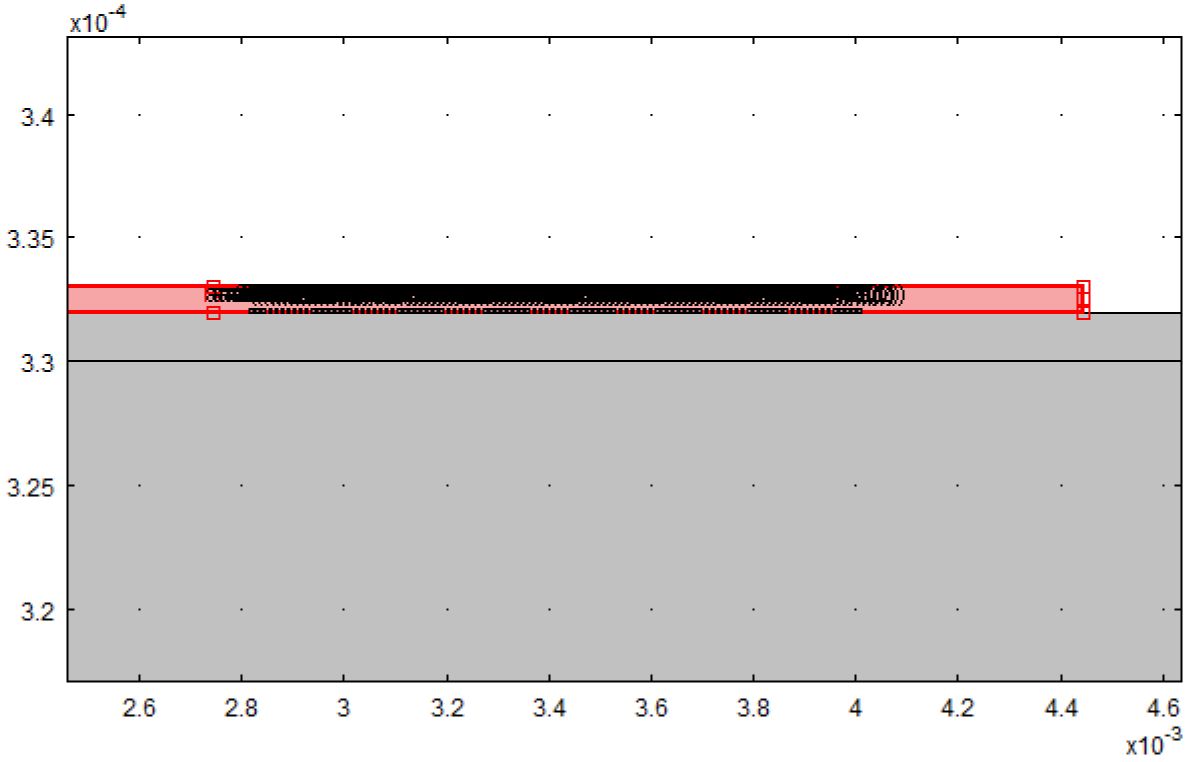

Fig. 3.13 The insulator layer is added to cover IDT

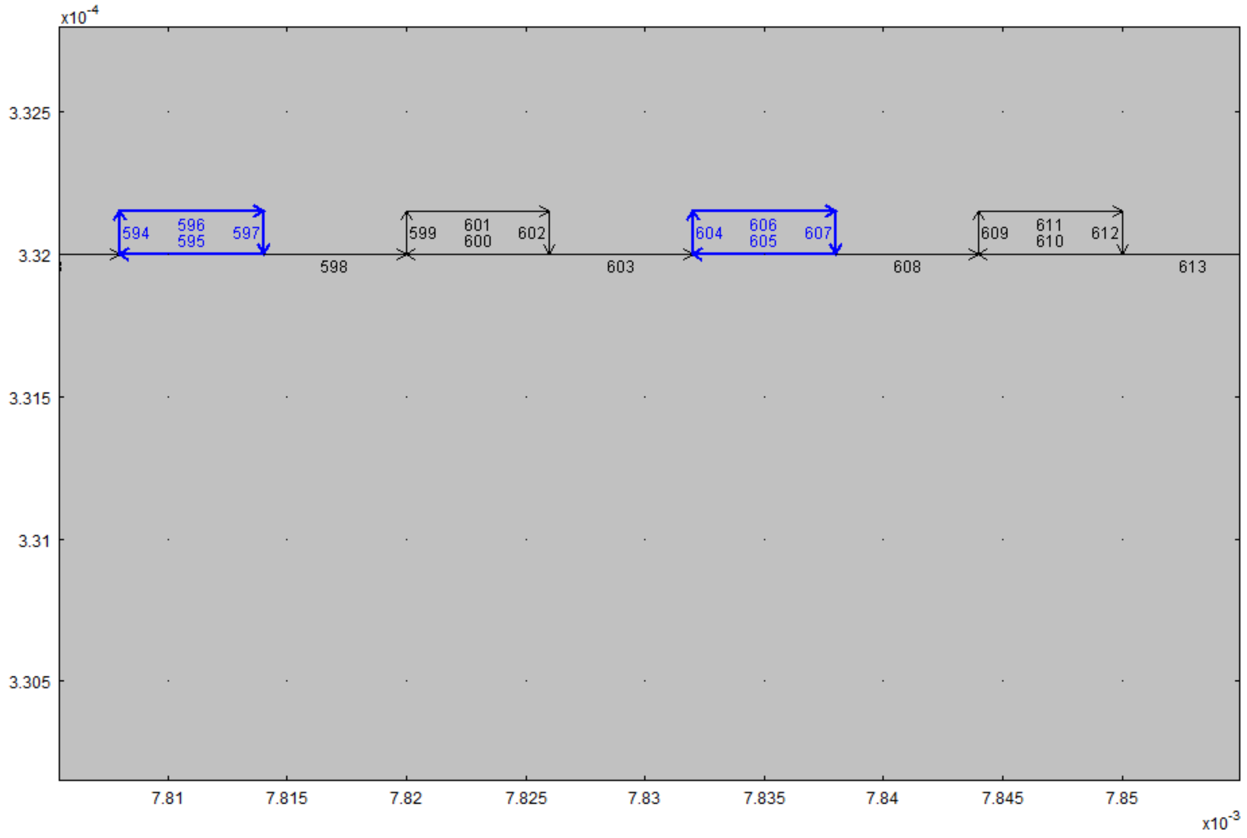

Fig. 3.14 The assignment for the boundary condition floating potential 1

In the step of mesh, the mesh size extra coarse is selected due to the more complex geometry. The resulting mesh element number is 174565. The mesh results are shown in Fig. 3.15. After 2 hours computation the frequency response is achieved. With 2D plot, the displacement can be observed for any frequency. Fig. 3.16 shows the obvious surface acoustic wave in Y direction. From Figs. 3.17 and 3.18 one can observe that the X component of the stress varies periodically on the top of the device and the Y component of the stress are changed in the internal of the device.

The terminal voltage and insertion loss are shown in Figs 3.19 and 3.20 respectively. From the simulation we can conclude that the AlN insulator will also bring in attenuation. The centre frequency will also be shifted due to the mass change of the surface.

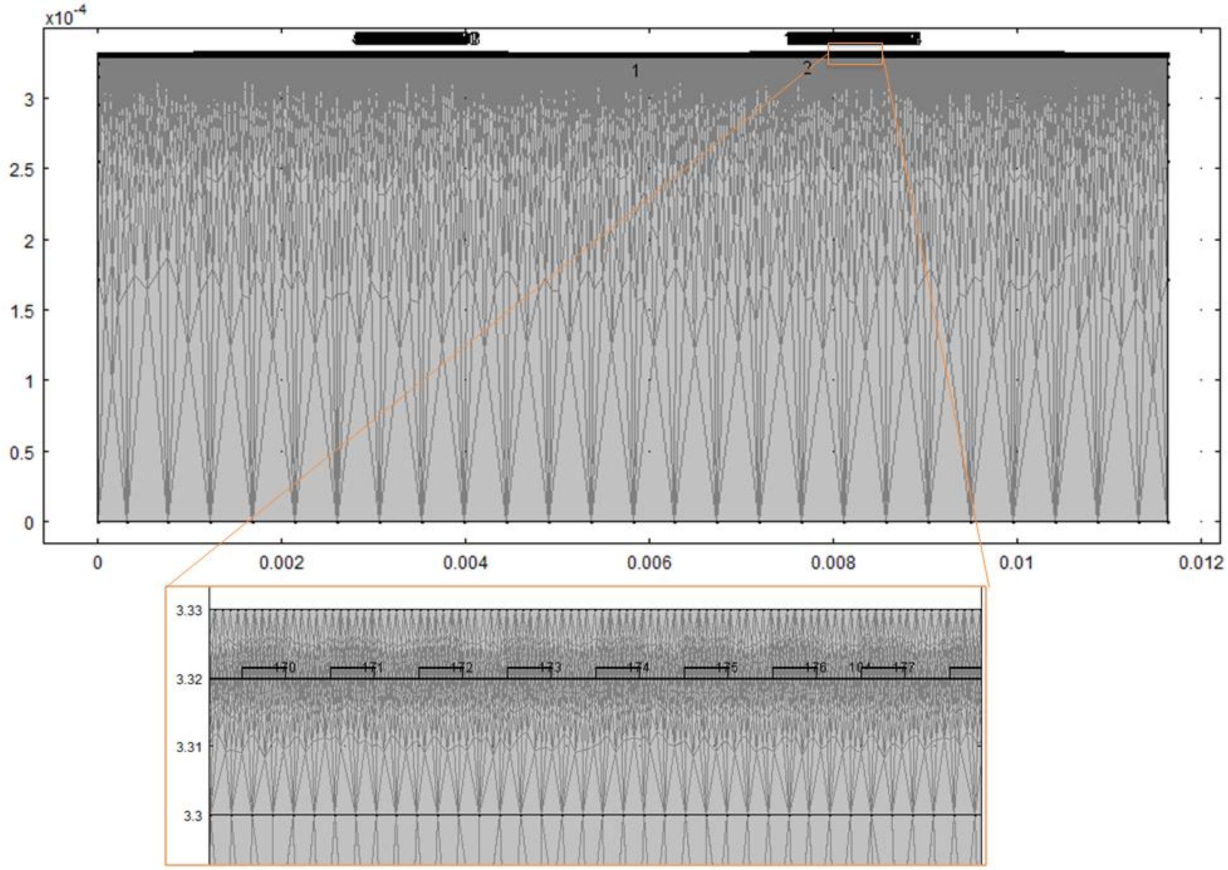

Fig. 3.15 The mesh plot for the device with the insulator

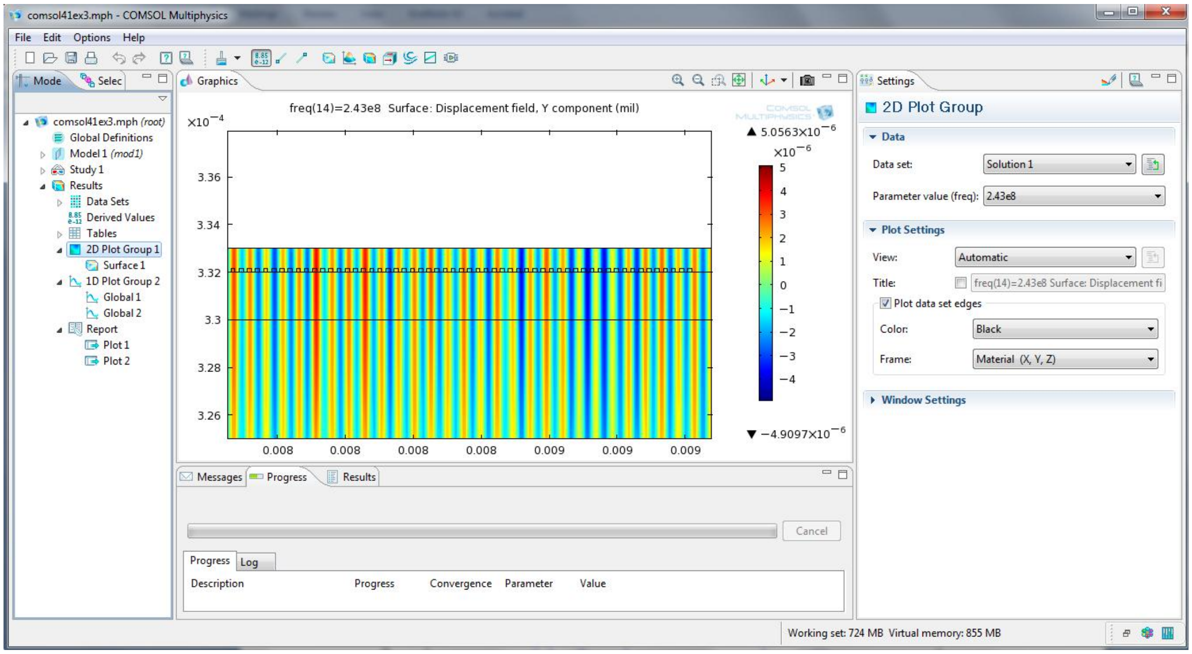

Data set: Solution 1

Parameter value (freq): 2.43e8

View: Automatic

Title: ☐ freq(14)=2.43e8 Surface: Displacement fi

☑ Plot data set edges

Color: Black

Frame: Material (X, Y, Z)

Fig. 3.16 The Y direction (Z direction in 3D) displacement for the device

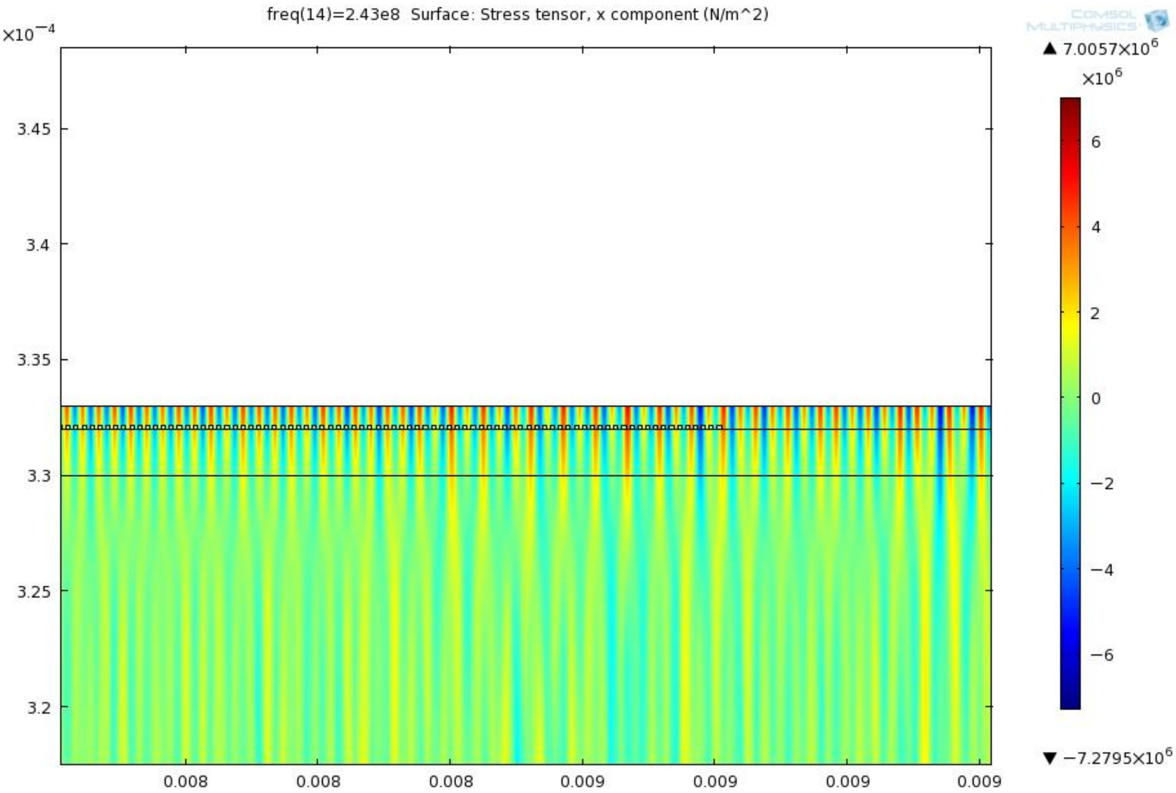

Fig. 3.17 The X component of stress tensor for the device

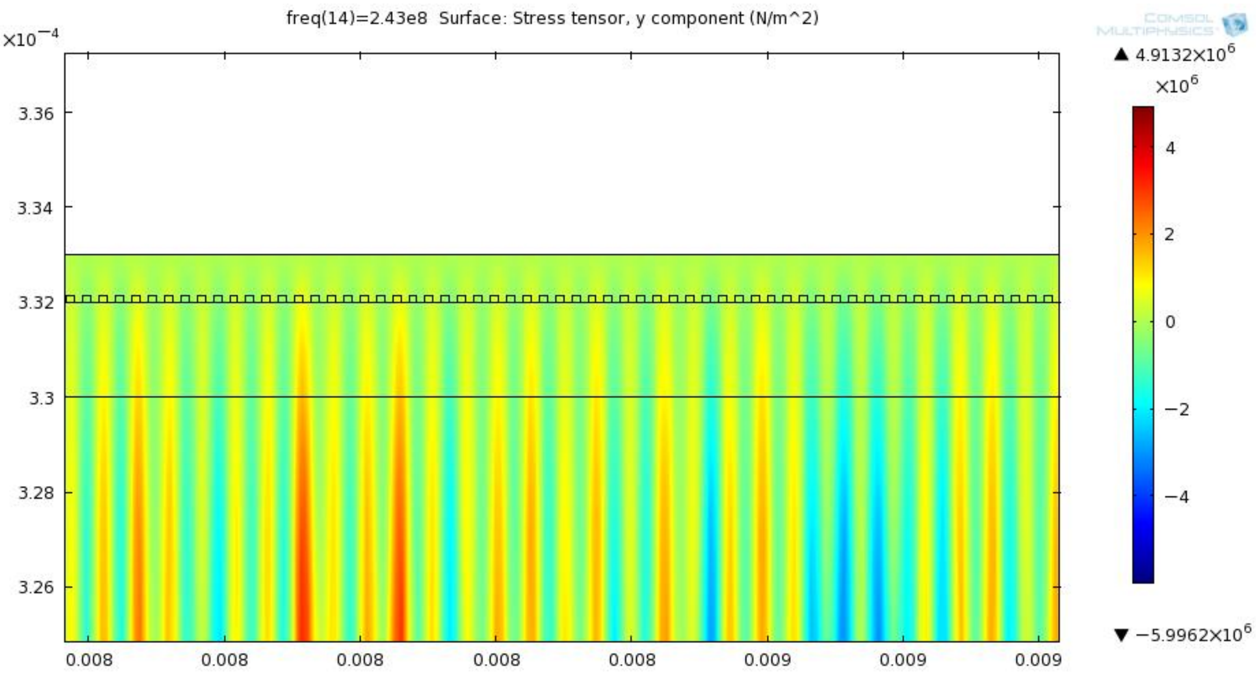

Fig. 3.18 The Y component of stress tensor for the device

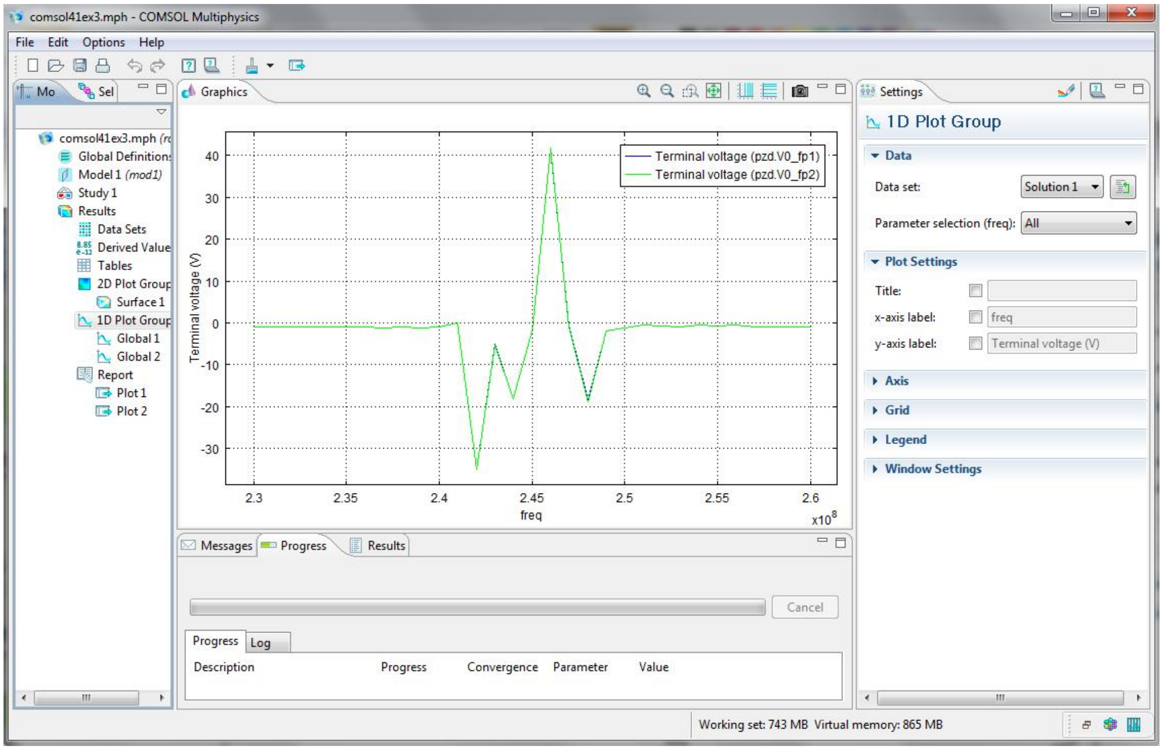

Data set: Solution 1

Parameter selection (freq): All

Title: ☐

x-axis label: ☐ freq

y-axis label: ☐ Terminal voltage (V)

Working set: 743 MB Virtual memory: 865 MB

Fig. 3.19 The 1D plot of frequency response on the terminal voltage

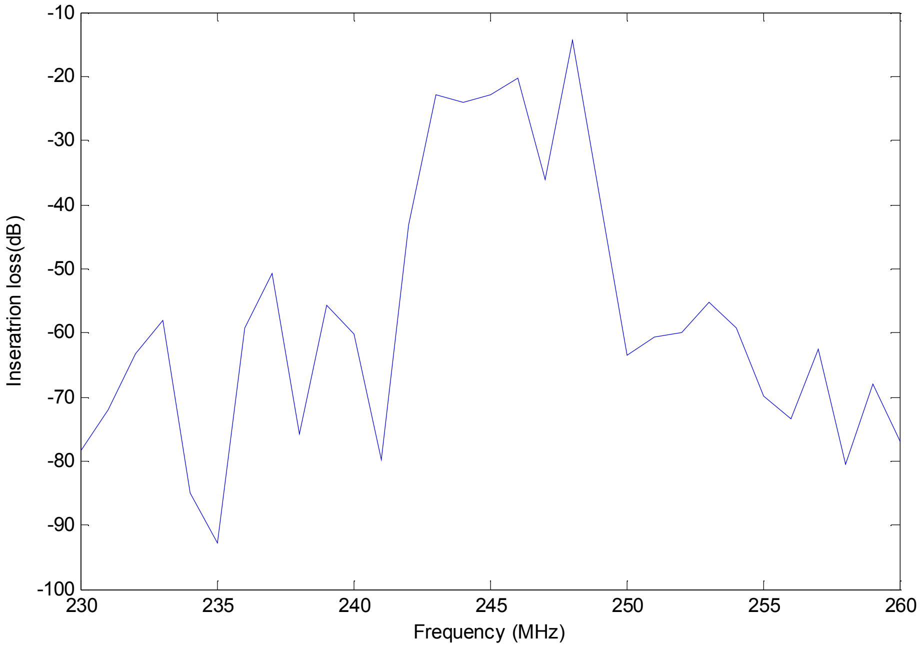

Fig. 3.20 The insertion loss for the device with the insulator

3.4 3D Simulation for AlN-based SAW Device with COMSOL 4.1

The whole device modeling based on the design parameters is tried initially however abandoned due to the memory limitation. In this section a simplified 3D model simulation is performed. Note that most SAW device simulations are based on simplified model in the existing literatures [100, 107-108, 136] or reduced mesh size ([137] from the workstation equipped with 48GB memory) .

The geometry for each device component is created first in COMSOL (shown in Fig. 3.21). The detailed dimension for each component is listed in the Table 3.1.

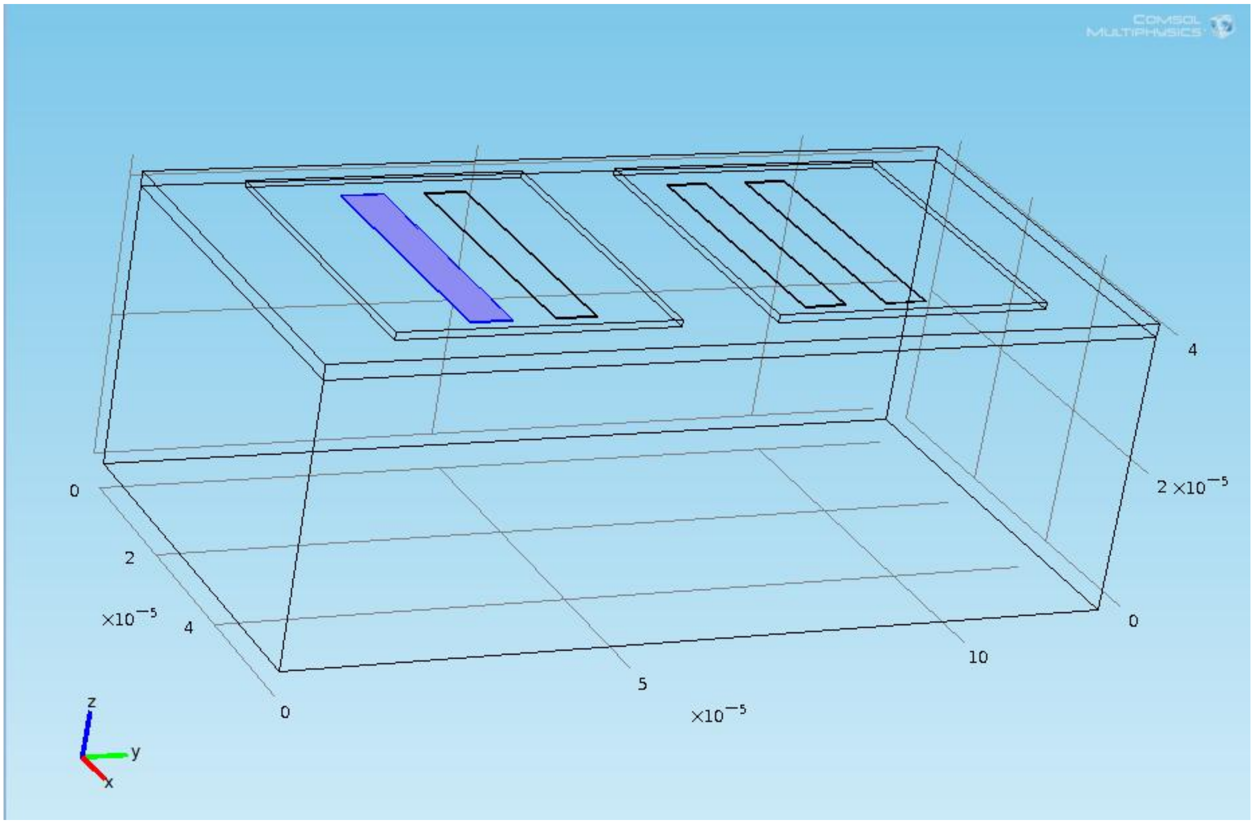

Fig 3.21 The 3D model geometries.

Table 2.1 All geometric parameters for simplified 3D model

IDT finger width	6 µm
IDT finger length	40 µm
Distance between two adjacent IDT fingers	6 µm
Distance between transmitter and receiver IDT	24 µm
Number of IDT pairs	1+1
Insulator width	48 µm
Insulator length	40 µm
Insulator center distance	6 µm
Insulator thickness	1 µm

Substrate thickness	40 μm
Piezoelectric layer thickness	2 μm
Substrate width	60 μm
Substrate length	120 μm

Similar to the 2D case, the boundary condition needs to be specified for each boundary. In 3D case the boundary becomes a surface instead of a line. Fig. 3.22 shows the boundary selection for floating potential 2.

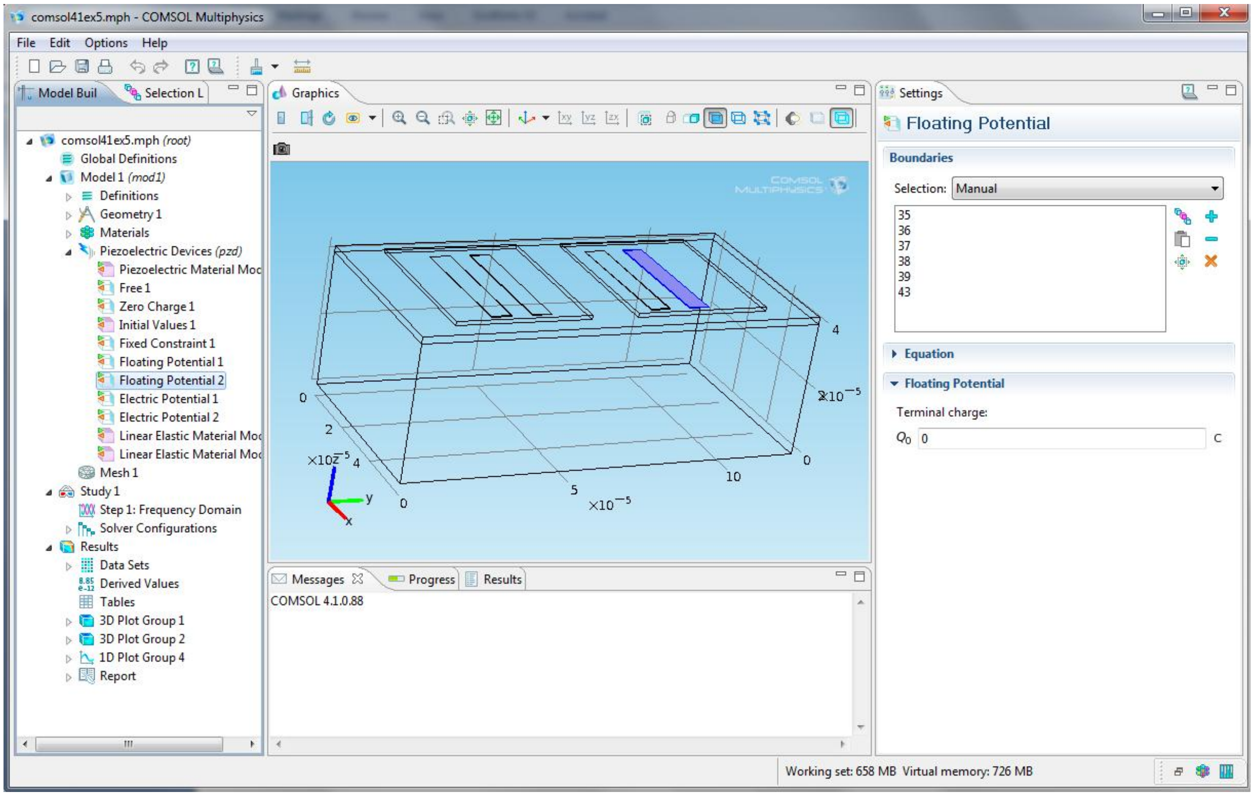

Floating Potential

Boundaries

Selection: Manual

35
36
37
38
39
43

Equation

Floating Potential

Terminal charge:

Q_0 0 C

COMSOL 4.1.0.88

Working set: 658 MB Virtual memory: 726 MB

Fig. 3.22 The boundary condition assignment for floating potential 2

The physics-controlled mess creation is also employed. The coarser option is selected to control the element size. Total element number is 65602 and the mesh status is shown in Fig. 3.23.

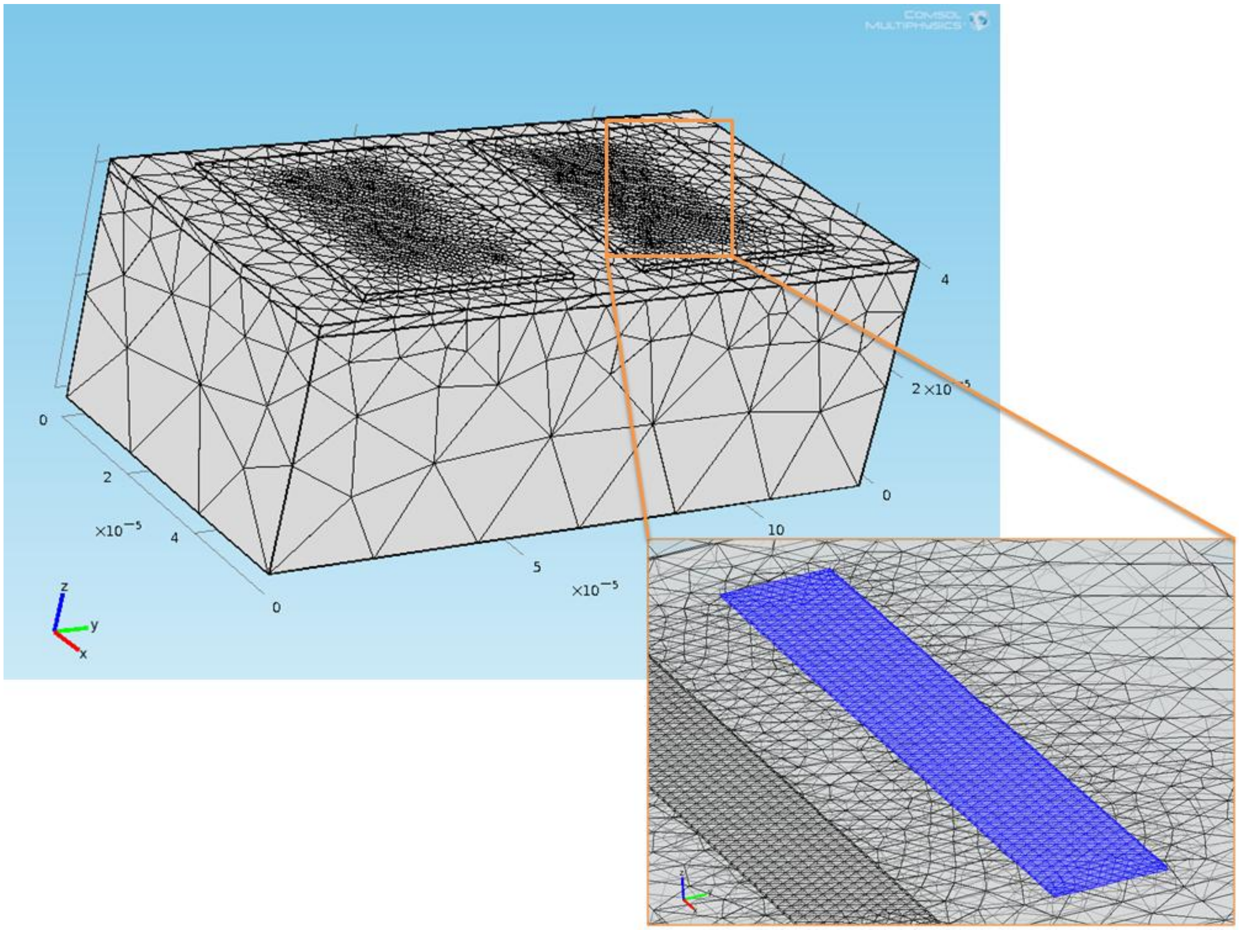

Fig. 3.23 The mesh plot for the simplified 3D model

MUMPS solver is used to solve this FEM problem. After 8 hours simulation, the results are shown in Figs. 3.24 - 3.27. From the Fig. 3.24, the SAW mode can be observed while the SH-SAW mode can be found from Fig. 3.25 which is unable to be observed in the 2D simulation. Fig 3.27 shows the insertion loss of the frequency response. The result reveals the existence of SAW mode and SH-SAW mode however it is not perfect matched our experimental result possibly due to the model simplification.

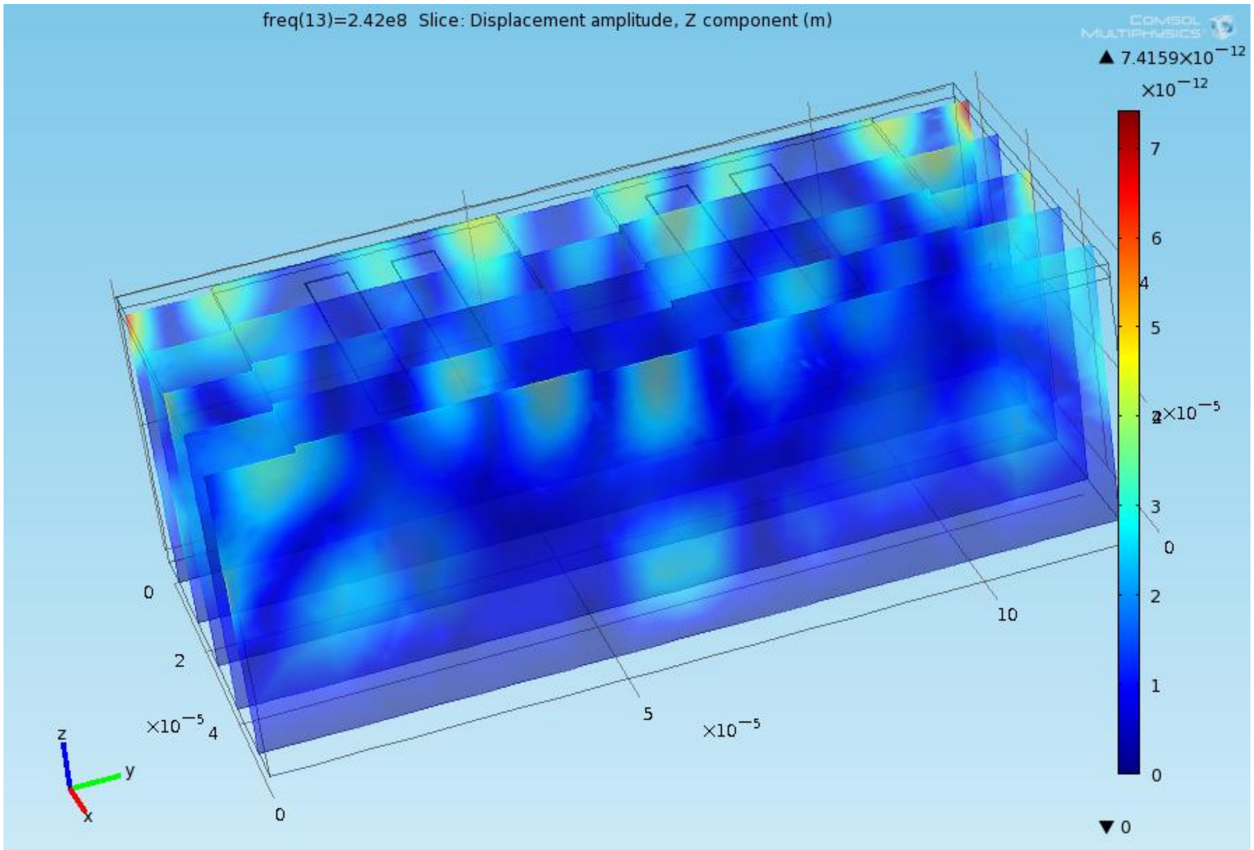

Fig. 3.24 The displacement amplitude for Z component

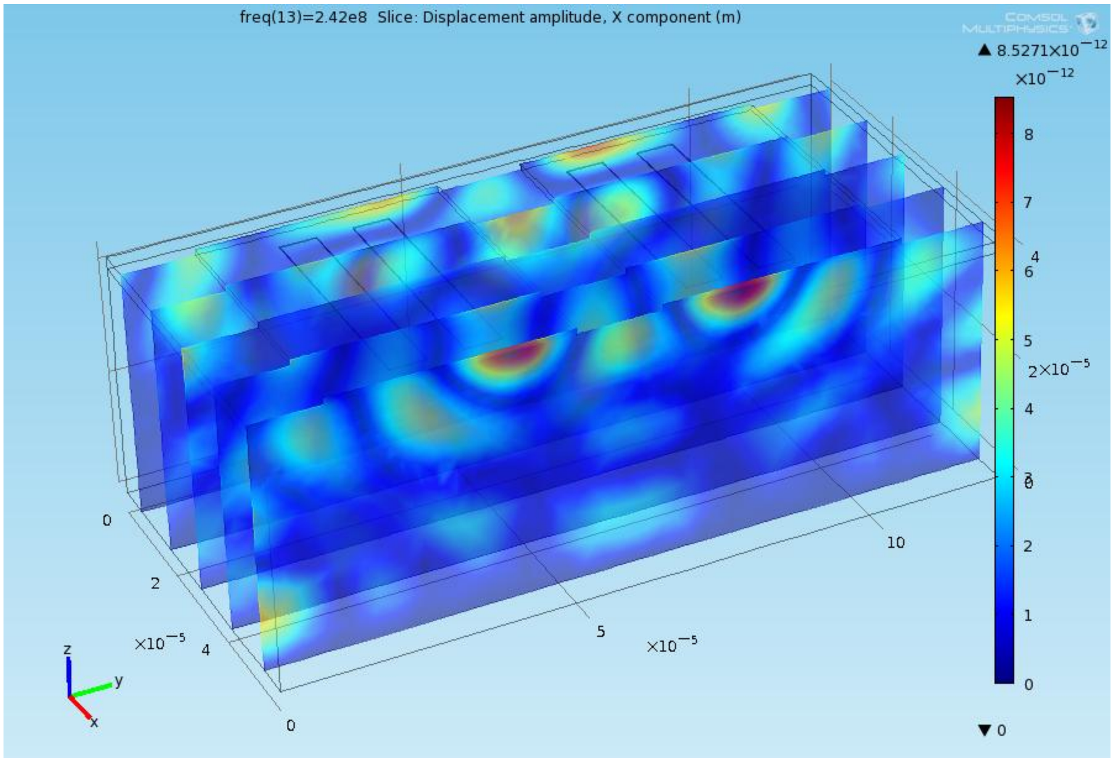

Fig. 3.25 The displacement amplitude for X component

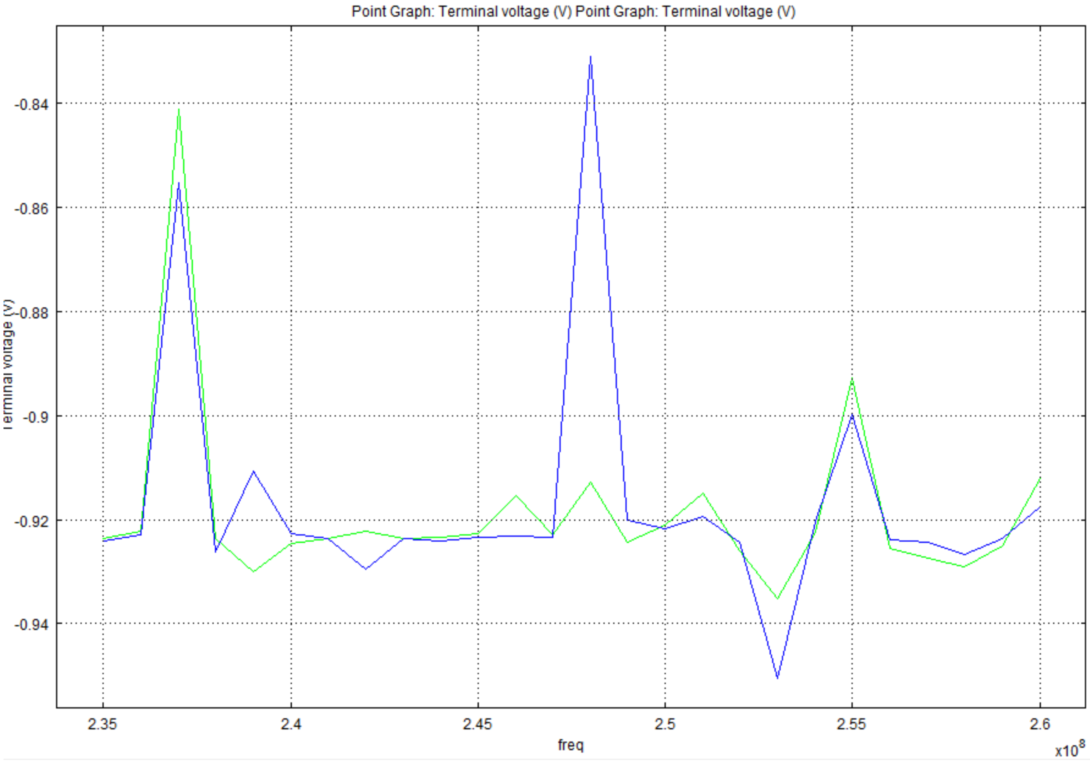

Fig. 3.26 The output terminal voltage for the simplified 3D model

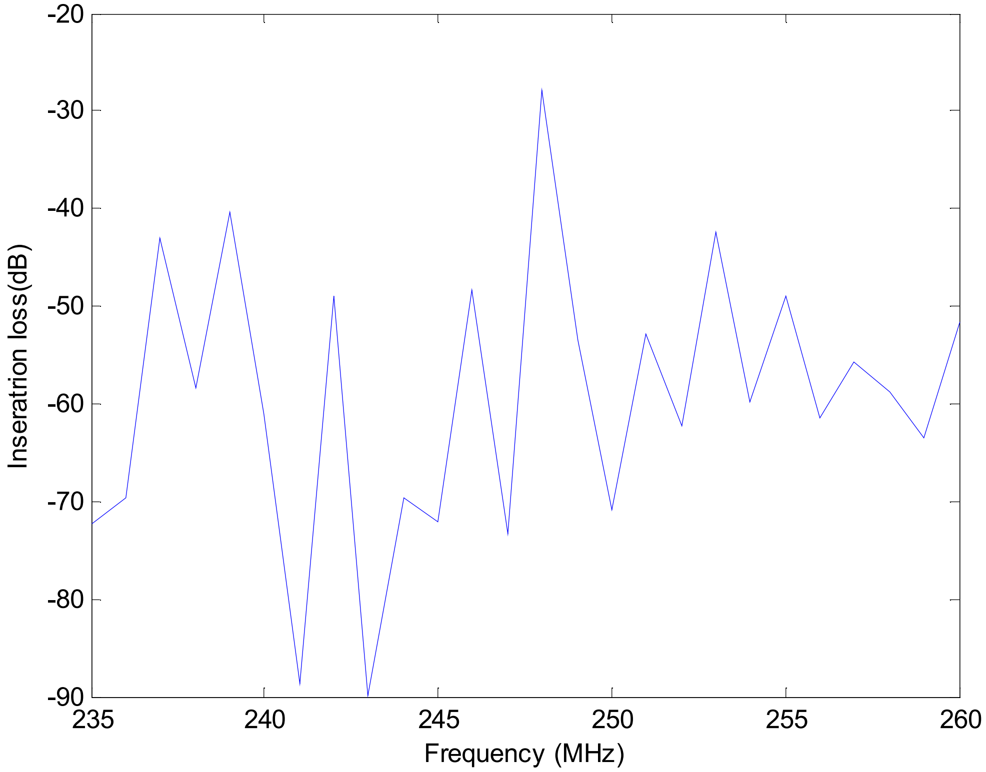

Fig. 3.27 The insertion loss for the simplified 3D model

CHAPTER 4 THE FABRICATION PROCESS FOR AlN-BASED SAW DEVICES

After theoretical and FEM validations, the design scheme was implemented in our SSIM clean room. Based on previous work in SSIM group for SAW device fabrications [2, 49], the detailed procedures for our AlN-based SAW devices are illustrated below.

4.1 The Piezoelectric Material AlN Synthesis

4.1.1 A Review on AlN Synthesis Approaches

AlN was first synthesized in 1862 from liquid Al and N_2 gas [47, 138]. Since then several growth methods have been used to get AlN but only some AlN powders containing very small crystals can be obtained [139]. These early results imply that the heteroepitaxy growth may be a promising way to synthesize AlN in large crystalline form. Here heteroepitaxy is one of epitaxy methods where the material for film and the material for substrate are different from each other. Epitaxy refers to the method of depositing a single crystalline film on a single crystalline substrate.

The first systematic effort to grow crystalline AlN by chemical vapor deposition or sputtering processes took place in the 1970s in order to characterize the optical and structural properties of thin films [47]. Thenceforward, a couple of groups have proposed various methods to grow high quality AlN thin film. Generally, these growing methods can be divided into three categories [42], physical transporting techniques (mechanical or thermodynamic methods), chemical transporting techniques (chemical change by fluid, gas or ionized vapor), and hybrid transporting techniques. These techniques are briefly overviewed as follows.

The first category includes liquid phase epitaxy (LPE) [140], physical vapor deposition(PVD) [141-142], pulsed laser deposition (PLD) [143-146], etc. PLD employs high energy laser to irradiate the stoichiometric AlN target so that the evaporated material is induced and condensed onto the heated substrate near the target surface with low growth temperature because the average energy of particles in the laser is 100 to 200 times of thermal evaporation process. The disadvantages of PLD technique are the expensive solid nitrides targets and limited thickness of deposition layer (about 250 nm in [144]). For PVD technique, AlN thin films were deposited by DC reactive magnetron sputtering at room temperature using a Minimak cathode and an aluminum target connected to a variable power supply with 30% nitrogen partial pressure in the nitrogen-argon gas mixer. The deposition rate can be 40nm/min. This method avoids the solid nitrides target using in PLD but still associate with limited thickness of AlN layer (about 500nm on Si substrate in [142]). LPE employs Sn-Ca flux which has a low melting point as well as the ability to resolve N_2 gas by relatively small pressure to react with Al in a boron nitride crucible. The temperature is about 900°C and gas pressure maintains 5 atm. The AlN grain with 10 μm thicknesses or thin film with 1.8 μm thicknesses can be synthesized in 96 hours.

The second category consists of chemical vapor deposition (CVD) [147], vapor phase epitaxy (VPE) [47], metal-organic chemical vapor deposition (MOCVD) [148-149], metal-organic vapor phase epitaxy(MOVPE) [150-151]. Chemical methods have been widely used because of its high growth rates which is up to a few tens of micrometers per hour [47]. The deposition of AlN by MOCVD has traditionally carried out from trimethyaluminum (TMA) and ammonia (NH_3). Reactor pressure and temperature were 20 Torr and 1150.8 C, respectively. A typical growth rate is about 1μm per hour.

The third category includes molecular beam epitaxy (MBE) [50, 152], plasma assisted molecular beam epitaxy (PAMBE) [153], ion source molecular beam epitaxy (ISMBE), gas source molecular beam epitaxy (GSMBE) [154], plasma source molecular beam epitaxy (PSMBE), radio-frequency plasma-assisted molecular beam epitaxy (RFMBE) [155], metal-organic molecular beam epitaxy (MOMBE) [156], RF diode sputtering [157] etc. In this category, the plasma source or ion source is used to lower the substrate temperature during deposition. In the growth of basal-oriented AlN on Si (111) substrates is only at the temperature of 100°C [158]. PSMBE method will be employed in this work for AlN SAW device fabrication.

4.1.2 AlN Thin Film Deposition

The AlN thin film is grown with the help of plasma source molecular beam epitaxy (PSMBE) system [159] in our group. PSMBE is a magnetron sputtering system whose root can traced back to 1970s [160]. Our group has employed the PSMBE system (shown in Fig. 4.1) on AlN film growth on Si and sapphire substrates from 1995 [161]. The system was initially designed by Dr. Gregory Auner and fabricated by Perkin-Elmer's physical electronic division [162]. The main part of the system is a 24-inch-diameter stainless steel chamber attaching various ports with different sizes for mounting additional equipments [163]. The sample is loaded through load-lock chamber and fixed on the main chamber holder. The sample can be heated and rotated controlled remotely. The growth temperature is measured by a K-thermocouple on the back of the substrate and an infrared 2λ pyrometer OMEGA IRRC-300-43-C24. There are two ultra-high vacuum pumps, CTI-Cryogenics cryopump and Perkin Elmer ion pump, to maintain the main chamber base pressure at 10^{-10} Torr. The ion pump uses high powered magnet to capture any gaseous species present, while the cryogenic pump uses an extremely cold liquid helium baffle (4K) to condense and trap gases. A roughing pump and a turbo pump are employed to reduce pressure in the load-lock chamber. A high vacuum environment is very important to grow pure AlN crystalline film.

Four cylindrical magnetically-enhanced hollow cathode sources are installed in the bottom of the chamber and aimed towards the substrate (shown in Fig.4.2). The inner walls of the hollow cathode are lined with MBE grade Aluminum (99.999% purity). The target aluminum has 3° inward taper to allow the sputtering ions with a relatively low energy. The ions out of the sources with low energy avoid the bombardments on the wall of the main chamber which contains some impurities that may affect the quality of the AlN thin film. The cathode for each source is connected to an RF power supply operating at 13.56 MHz, controller and an impedance matching network independently. In our group, the advanced energy RFX 3000, RFX 1250 or RF plasma products RF-5S power supplies is in use. The metal anode shield is grounded to the chamber body and electrically insulated from the cathode. To be similar in principle to the fluorescent light, a capacitive coupled plasma (CCP) is generated between the anode and cathode. When the nitrogen and argon gas are injected from impeller, the electrical field between electrodes makes gas atoms ionized and release electrons. An ion is an atom (or molecule) with a net positive or negative electrical charge. The charge of an ion is equal to the difference between the number of protons and the number of electrons which is denoted as a superscript ‘+’ or ‘-’ following a number indicating the difference. If an ion contains unpaired electrons, it is called a radical ion which is generally very reactive. The electrons in the gas are accelerated by the RF field and hit the other atom to produce secondary electrons. When the RF power is high enough, the whole gas becomes electrically conductive (the plasma with radicals) due to this phenomenon called electron avalanche. Generally, the light emission is accompanied in this process. Therefore, we can see the pink light if the plasma is successfully ignited. Since the ions are much heavier than the electron, the cathode collects more electrons in the positive cycle of RF power than positive ions in the negative cycle [164]. A negative DC potential is self-developed, so called “self-bias” between the plasma and the electrode [165]. As a consequence, the ions’ energy can reach a few hundred eV and be accelerated to the cathode. When the ions in plasma bombard on the wall of cathode the Al atoms are induced sputtering from the cathode surface since the energy of the incoming ions is much greater than the binding energy of the target atoms. The heavy Ar+ ions help to create Al atoms. The sputtered atoms are not in their thermodynamic equilibrium state, and therefore tend to deposit on the surface (e.g. the sapphire wafer in our case). The average energy of the ions out of sources is much smaller (1eV) than that in the sources. A DC bias potential is added in the substrate holder to accelerate the ions to deposit to the substrate.

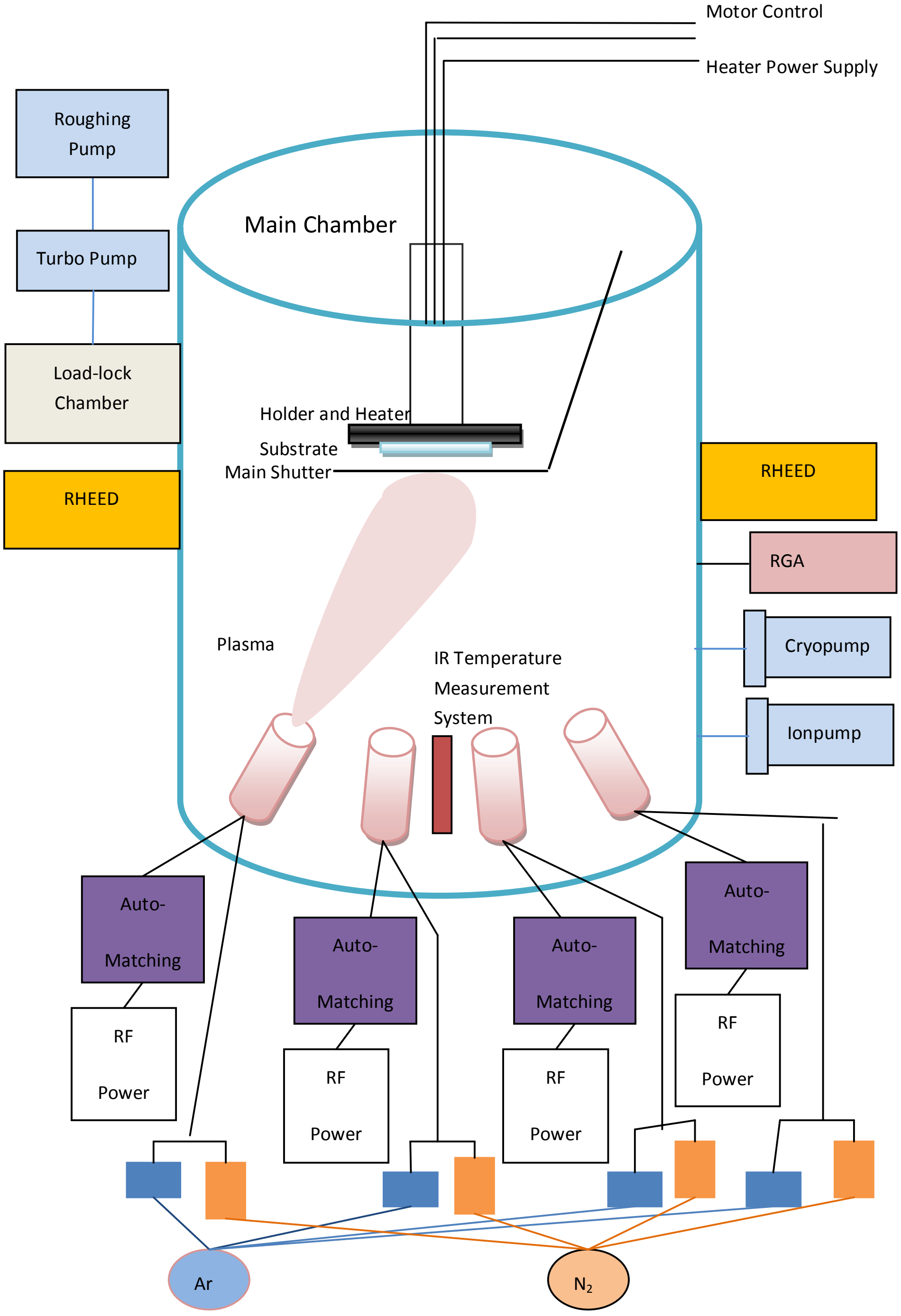

Fig. 4.1 Schematics of the PSMBE system

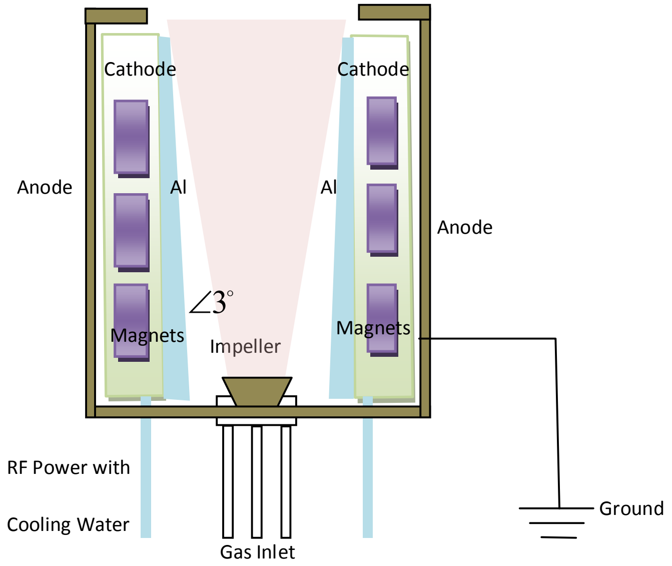

Fig. 4.2 The cylindrical magnetically-enhanced hollow cathode source

The permanent magnets are imbedded in the source wall to generate a magnetic field that confines plasma secondary electrons near the target surface of the cathode [162]. The magnetic field lines are elliptically shaped and parallel with the target surface. Therefore, the electrons moving in the source experience a sideways force (Lorentz force) which is perpendicular to the magnetic field and motion. For this reason, the electrons' movement trace will be a circle or helix around magnetic field lines which is called cyclotron motion. Such a motion increases the overall distance that an electron travels so that increases the probability of the collision between electrons and ions. Hence, the plasma density inside the source is increased effectively with the magnetic field [164, 166]. It also makes the target material erosion uniformly [42]. When all the shutters are open for deposition, we connect a negative DC bias voltage to the substrate holder. The plasma containing Ar+, Al+, and N+ (N_2^+) move towards the substrate to complete the deposition. The AlN growth can be amorphous, polycrystalline or single crystal depending on the deposition conditions.

There are several equipments to monitor the deposition process. The chamber residual gas composition can be measured by a Stanford research systems (SRS) RGA200 residual gas analyzer and displayed on the remote computer. The reflection high energy electron diffraction (RHEED) provides a direct measurement of the surface structure of the substrate wafer. The Staib instrument EK-2035-R RHEED electron gun is mounted on one side of the main chamber and a phosphor screen with a digital camera on the other side. The software KSA-400 is used to take the photos or movies remotely.

With these equipments, the AlN is able to be deposited to the sapphire substrate. The detailed steps are listed in Appendix 1.

4.2 IDT Fabrication Using Photolithography Techniques

After AlN film deposition on the sapphire substrate, the aluminum IDT will be coated on the surface of AlN. As shown in Chapter 2, our SAW device has 6 μm finger width and 150 nm film thickness. For split-finger design, the finger width is only 3 μm. To fabricate such a sophisticated device, different lithography techniques (photolithography, electron lithography [167], X-ray lithography [168-169] or ion bombardment etching [170]) can be employed. Electron beams can be readily focused to diameters on the order of 150 Å. Therefore electron lithography is suitable for small devices. X-ray lithography is similar to the photolithography but employs a much shorter wavelength radiation (10 Å). In our group, the photolithography technique is used for IDT deposition in our SSIM clean room [2, 49].

The photolithography is an optical lithography technique widely used in micro-fabrication field [171]. It shares some fundamental principles with photography e.g. exposing, etching, etc. The standard procedure is shown in Fig. 4.3. Firstly the substrate surface is coated with a radiation-sensitive polymer (known as photoresist) film. The photoresist is sensitive to short wavelength visible and ultraviolet light which results in the exposed area soluble in the developer (positive photoresist) or polymerized, i.e. difficult to dissolve (negative photoresist). The existing well-known produces include Shipley® (Rohm and Haas), Hoechst® (now called AZ electronic materials) and MicroChem® [172]. In this work, the photoresist S1811 made by Shipley®

and LOR 3A from MicroChem® are employed. The photoresist can be evenly coated onto the substrate through the photoresist spinner and baked in the oven or hotplate.

With the pre-designed photo mask, the surface of substrate is exposed to the light and the IDT pattern is recorded in the photoresist layer. A photo mask is an opaque plate with holes or transparencies that allows the light to pass through. Figs. 4.4 and 4.5 show the 6-inch photo mask used in this work (designed in [2], courtesy to Dr. Guopeng Hu). The software AutoCAD® is employed to design the photo mask and all rectangles drawn in Figs. 4.4 and 4.5 represent IDT pattern which will be fabricated as the transparent areas. Since the area for IDT should be covered by aluminum, the photoresist have to be positive type.

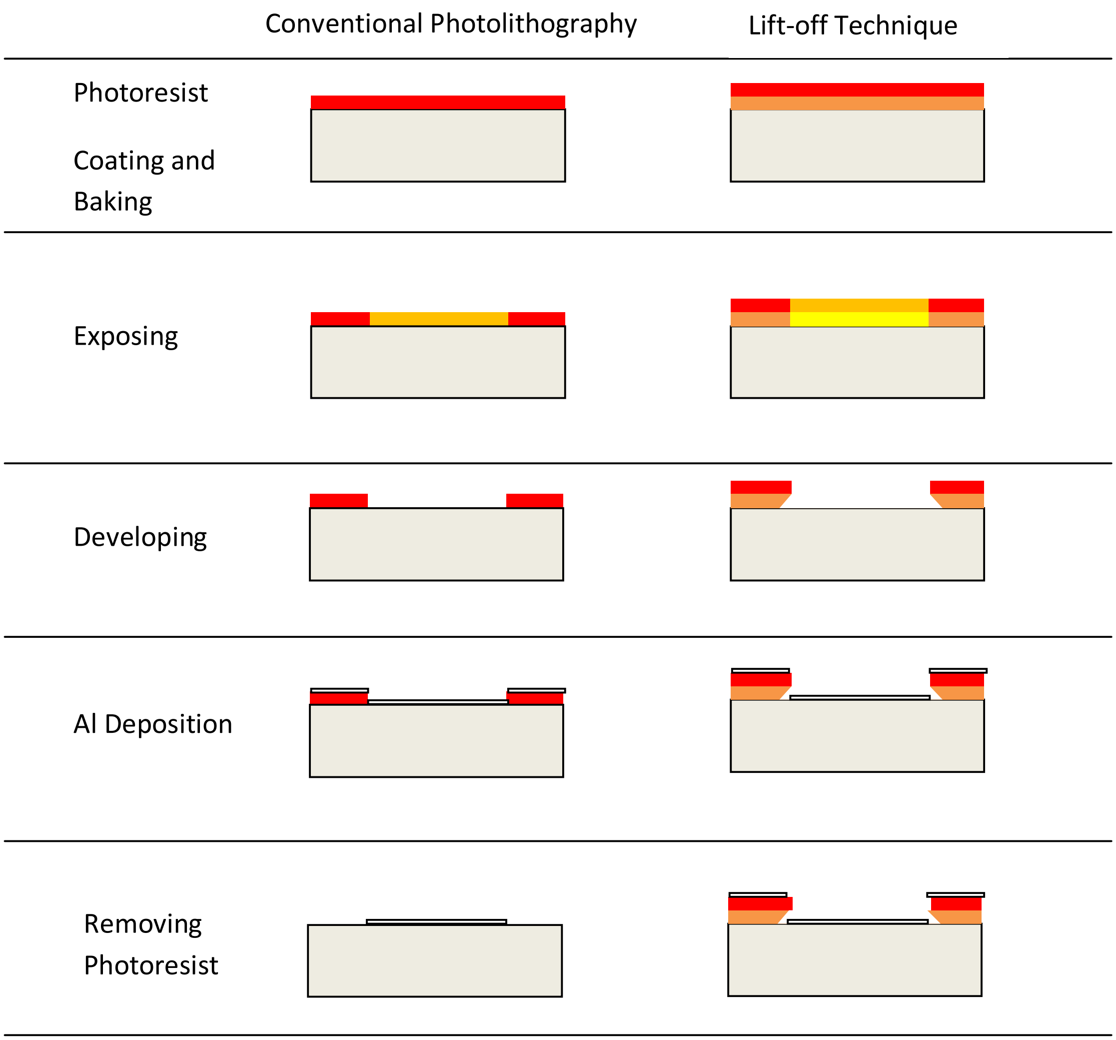

Fig. 4.3 Photolithography procedures and comparison between conventional photolithography and lift-off photolithography

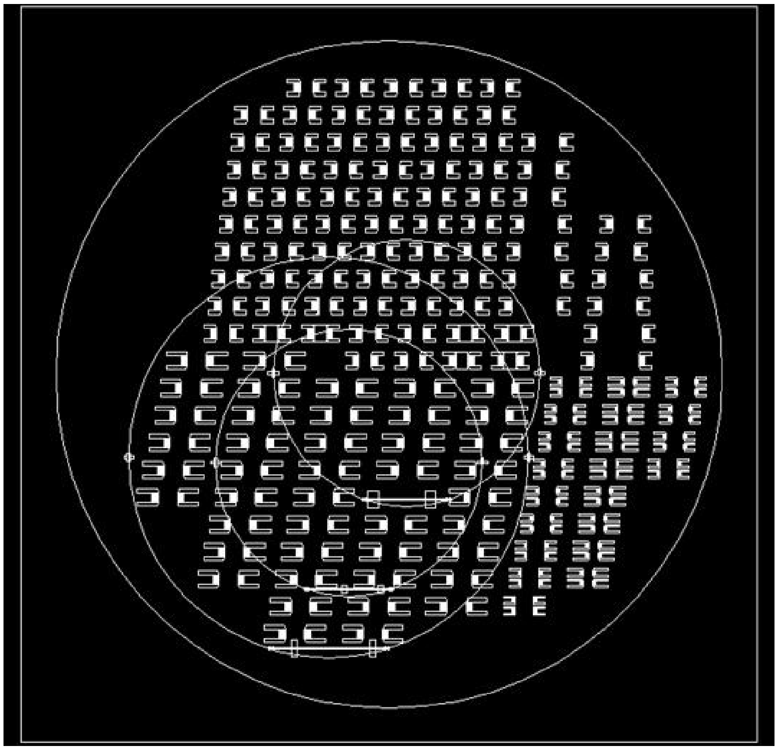

Fig. 4.4 The 6-inch photo mask with IDT patterns used in this work.

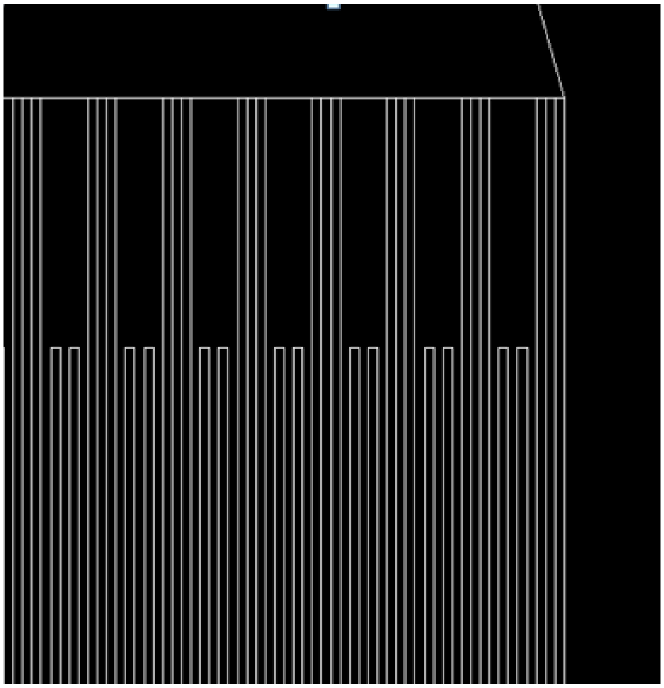

Fig. 4.5 The locally enlarged view

Generally, there are three exposing methods: projection printing, shadow printing and holographic recording. Projection printing uses an optical system to image the pattern onto substrate with some demagnification [173-174]. Shadow printing is the most widely used technique in photolithography also called contact printing. In this technique the glass photo mask is covered by thin-film chromium, Fe2O3, silicon, photographic emulsion or other ultraviolet attenuator and is contacted with or close to the substrate. The pattern will be duplicated on the substrate. It is a simple and inexpensive method but the exposed area is limited by the size of photo mask [175]. Some commercial instruments have been developed for shadow printing, e.g. MA6 mask aligner is employed in this work. The holographic recording utilizes the interfering of two laser beam [176-177]. A beam from argon, helium-cadmium, krypton or other short-wavelength laser is passed through a spatial filter and beam expander. Then it is split into two plane-wave beams with roughly equal intensity. The two beams are brought onto the photoresist-coated substrate together by a pair of plane mirrors. This method is able to provide more accurate and low distortion gratings.

After exposing, the whole sample needs to be treated in the developer bench to remove the exposed photoresist. In this work, the CD26 developer is in use. Then, on the top substrate, a layer of metal (aluminum is used in this work) will be deposited. Note that after developing, the IDT area will be directly covered by aluminum from metal deposition and for other areas, the aluminum is deposited on the photoresist. There are several ways to deposit aluminum, e.g. thermal evaporation, electron-beam-induced evaporation, plasma sputtering, etc [1]. The electron-beam-induced evaporation method is used in this work with the equipment BJD 1800 shown in Fig. 4.6. The last step is to remove the residual photoresist with the aluminum on top. The photoresist stripper Shipley® 1165 is employed in this work.

A problem for conventional photolithography technique is that it takes long time to remove photoresist after IDT deposition if the thickness of coated metal exceeds 50 nm [178] (the thick metal prevents the contact between the photoresist and photoresist stripper). Since the thickness of our IDT is about 150 nm, the lift off technique is used for photolithography in this work. The lift off technique makes the polymer and its coating of material be readily removable after deposition [2, 170, 175, 178-179]. The lift off process includes two photoresist coating. The LOR 3A from Microchem® is firstly coated and baked on the substrate surface. Photoresist 1811 from Shipley® is then coated on the top of LOR 3A. Since the LOR 3A is an inert, non-UV-sensitive polymer but solvent in most developers, after exposing and developing, an undercut can be found and shown in Fig. 4.3. In this way, the deposited aluminum will not block the photoresist stripper and make it easy to flow through the undercut and solve the photoresist residue fast. Note that the develop time is very important in lift off process. If the time is too long the whole photoresist layer will be lift off, on the other hand, the under cut may not be formed.

The detailed photolithography procedures, adjustable parameters and recipe for this work are listed in Appendix 2.

Fig. 4.6 The E-beam evaporation equipment BJD1800 in SIMM clean room

4.3 AlN Insulator Layer Depositions

In order to deposit AlN insulator to the substrate, the original substrate holder cannot be used since we don't want to cover the whole area of the device by the insulator. Therefore, a PSMBE compatible mask which is able to control the deposition area and its support holder have to be designed first. Based on the Table 2-1, the layout and parameters of the mask shown in Fig. 4.7 are determined and drawn in AutoCAD 2005 where the small rectangles are the insulator area. Since the material for all holder parts inside the PSMBE are molybdenum (high melting point), the mask is also made of molybdenum considering the heat expansion during deposition. The mask and the holder are fabricated in the engineering school machine shop of Wayne State University. The alignment between the mask and the substrate devices is shown in Fig. 4.8. The flat part at the bottom of the mask is used to make the alignment.

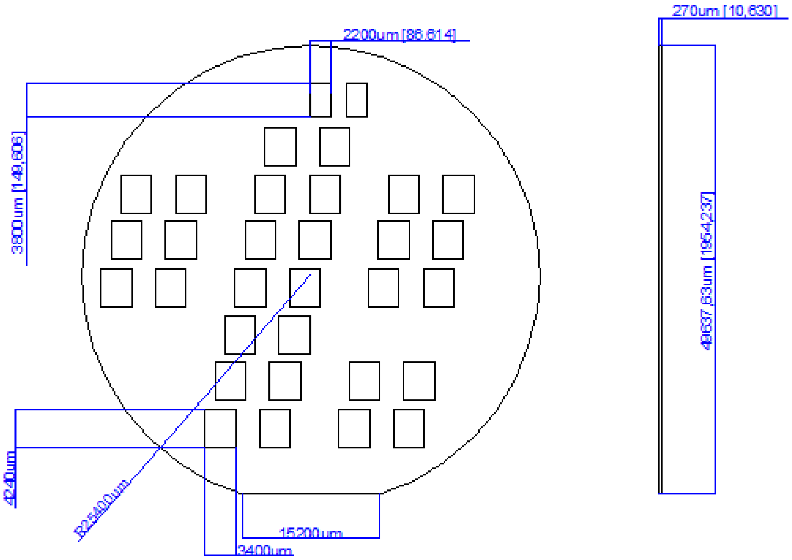

Fig. 4.7 The layout and design parameters for PSMBE compatible mask

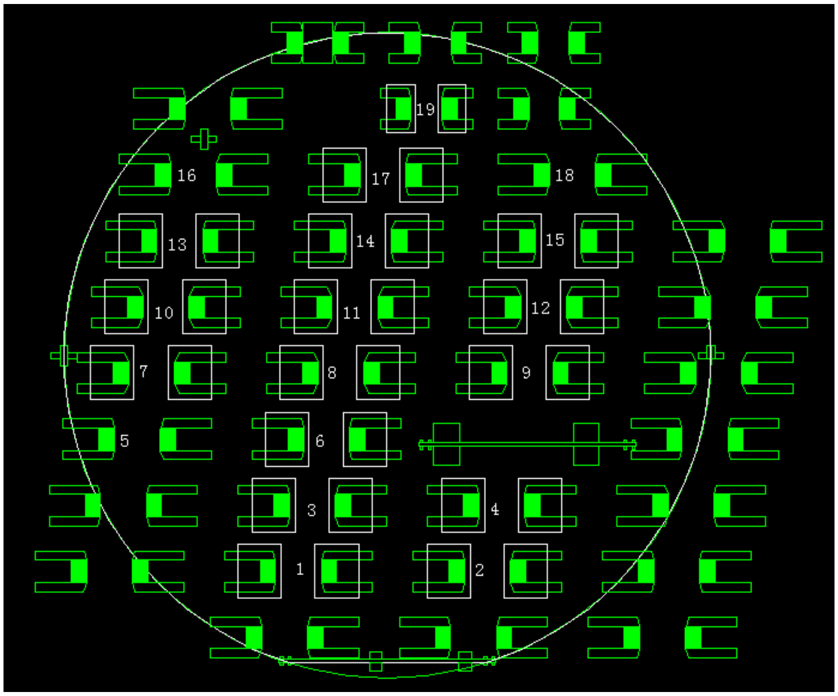

Fig. 4.8 The alignment between the insulator mask and the substrate

Similarly the substrate holder is also designed with AutoCAD 2005 and shown in Fig. 4.9. The material of the holder is molybdenum and the screws are made of Tantalum. Besides the center hold for 2 inch wafer three additional rectangle holes are open for the small samples that can be utilized in X-Ray Diffraction (XRD) test .

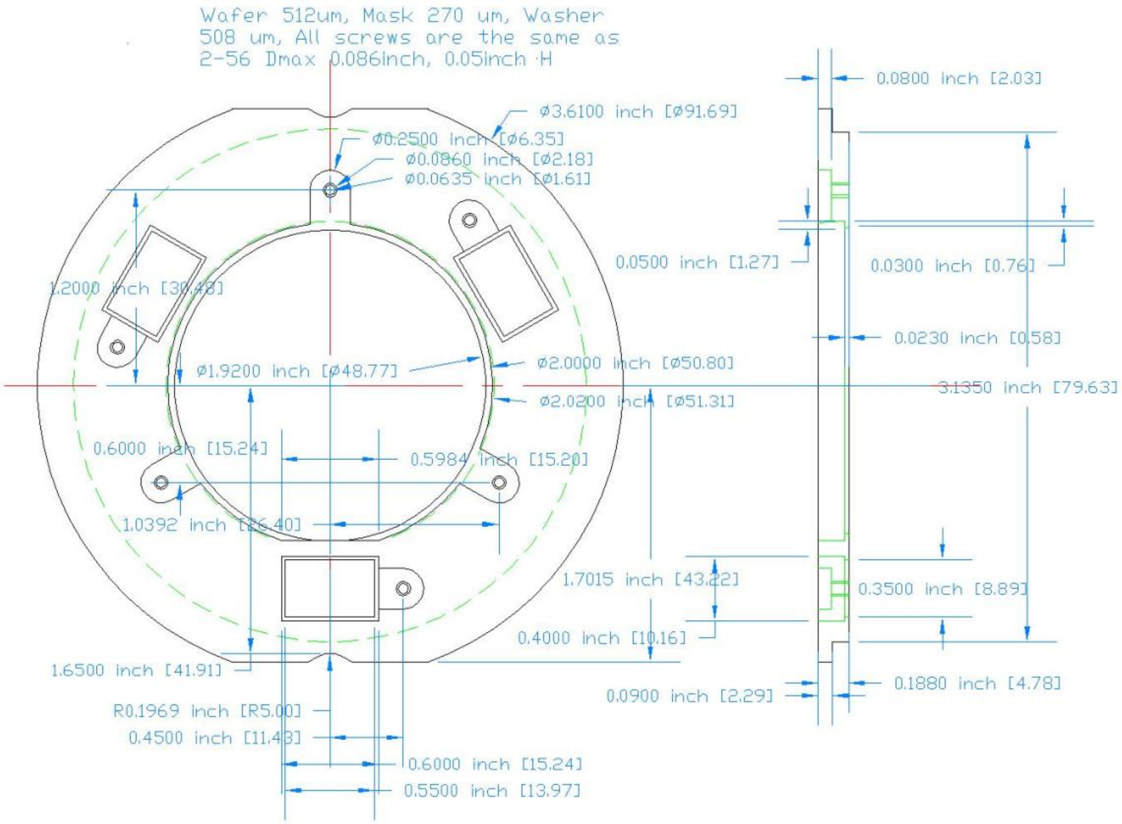

Fig. 4.9 The schematic and design parameters for PSMBE compatible holder

The deposition process is similar to the AlN deposition stated in the section 4.1.2. The only difference is that the deposition temperature can not exceed the IDT melting point 660°C (580°C-740°C) otherwise the IDT will be damaged. During the deposition the RHEED pattern can be observed to examine if the crystal structure is good or not. In order to clean the surface of the substrate before and after the deposition, the plastic holders for 2 inch wafer and 1 inch wafer are designed and shown in Figs 4.10 and 4.11, respectively. The plastic ring to clamp the wafer is designed shown in Fig. 4.12.

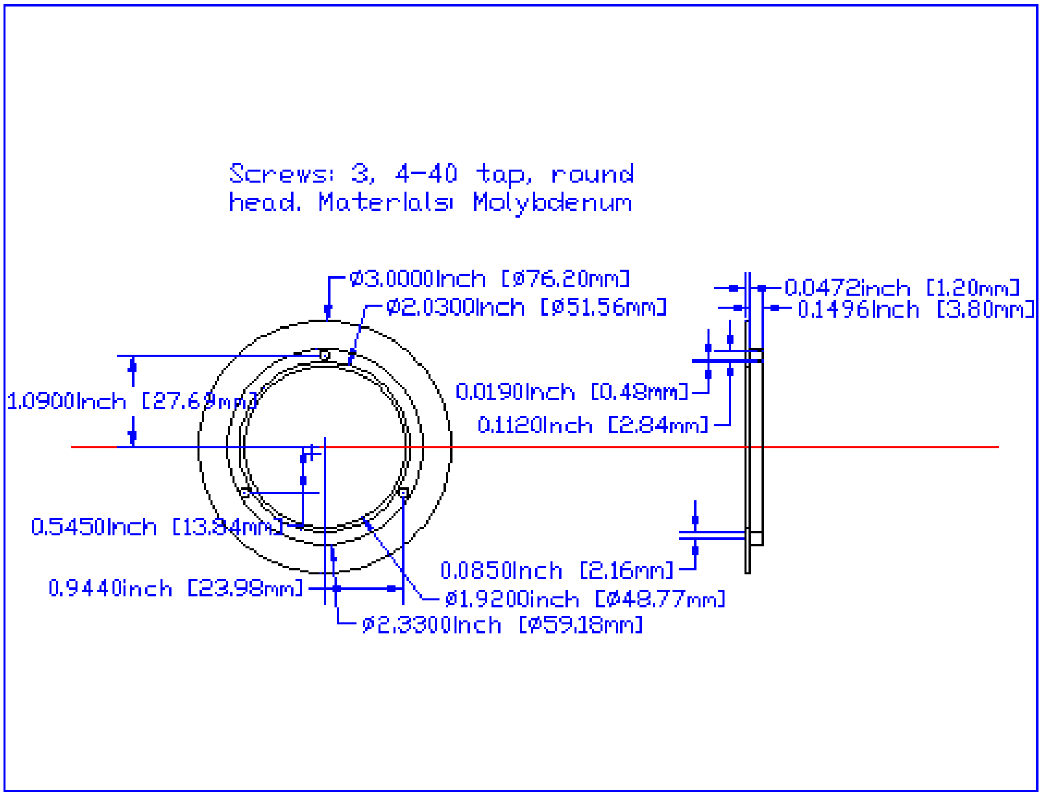

Fig. 4.10 The layout and design parameters of the plastic holder for two inch wafer

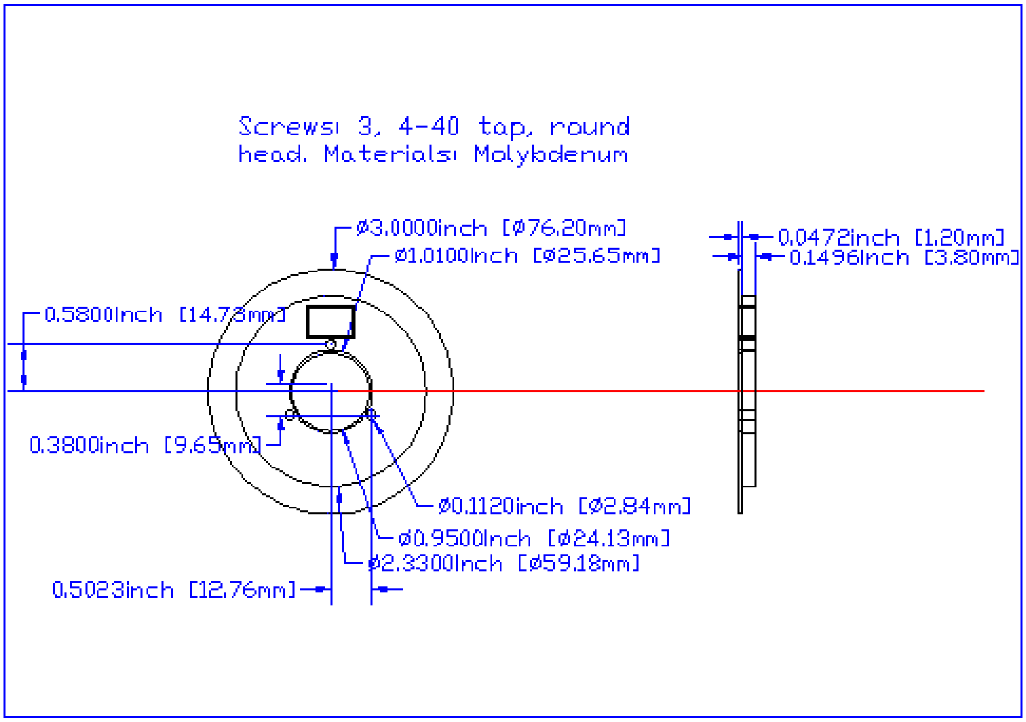

Fig. 4.11 The layout and design parameters of the plastic holder for 1 inch wafer.

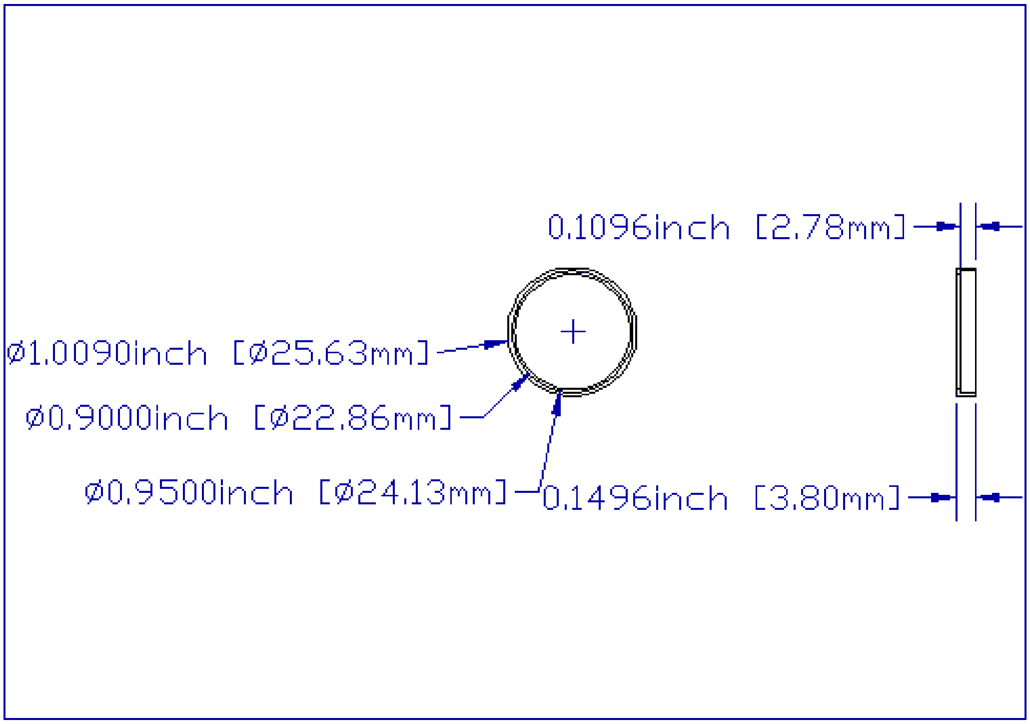

Fig. 4.12 The layout and design parameters for the plastic holder covering ring.

With the XRD measurement, the crystal structure of the material in each layer is characterized. We also examine the surface of the device with the optical microscope. The results are shown in Figs. 4.13 and 4.14. The blue rectangles in the figures show the insulator region. The aureole indicates the thickness change at the insulator boundary. The IDT fingers can be clearly observed from the detailed view. From one wafer, several devices are successfully deposited.

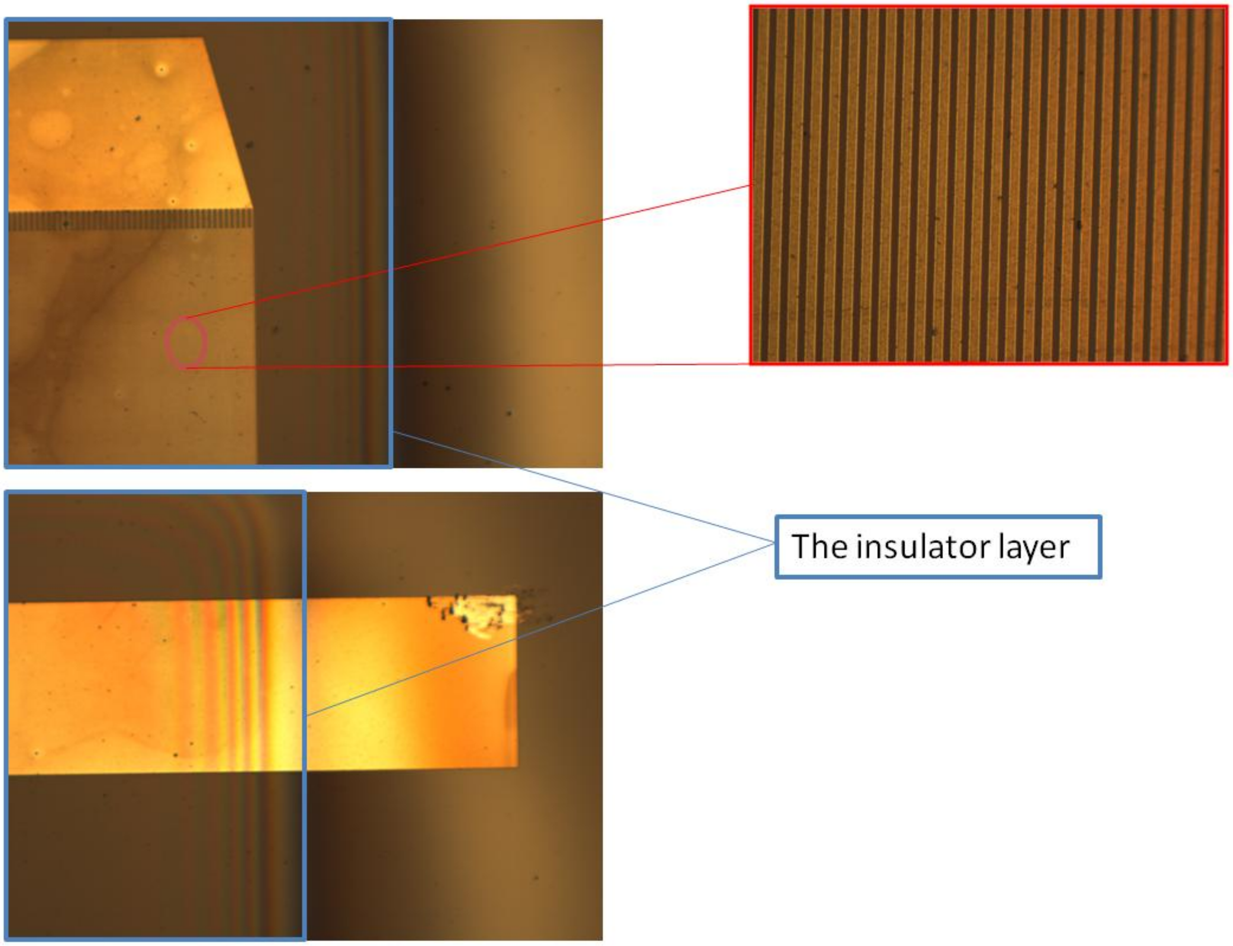

Fig. 4.13 The device surface under the optical microscope. The device #3 is shown above.

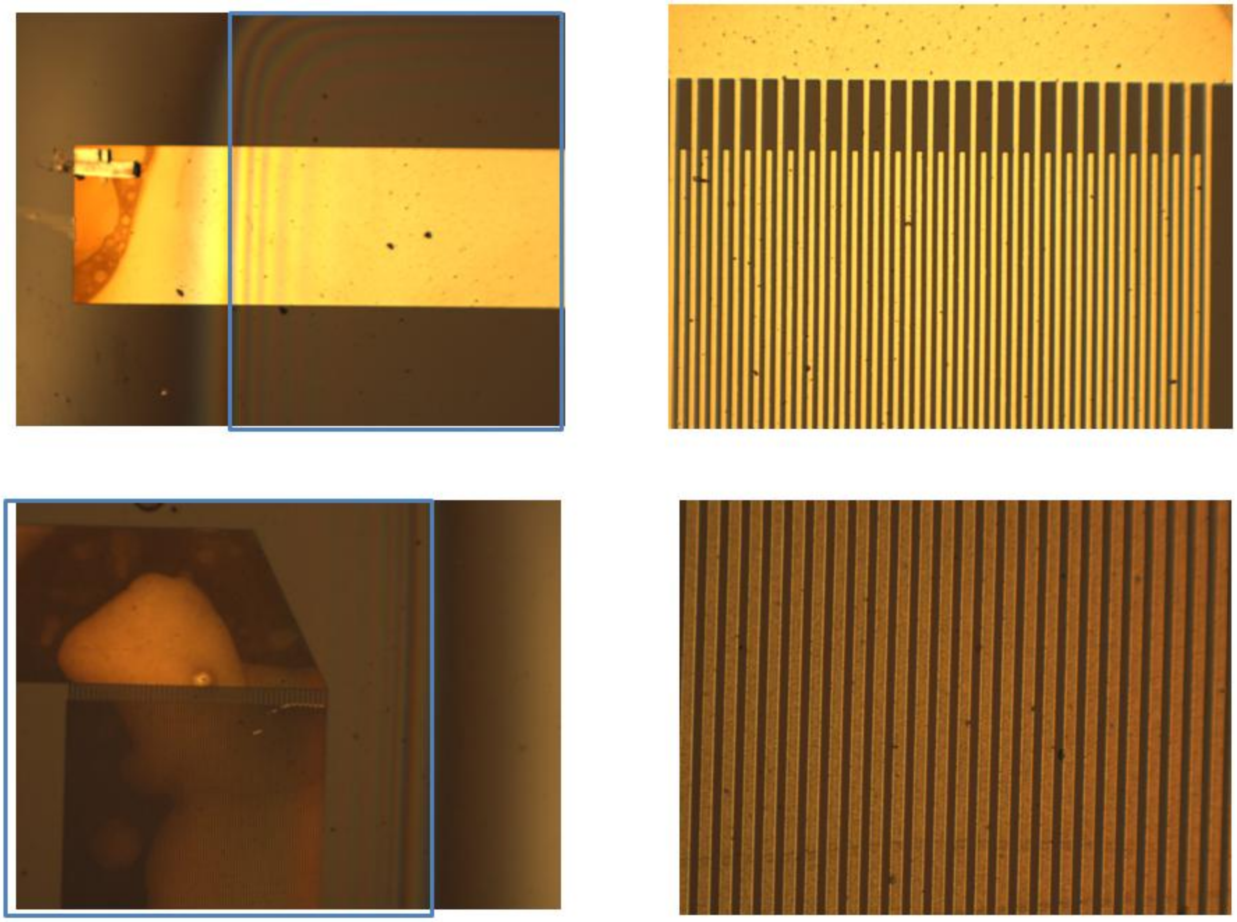

Fig. 4.14 The device surface under the optical microscope. The device #8 is shown on the top and the device #9 is shown on the bottom.

With the Labview® program and the network analyzer, the frequency response for each device is acquired before and after insulator deposition (shown in Figs. 4.15 - 4.19). From Figs. 4.16, 4.18 and 4.19, the amplitude is attenuated by 5-30 db with the AlN insulator. From Fig. 4.17, the amplitude is increase by 3 db which possibly caused by the piezoelectric insulator enhancement. The reason for different insulator impaction is possible from the crystal quality of the insulator. Since too many factors e.g. if the surface is clean enough may affect the quality, its common that different performances appear from different devices on the same wafer. The center frequency is also shifted due to the insulator mass loading. These results coincide with our FEM simulation results and partially validate our FEM analysis.

Comparing with the previous work on coatings ([2]), the AlN coating has smaller attenuation/thickness ratio. Furthermore as we discussed in Chapter 1 the physical and chemical stability of AlN is the best among these possible coatings.

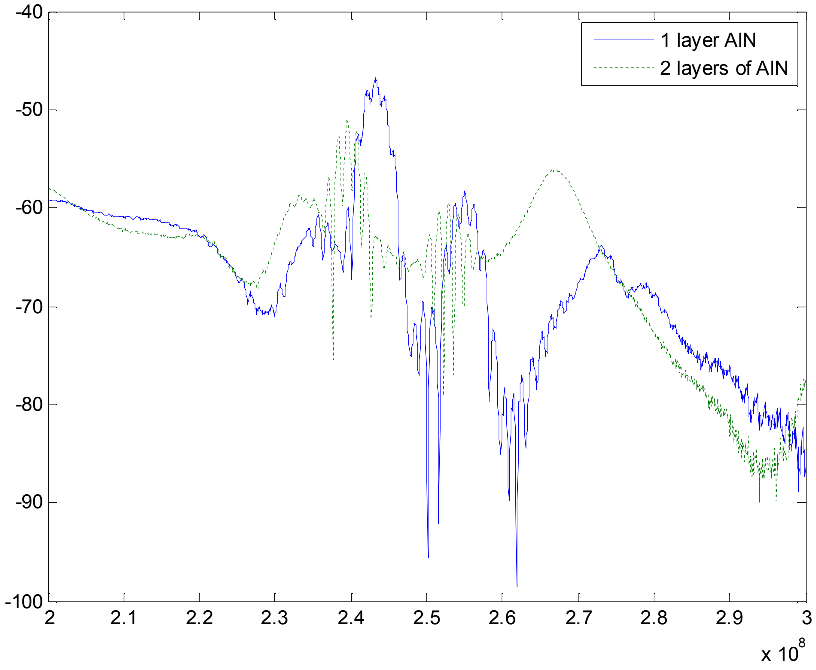

(a)

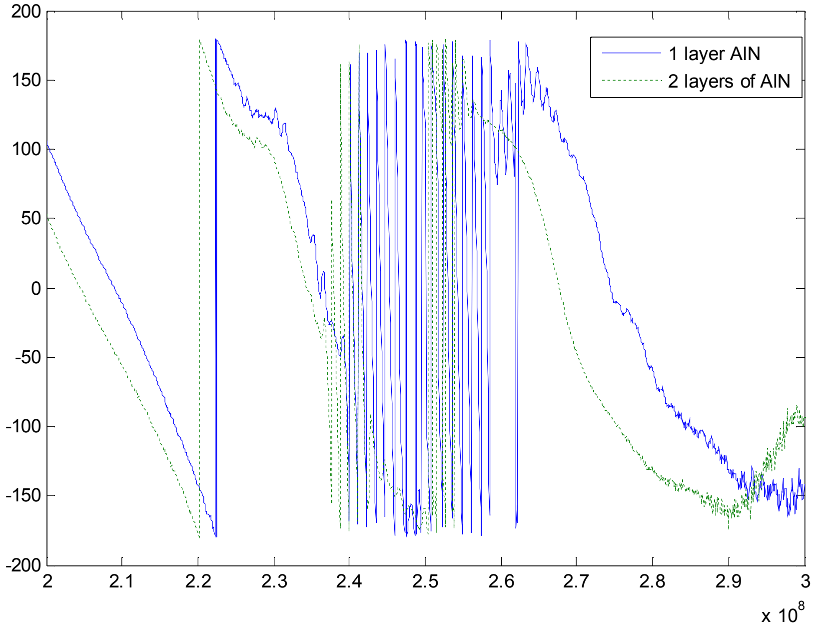

(b)

Fig. 4.15 The frequency response for device # 3. (a) Amplitude (b) Phase

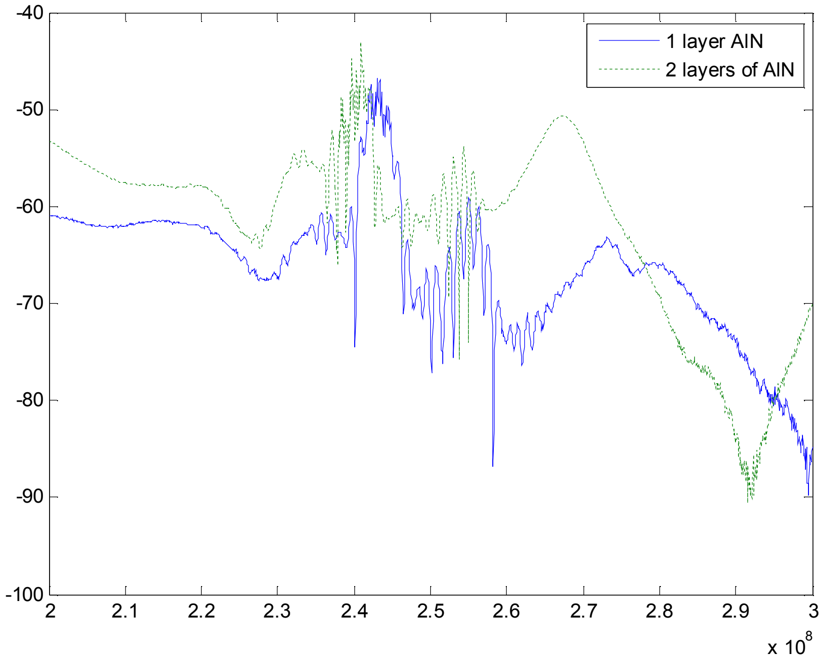

(a)

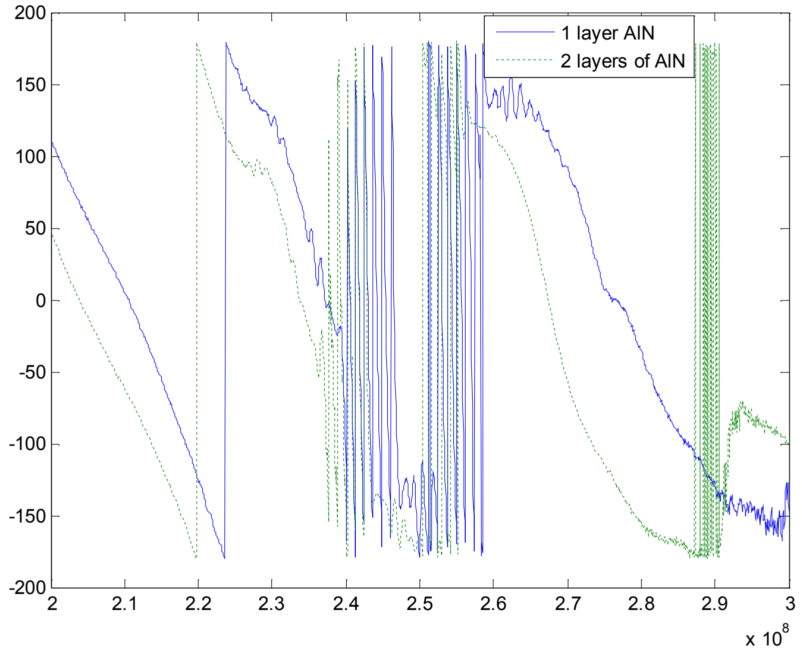

(b)

Fig. 4.16 The frequency response for the device # 8 (a) Amplitude (b) Phase

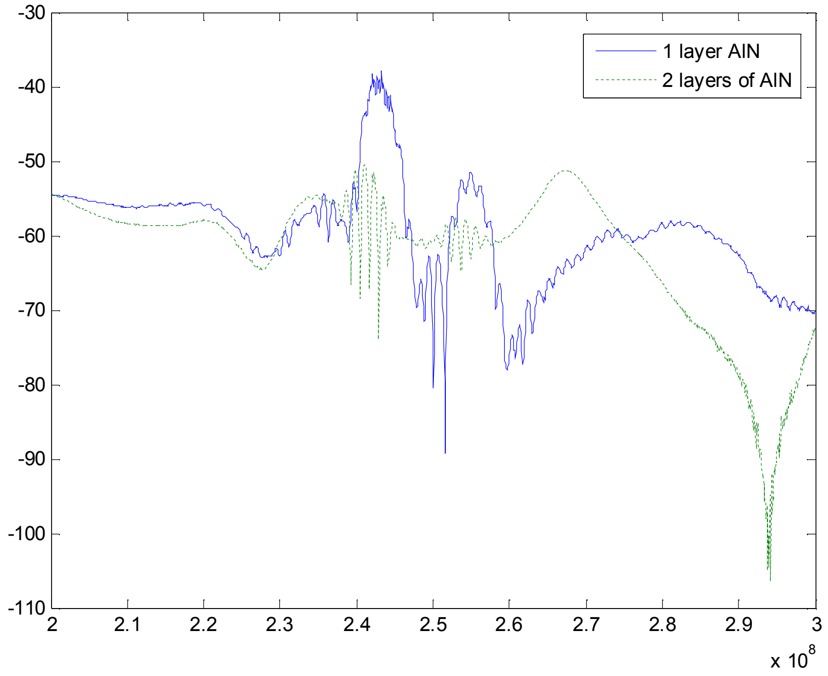

(a)

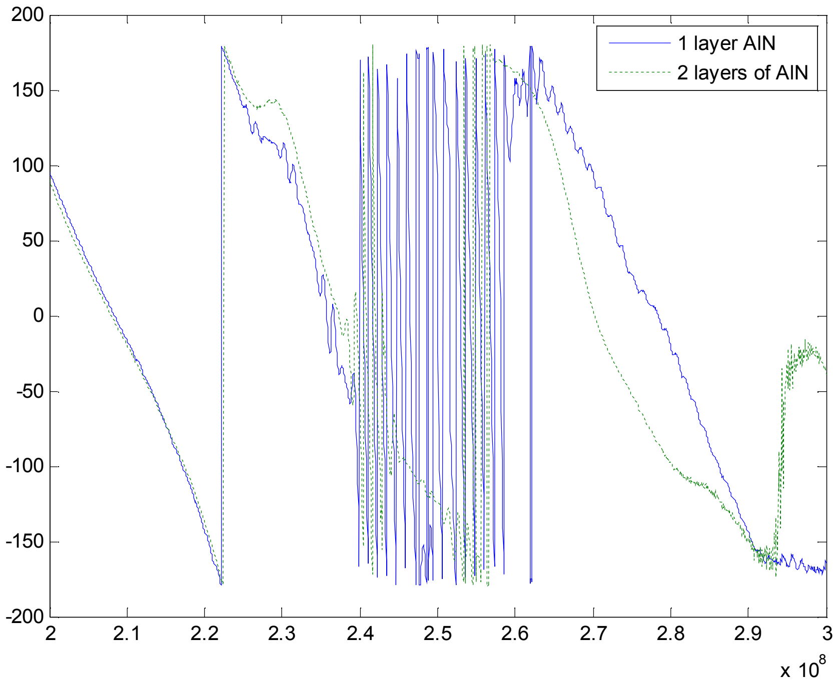

(b)

Fig. 4.17 The frequency response for device # 9 (a) Amplitude (b) Phase.

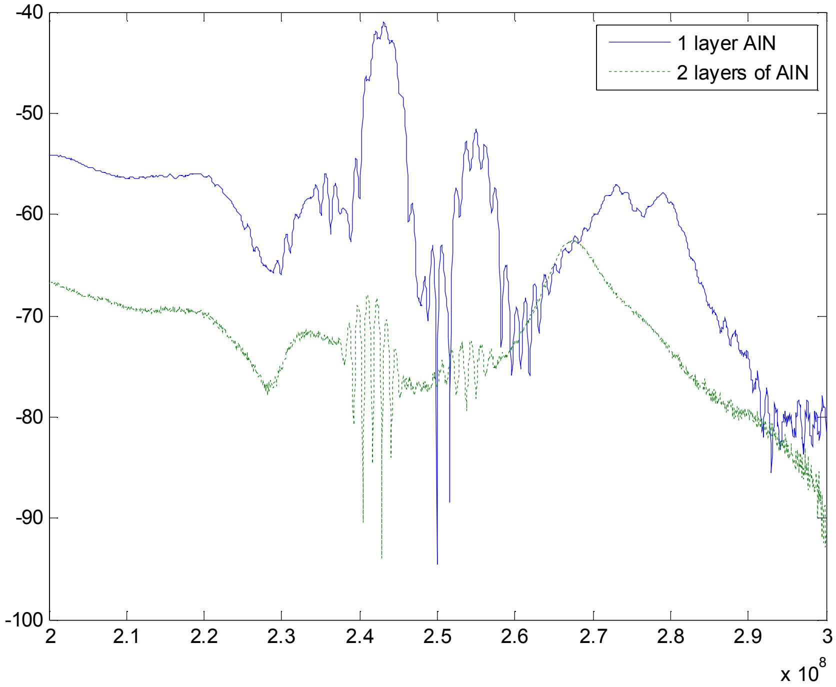

(a)

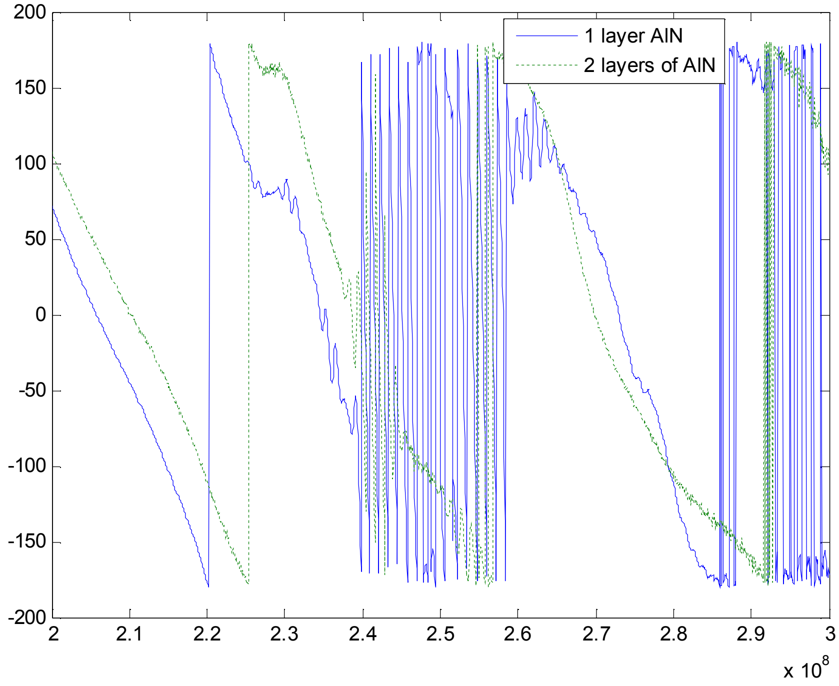

(b)

Fig. 4.18 The frequency response for device # 15 (a) Amplitude (b) Phase.

Table 4-1 Comparison between different coatings on AlN-based SAW Device [2]

Coating Layers	Thickness (nm)	Attenuation on SAW (db)	Attenuation on SH-SAW (db)
LOR 1A	140	0	0
LOR 3B	780	2	25
SiO_2	500	2	10
AlN	1500	-3	-5

CHAPTER 5 SYSTEM INTEGRATION AND DEVELOPMENT

In order to build the whole pressure sensor system, the electric circuit and some signal processing algorithms are developed in this section. First a prototype system is set up using separate electric components to evaluate the baseline performance. Some algorithms are developed to capture the sensing signatures. The thermo stability of the system is then investigated to test the system robustness in various environments. The portable electric circuit is designed based on the prototype system at last.

5.1 Frequency Measurement System Setup

As pointed out in the Chapter 2, the possible sensing signatures of SAW devices are frequency, phase and amplitude. Considering the system robustness [180], the frequency and phase measurements are the most two common ways to sense the pressure. For the phase measurement system, the phase difference for the signal excited by an external signal generator passing through the sensor or bypass the sensor is the sensing signature. While for the frequency measurement system, the frequency of the signal self-excited by a loop containing the device is the interest. Considering the system complexity, in this work, the frequency measurement scheme is employed.

The system contains a self-excited loop and a frequency measurement device which is shown in Fig. 5.1. As we know the condition of a self-excited closed loop system is that the total loop gain is greater than 0 db and the loop phase is equal to $2k\pi$ where k is an integer. From Figs. 4.16-4.19, the phase range over the pass band of our device is [-π, π], so the phase balance condition can be neglected here. Only enough amplifiers and proper band-pass filter are required to guarantee the maximum loop gain is over 0 db and locates at the desirable frequency band.

As a starting point, some separate components are employed to implement the frequency measurement scheme which are listed in Table 5.1. Either an oscilloscope or a frequency counter can be used as the frequency measurement device. In this work both the frequency counter HP/Agilent 53131A and the oscilloscope HP/Agilent 54852A are used to evaluate the corresponding estimation algorithms. Similar to the phase detection system in [2], The differential set up is adopted in this work by using two identical set of components. Each set contains two/three 18 db amplifiers, one AlN-based SAW device, one band-pass filter and one Power splitter. The frequency difference between two neighboring identical SAW devices is the system output.

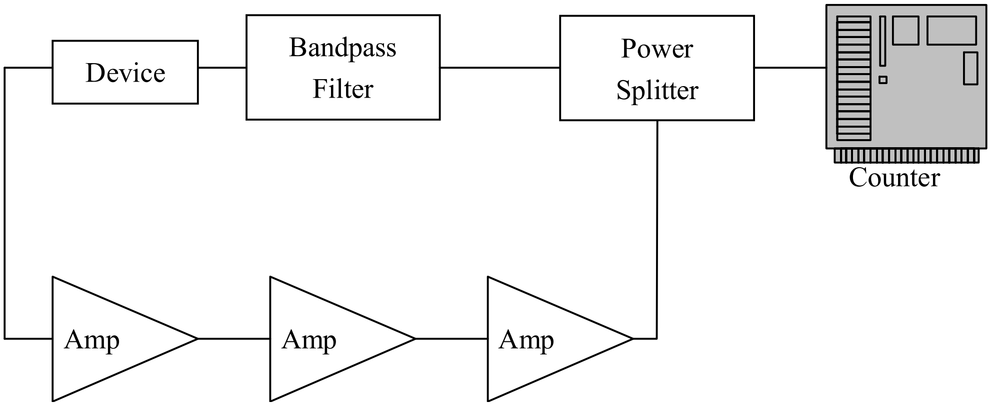

Fig. 5.1 Schematic diagram of single device frequency measurement system

Table 5.1 Components list for frequency measurement system

Name	Quantity	Model	Corp

Amplifier	4	ZFL-750	Mini-circuit ®
Filter	1	5VF200/400-5-50-KK	Trilithic®
Power splitter	2	ZFSC-2-1W	Mini-circuit®
SMA Cable	10	J3306-ND	Digi-key®
SMA Cable(long)	5	J3324-ND	Digi-key®
Frequency Counter	1	HP 53131A	HP/ Agilent®
Oscilloscope	1	HP 54852A	HP/Agilent®

5.2 Frequency Estimation Algorithms

The output of the SAW device is an electrical signal with time-varying voltage. To acquire the pressure value the frequency of the signal needs to be estimated. The common estimation algorithms include, fast Fourier transform (FFT) [181], interpolated FFT [182-183], zero-crossing method [184], sine-wave fitting [185], Kalman filter [186], Chirp-Z transform [187], short-time Fourier transform [188], etc. Here frequency estimation using FFT is to look for the strongest component in frequency domain while an interpolated FFT interpolate the spectrum from FFT by utilizing the knowledge of the sampling window shape and pure sine wave source. The latter is able to achieve better accuracy from the same data. Chirp-Z transform is based the z transform and estimate the frequency in the frequency domain. The sine-wave fitting is a time-domain method to estimate frequency with least square optimization. Kalman filter is a system identification approach and it’s fit for distorted or time-varying signals. Zero-crossing is an easy implemented time-domain algorithm which estimates the frequency by calculating the time between two cross-zero points. The computation burden is the smallest among all estimation algorithms. A more detailed comparison can be found in [189].

In this work two estimation schemes are employed. The first one is to use the oscilloscope to sample output data. Then the interpolated zero-crossing method is used to obtain the estimated frequency. The moving average method is applied to remove the signal noise. The flow chart of the estimation process is shown in Fig. 5.2.

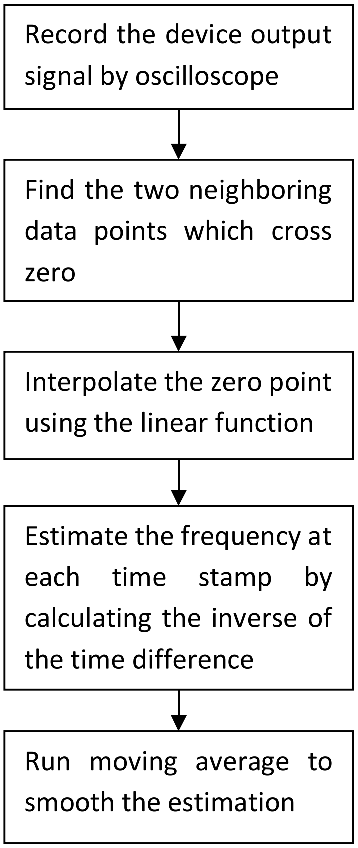

Fig. 5.2 The flow chart of frequency estimation approach using the oscilloscope.

To validate the algorithm, the device No. 16 was used in our differential frequency measurement system. The frequency estimation results without moving average for both channels are shown in Figs. 5.3 and 5.4 respectively where no pressure is imposed on the device. One can observed that the frequency value for either channel is not stable due to the environment change (i.e. temperature). The differential result shown in Fig. 5.5 is more stable than either single channel indicating the differential configuration helps to weaken the environment impaction.

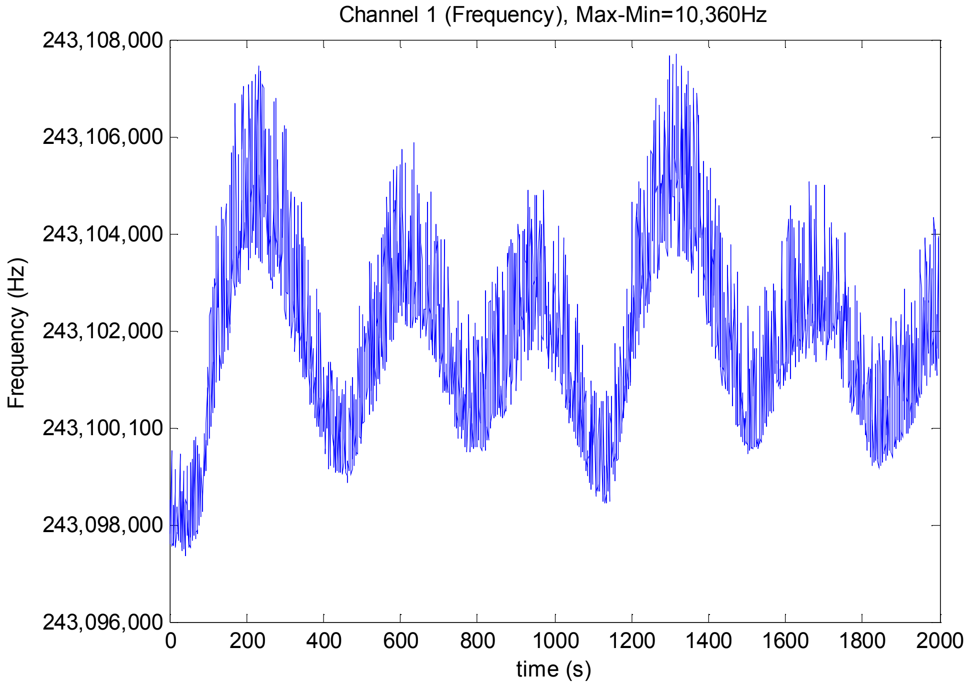
Channel 1 (Frequency), Max-Min=10,360Hz

Fig. 5.3 The frequency estimation result for differential system channel 1

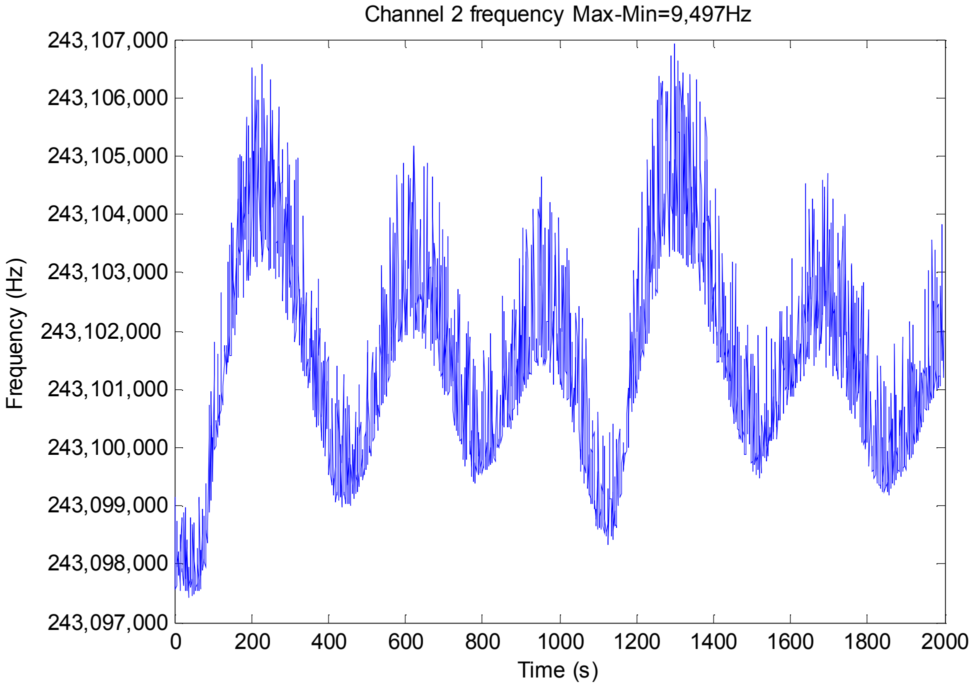

Fig. 5.4 The frequency estimation result for differential system channel 2

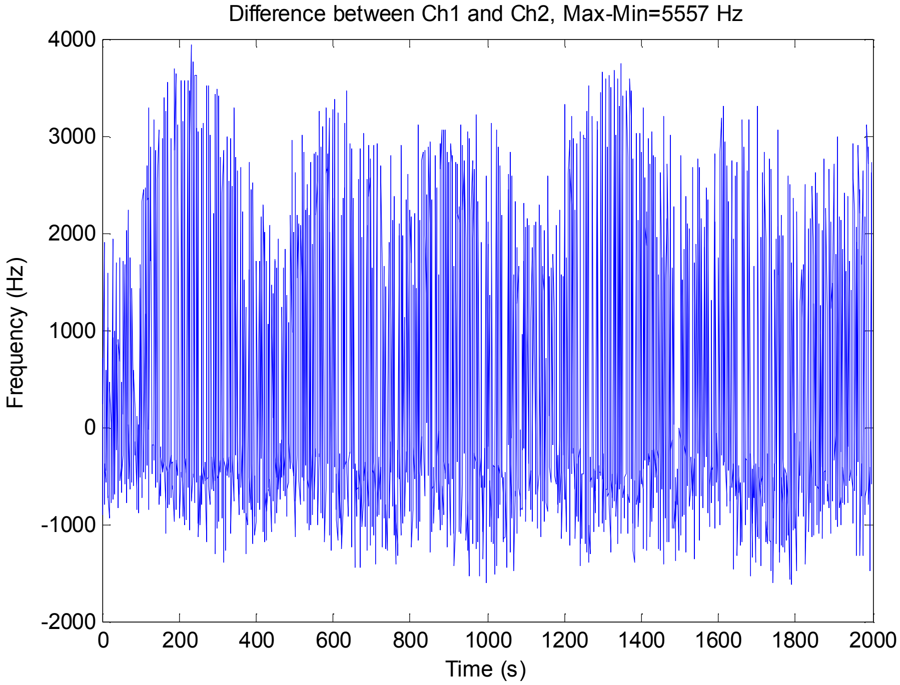

Fig. 5.5 The frequency estimation result for differential system

Since the range of differential output is still very large (i.e. the measurement system is not stable), the 101-point moving-average is employed to filter the differential output. Shown in Figs. 5.6 and 5.7, after the moving-average step, the stability for either the single channel frequency estimation or the differential output is dramatically increased. The range of frequency fluctuation is only 971 Hz.

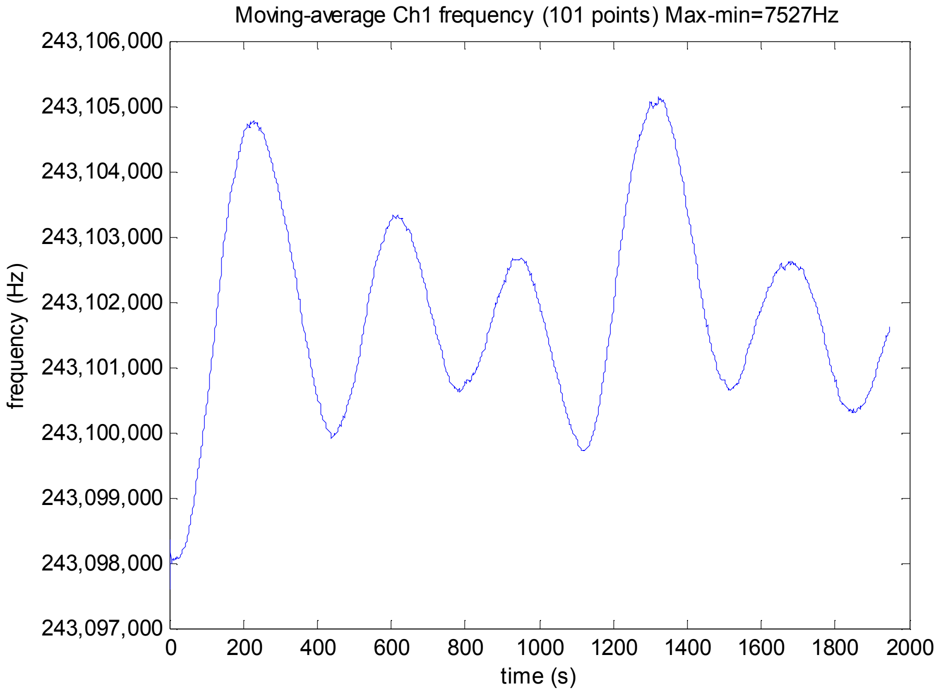

Fig. 5.6 The frequency estimation result for differential system channel 1 after moving-average

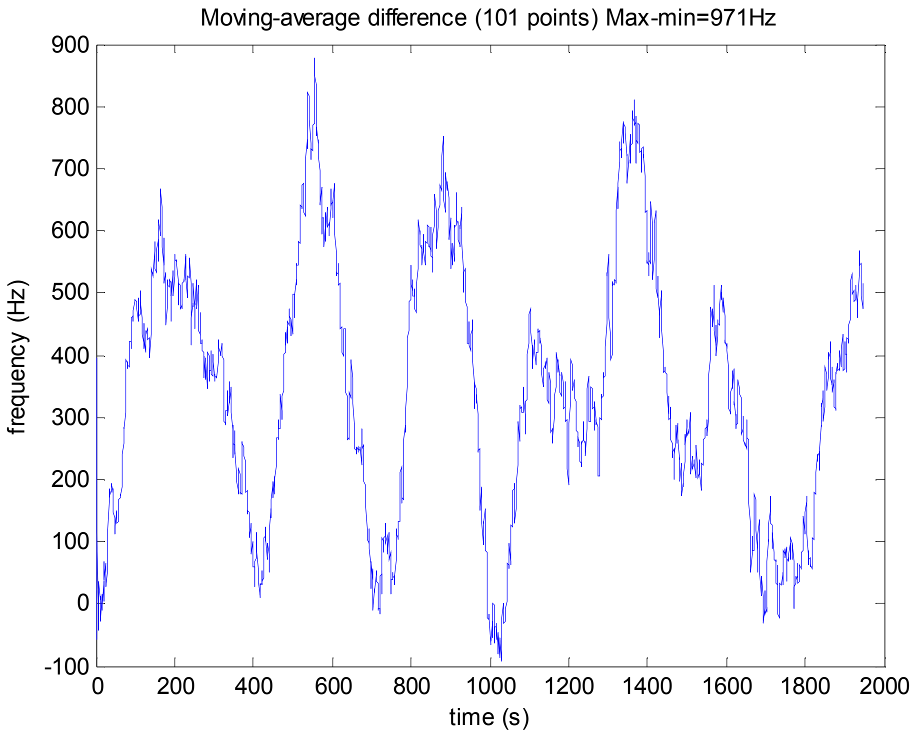

Fig. 5.7 The frequency estimation result for the differential system output after moving-average

Similarly, device #19 was used in the same differential frequency measurement system. The system configuration is exactly same as the above one except for the SAW device. The experiment results are shown in Fig. 5.8, Fig. 5.9, Fig. 5.10, Fig. 5.11 and Fig. 5.12. The results indicate that the differential system can suppress the signal fluctuation from 3495 Hz (Ch1) to 1130 Hz (differential).

.

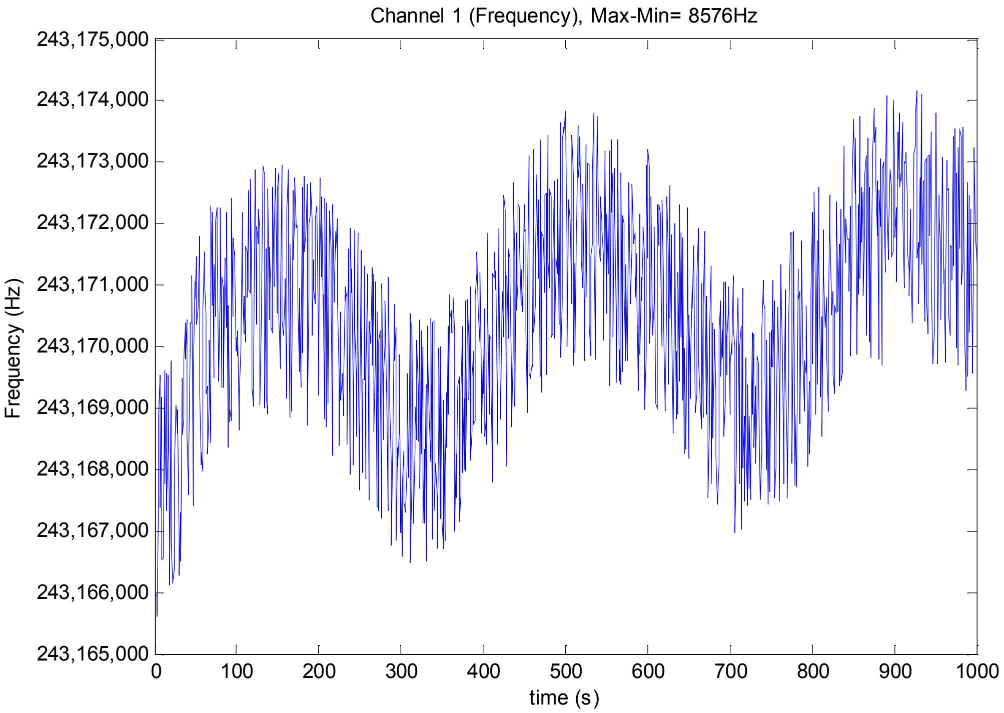

Fig. 5.8 The frequency estimation result for differential system channel 1

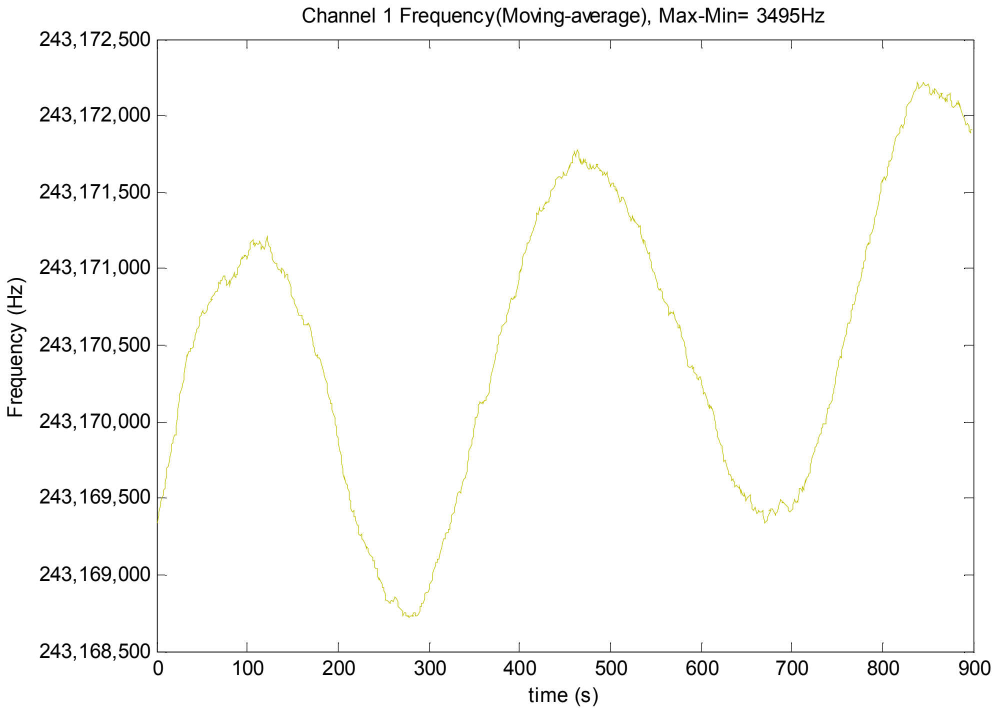

Fig. 5.9 The frequency estimation result for differential system channel 1 after moving-average

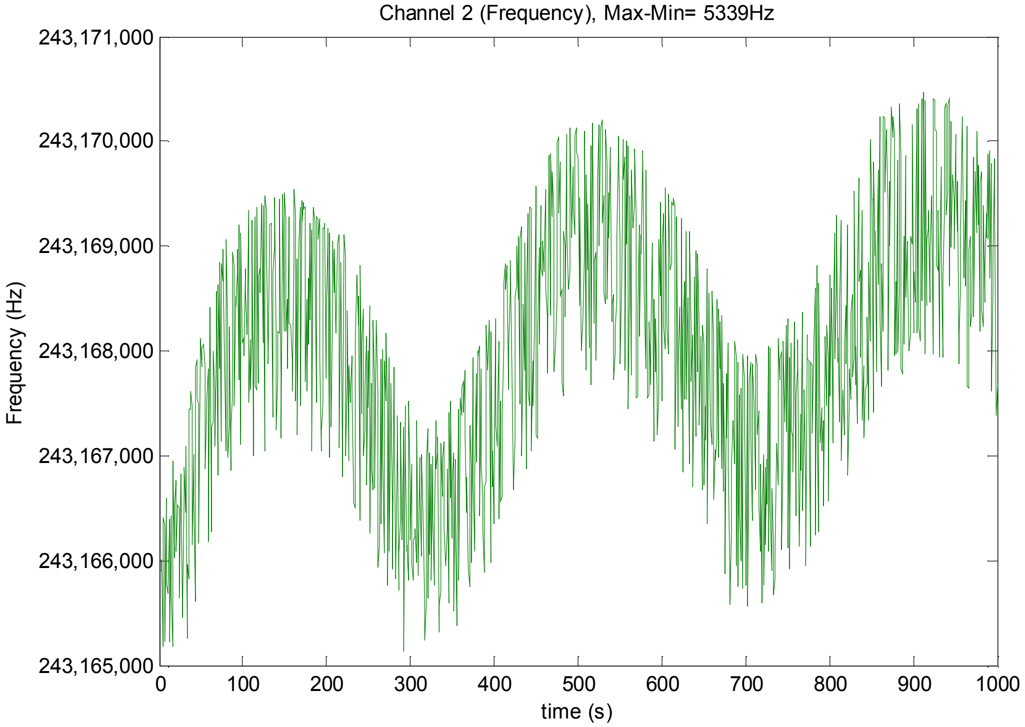

Fig. 5.10 The frequency estimation result for differential system channel 2

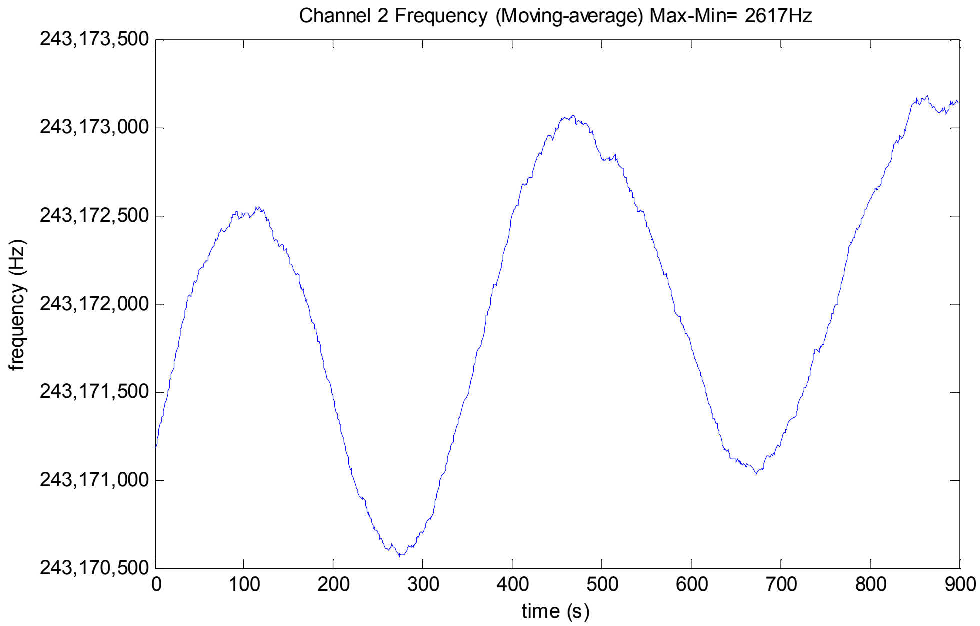

Fig. 5.11 The frequency estimation result for differential system channel 2 after moving-average

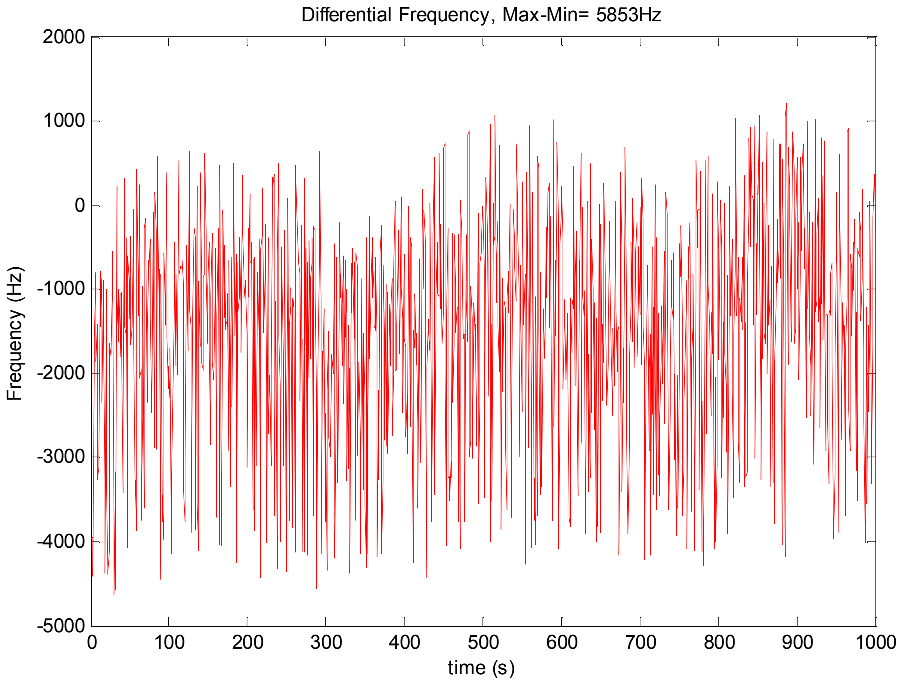

Fig. 5.12 The frequency estimation result for differential system output

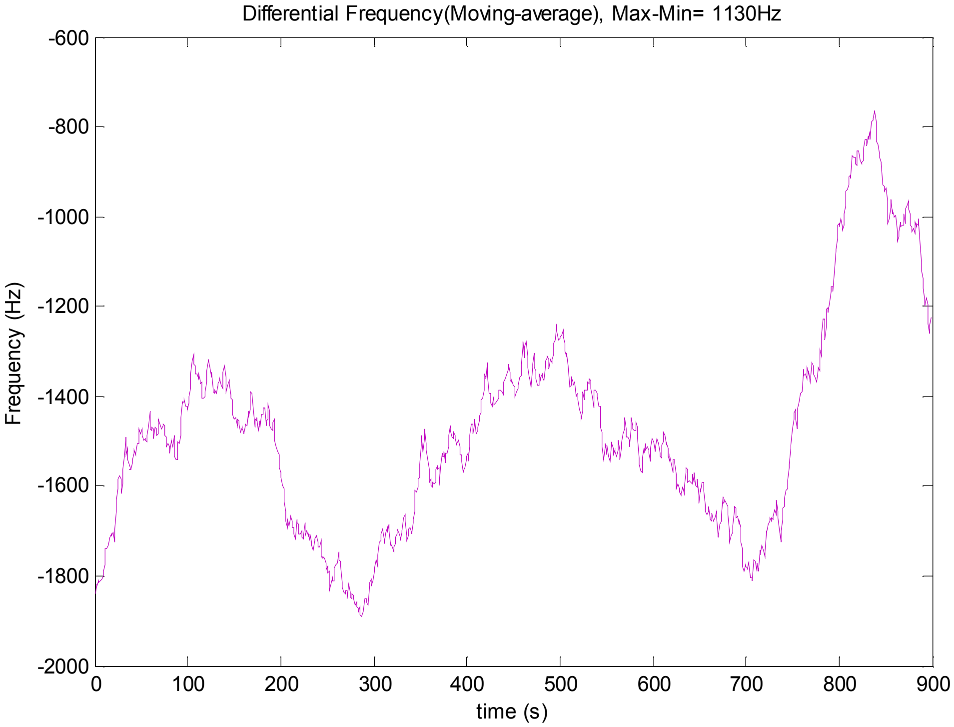

Fig. 5.13 The frequency estimation result for differential system output

In the same fashion, we repeat these baseline experiments for several times in different time. The similar results are achieved and listed in Table 5.2. Comparing the results with references [2, 17], the frequency measurement results are comparable to the phase measurement results using oscilloscope's average sampling mode and worse than the results using oscilloscope's real time sampling mode.

Table 5.2 The experimental results for differential frequency measurement system

Experiment	Sensor	Ch1 (Hz)	Ch2 (Hz)	Difference (Hz)	Corresponding Phase (Mili-degree) (3.4 :1)
1	No. 16 (SAW)	7527	8498	971	286
2		15742	16548	2239	658
3		4209	4481	477	140

4	No. 19 (SAW)	2849	3006	537	157
5		4560	3719	899	264
6		3495	2671	1130	332
7		7066	9620	2596	761

To achieve better results, the frequency estimation using frequency counter is attempt as follows. The estimation process is shown in Fig. 5.14. First, the LabView ® program was developed to record two channels simultaneously using the frequency counter HP53131A. The front panel and block diagram of the program are shown in Figs. 5.15 and 5.16. The differential results are not as good as what we expect. By analyzing the raw data, we found that the sampling time for dual channels sampling are not exactly at the same time stamp. Therefore, we shift channel 2 data backward by half of the sampling interval, the result shows great improvement.

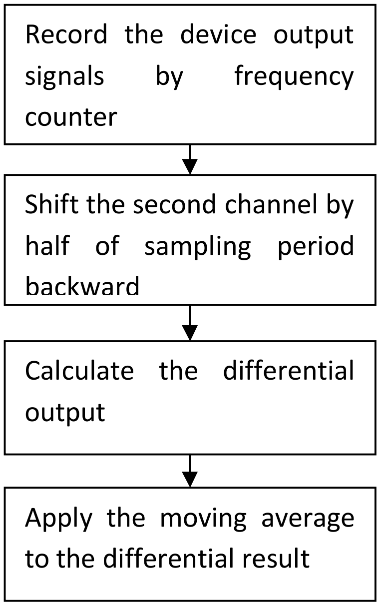

Fig. 5.14 The flow chart of frequency estimation approach using frequency counter

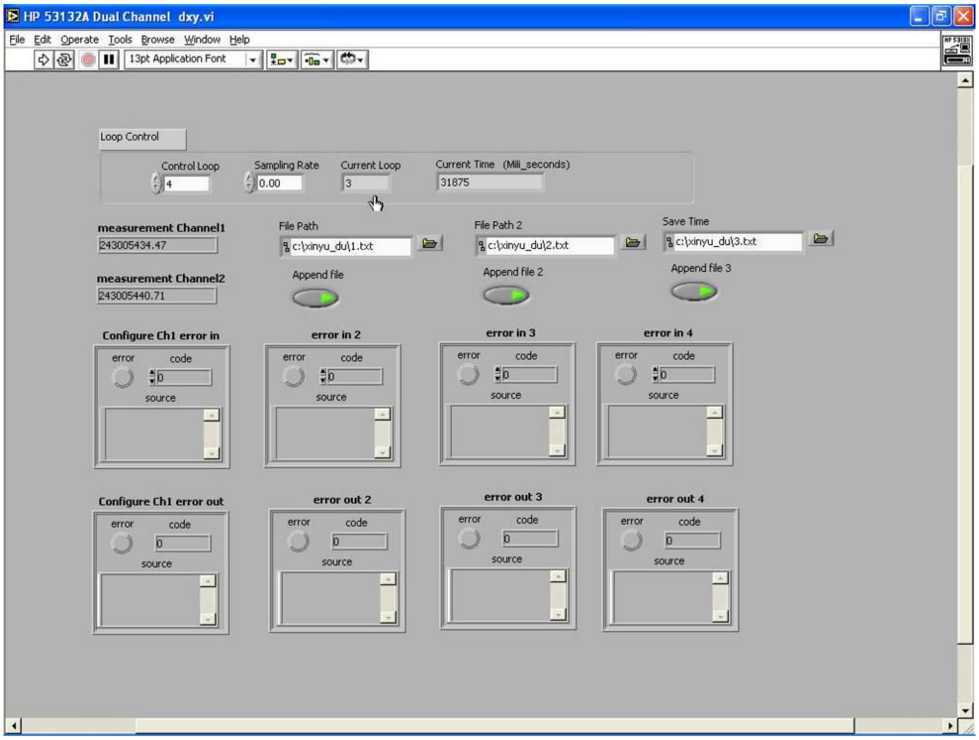

Control Loop: 4
Sampling Rate: 0.00
Current Loop: 3
Current Time (Mili_seconds): 31875
measurement Channel1: 243005434.47
measurement Channel2: 243005440.71
File Path: c:\xinyu_du\1.txt
File Path 2: c:\xinyu_du\2.txt
Save Time: c:\xinyu_du\3.txt

Fig. 5.15 The front panel of the Labview® program

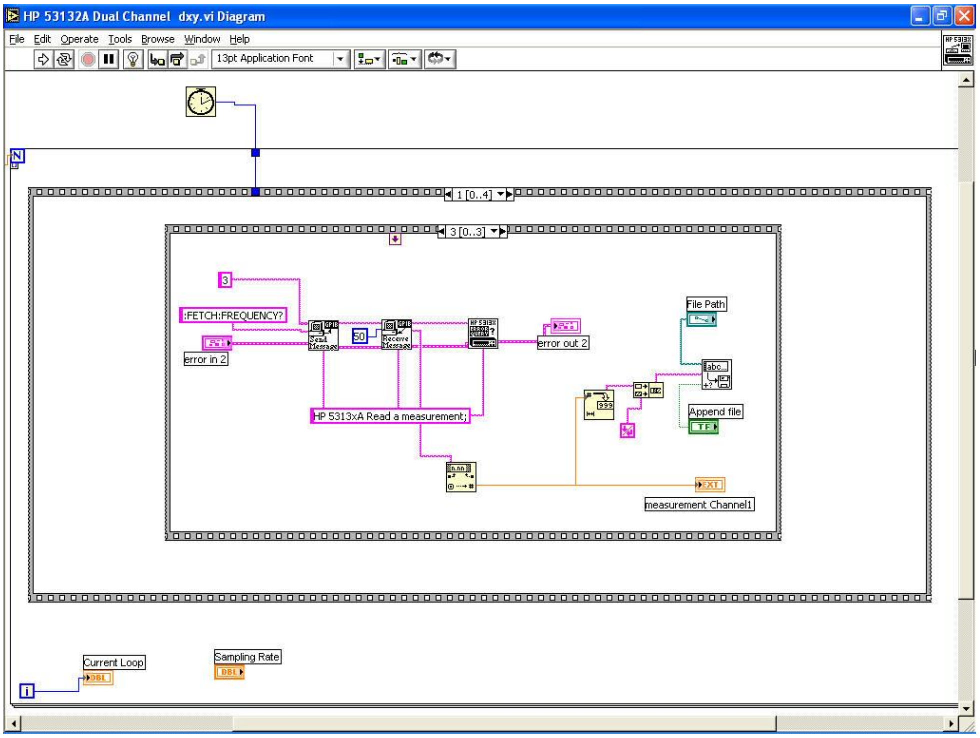

Fig. 5.16 The block diagram of the LabVIEW ® program

To evaluate the second estimation scheme, the stability test without and with channel 2 shift are performed respectively. The results shown in Figs. 5.28 to 5.36 are from three independent experiments without channel 2 shift step. Comparing with the frequency estimation method 1, this method already achieves better stability (the range is only about 100 Hz).

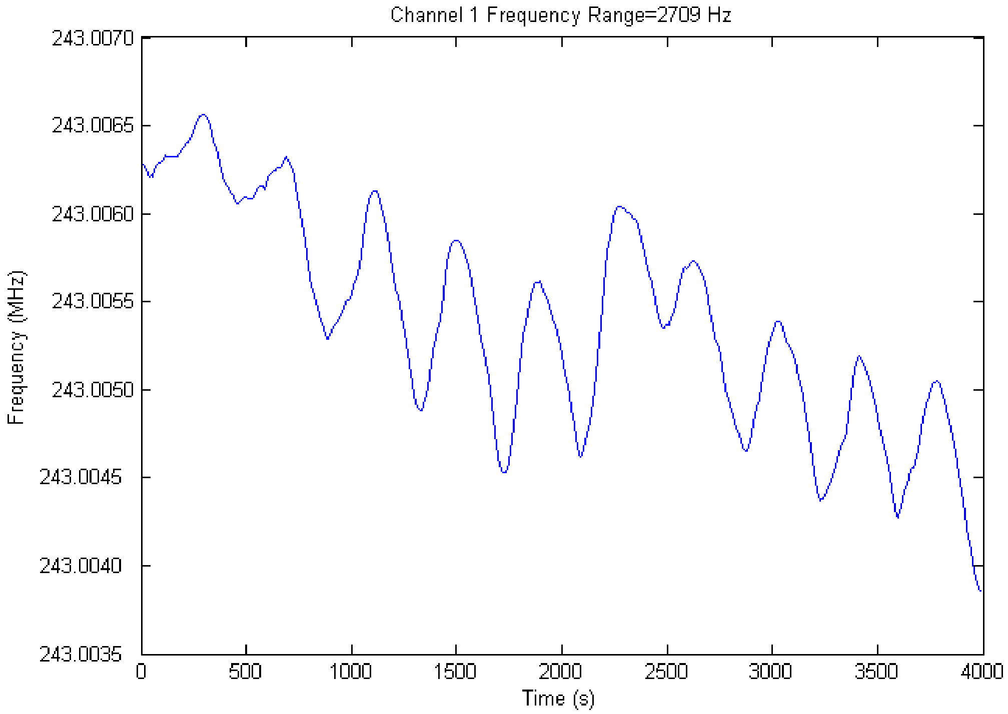

Fig. 5.17 The frequency estimation result for differential system channel 1 in experiment 1

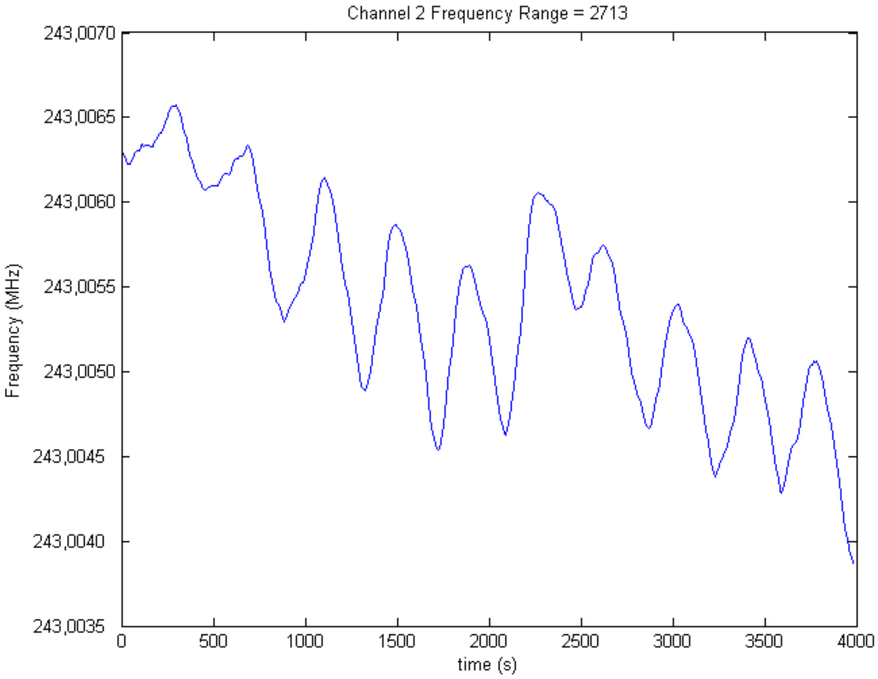

Fig. 5.18 The frequency estimation result for differential system channel 2 in experiment 1

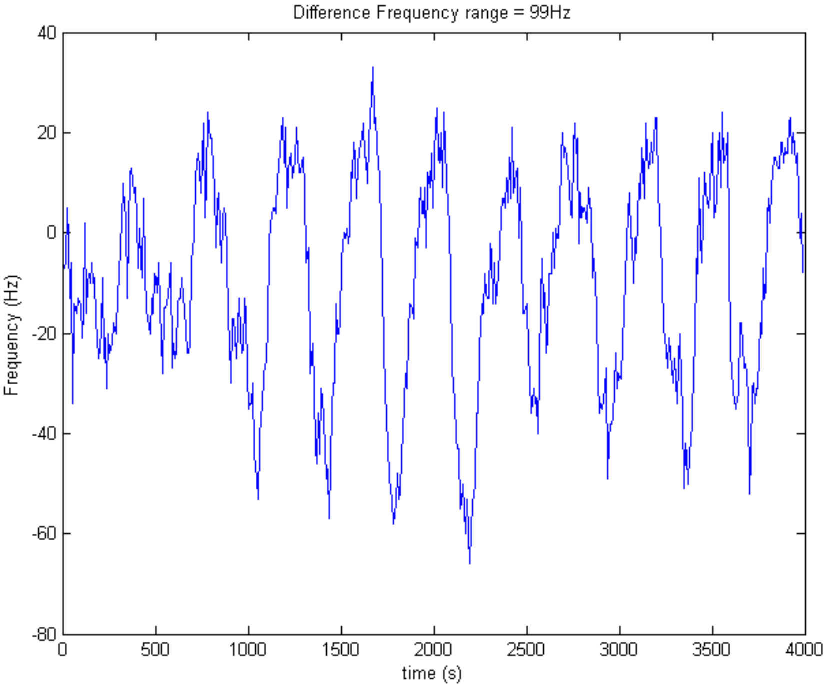

Fig. 5.19 The frequency estimation result for differential system output in experiment 1.

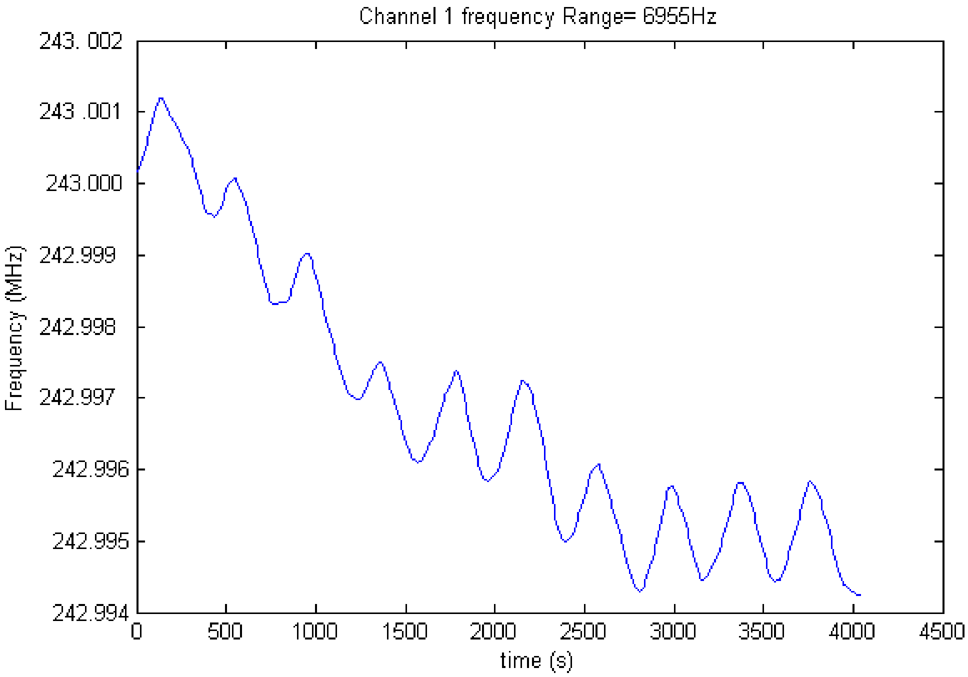

Fig. 5.20 The frequency estimation result for differential system channel 1 in experiment 2

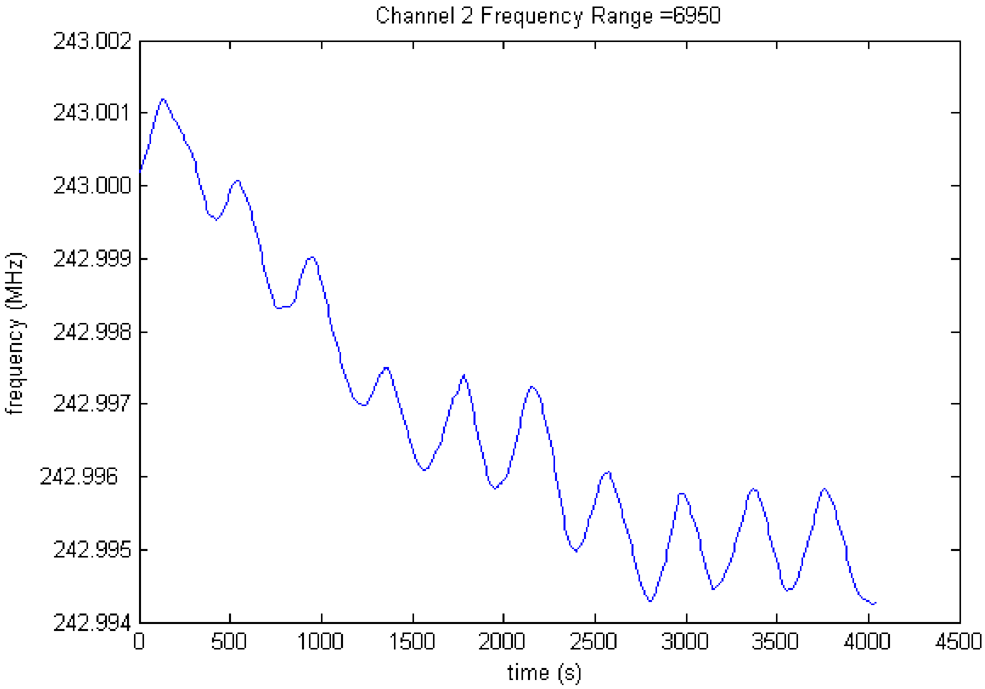

Fig. 5.21 The frequency estimation result for differential system channel 2 in experiment 2

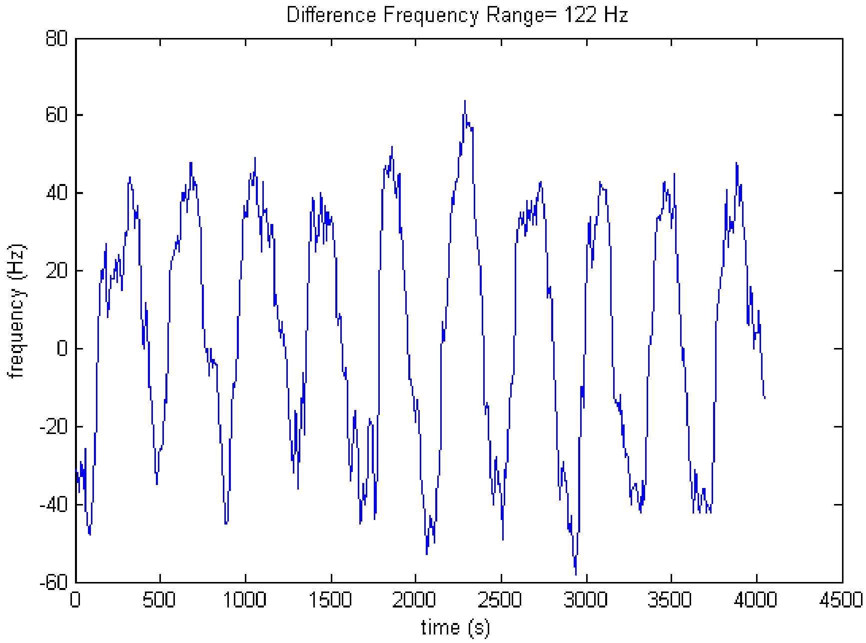

Fig. 5.22 The frequency estimation result for differential system output in experiment 2

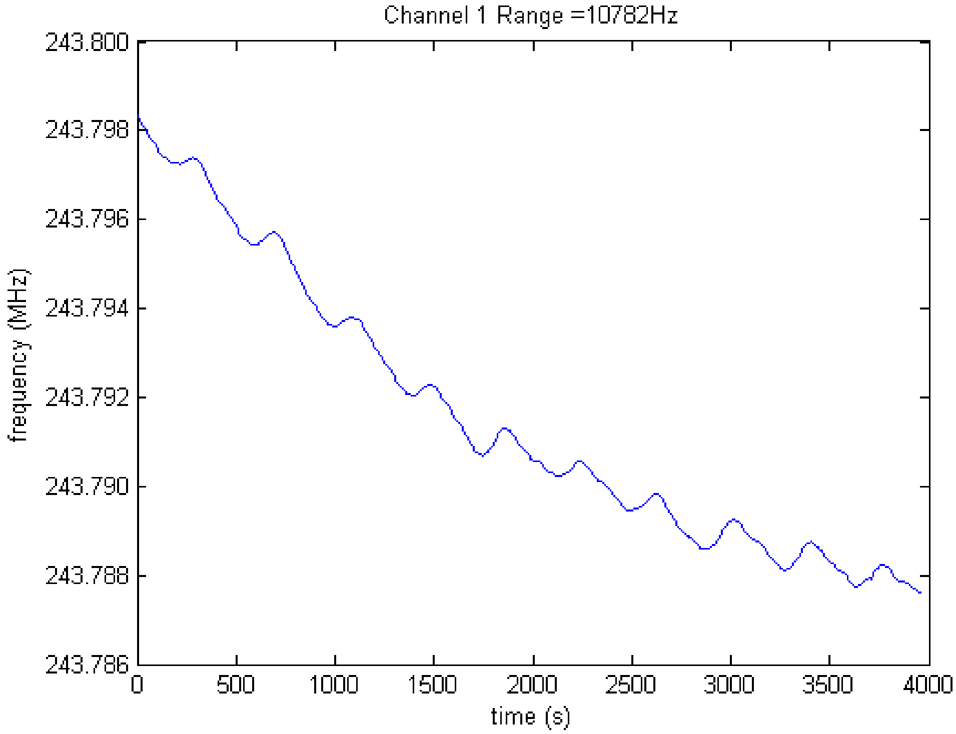

Fig. 5.23 The frequency estimation result for differential system channel 1 in experiment 3

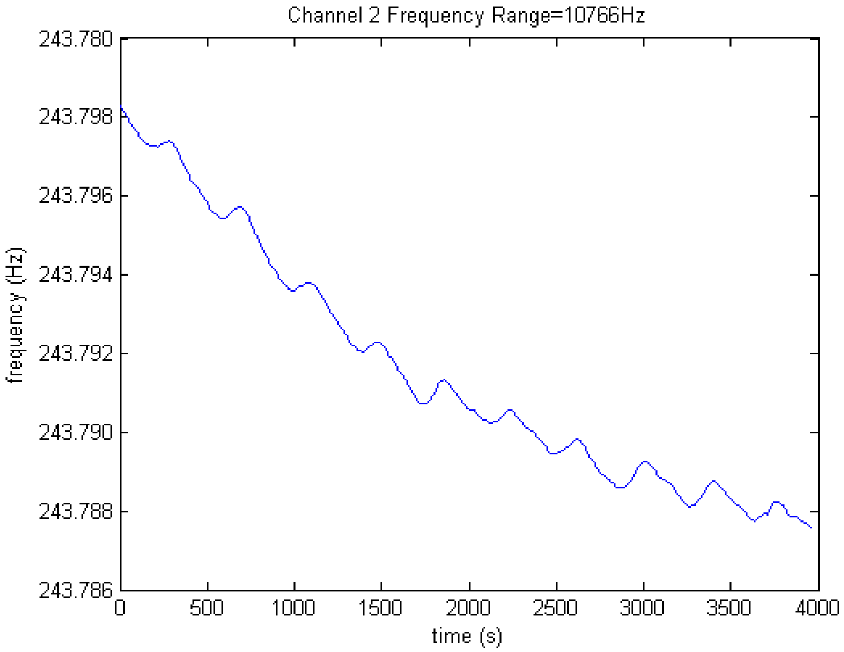

Fig. 5.24 The frequency estimation result for differential system channel 2 in experiment 3

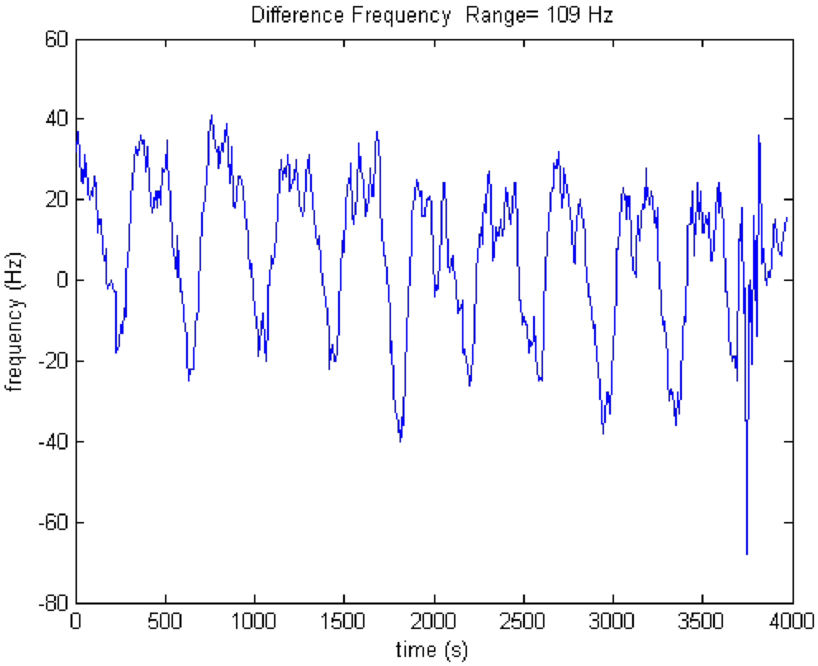

Fig.5.25 The frequency estimation result for differential system output in experiment 3

With the channel 2 shift step, the range of the differential output is reduced to around 30 Hz. Two independent experiments are performed and shown in Figs. 5.26-5.31.

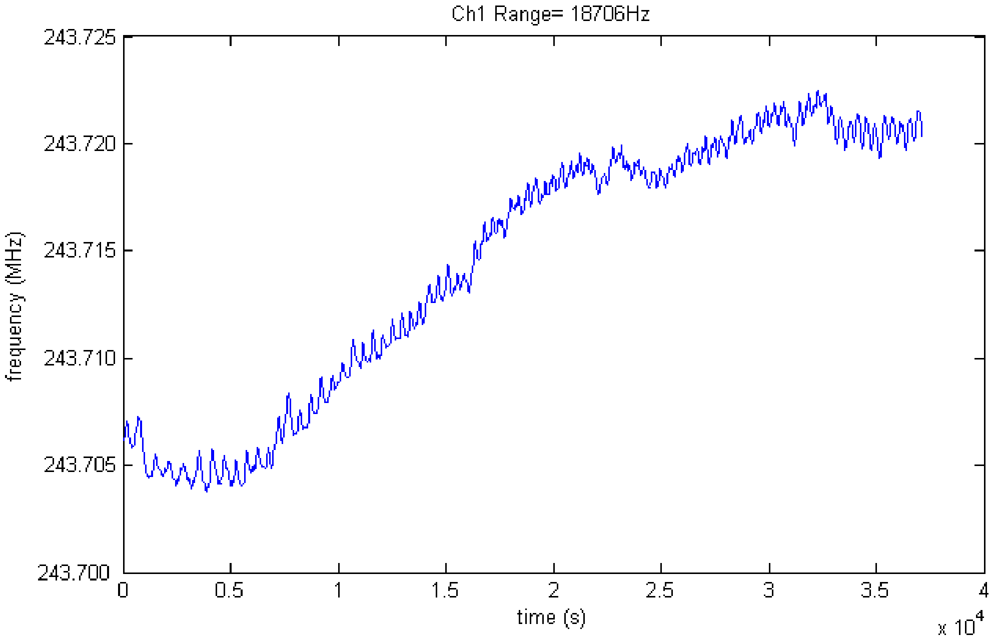

Fig. 5.26 The frequency estimation result for differential system channel 1 in experiment 4

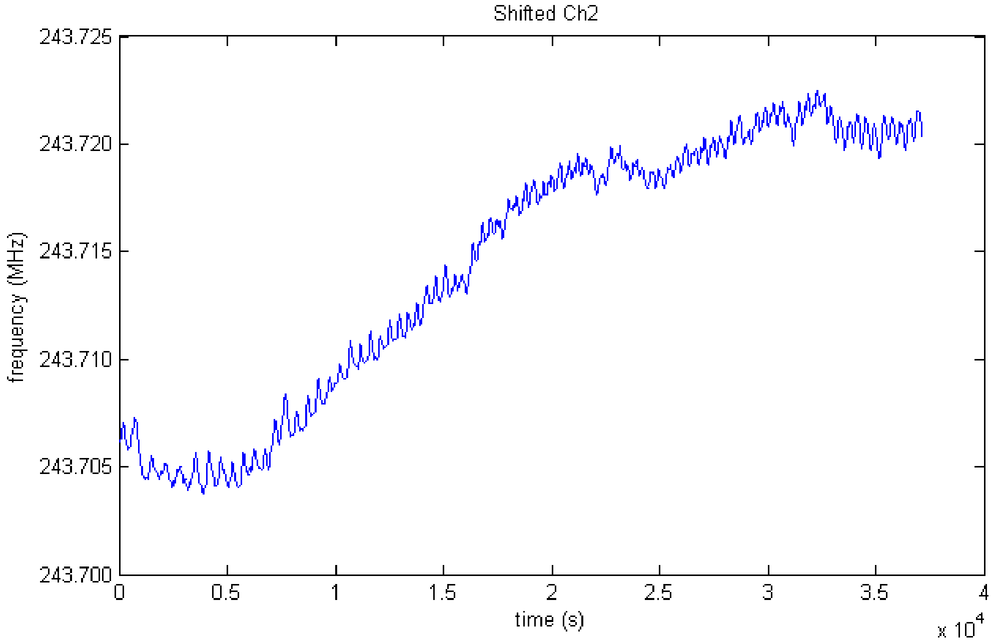

Fig. 5.27 The frequency estimation result for differential system channel 2 in experiment 4. The signal of channel 2 has been shifted backwards

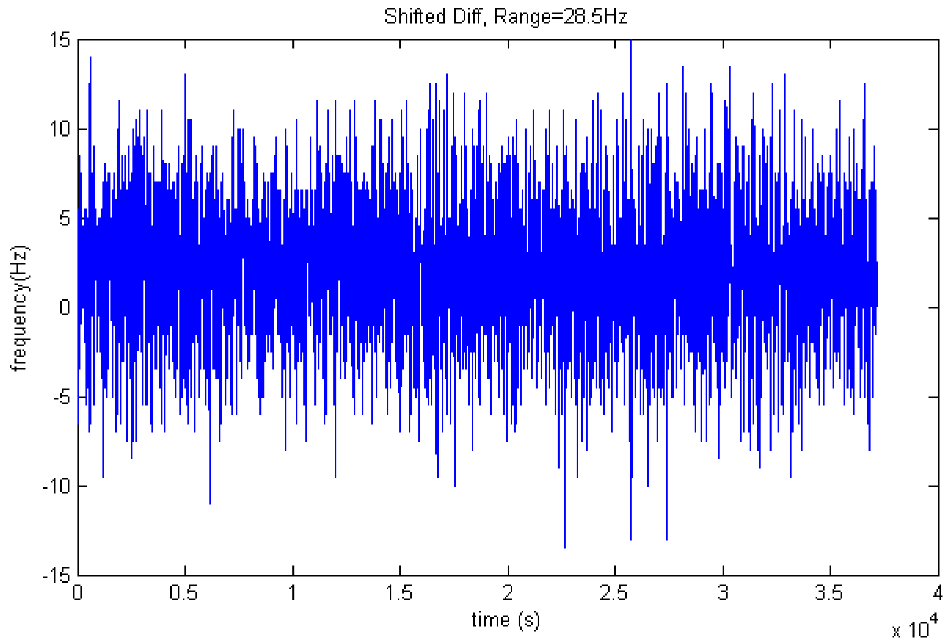

Fig. 5.28 The frequency estimation result for differential system output in experiment 4

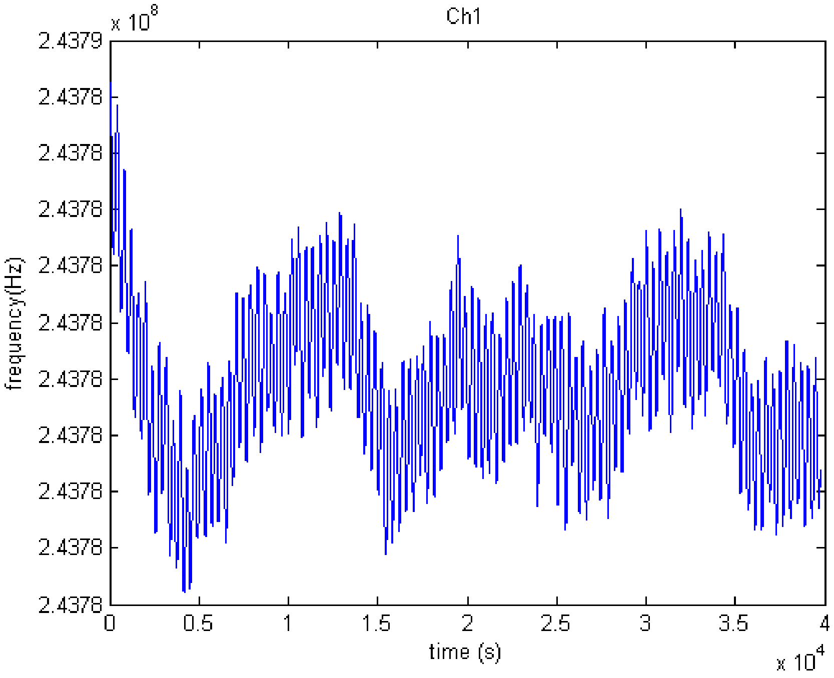

Fig. 5.29 The frequency estimation result for differential system channel 1 in experiment 5

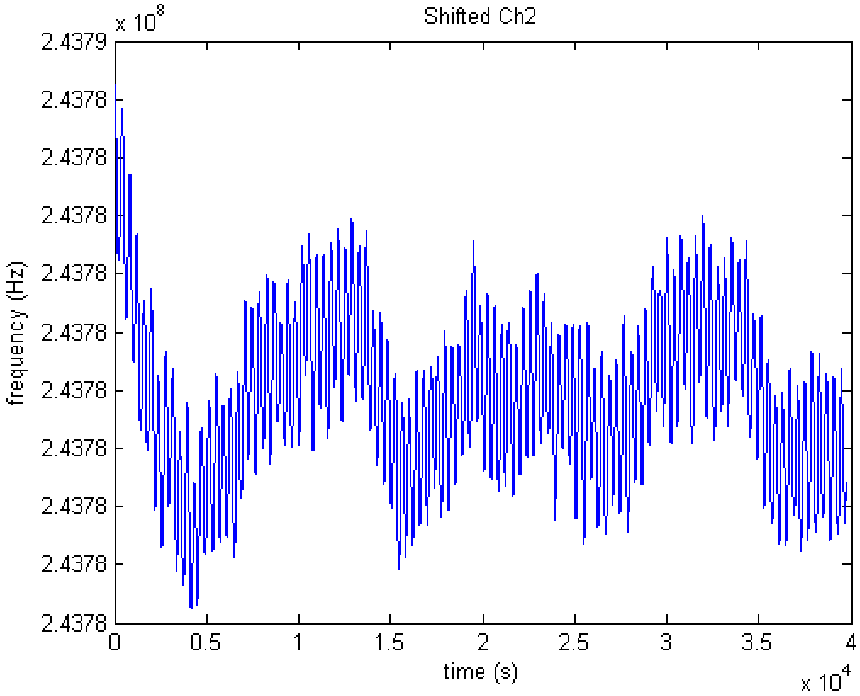

Fig. 5.30 The frequency estimation result for differential system channel 2 in experiment 5. The signal of channel 2 has been shifted backwards

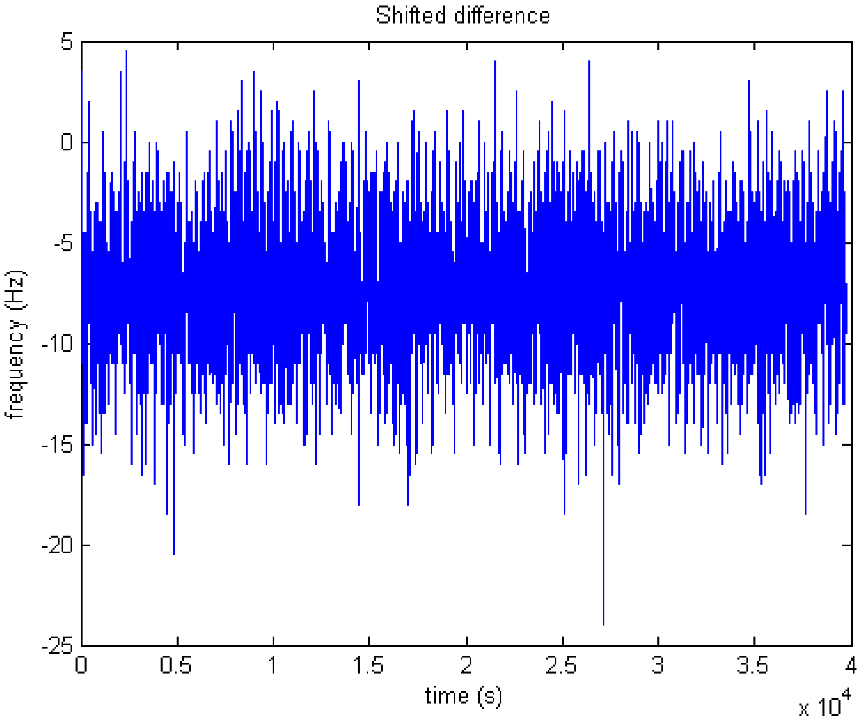

Fig. 5.31 The frequency estimation result for differential system output in experiment 5

To test the system performance in aqueous environment, we drop some water on the surface of the device. The system oscillation frequency becomes 254.51MHz which is SH-SAW Mode. The result shown in Fig. 5.32 indicates that the system successfully works in SH-SAW mode. Figs. 5.33 and 5.34 show the differential result before and after 50-points moving average in 8000 seconds. The measurement system shows great stability where the range is only 13.58 Hz.

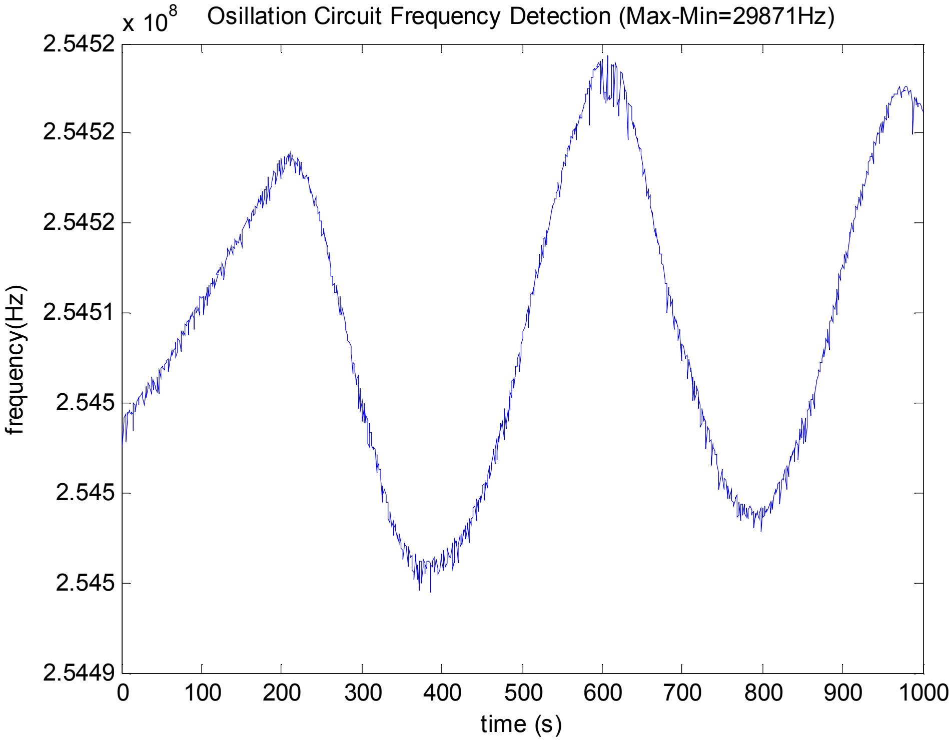

Fig. 5.32 Frequency experiment for the device working in SH mode

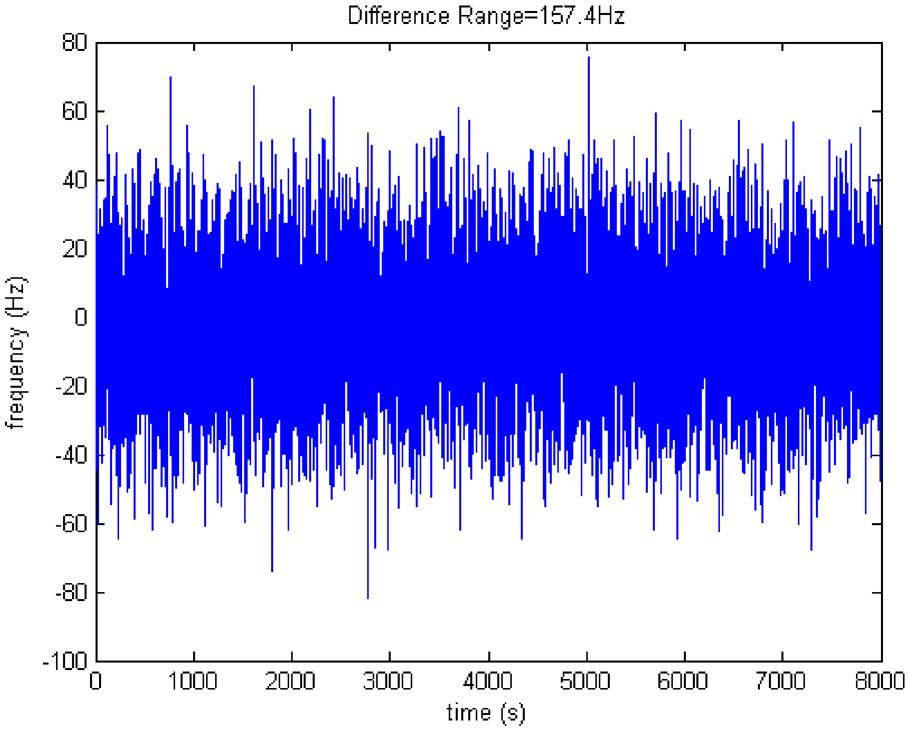

Fig. 5.33 The frequency estimation result for differential system output.

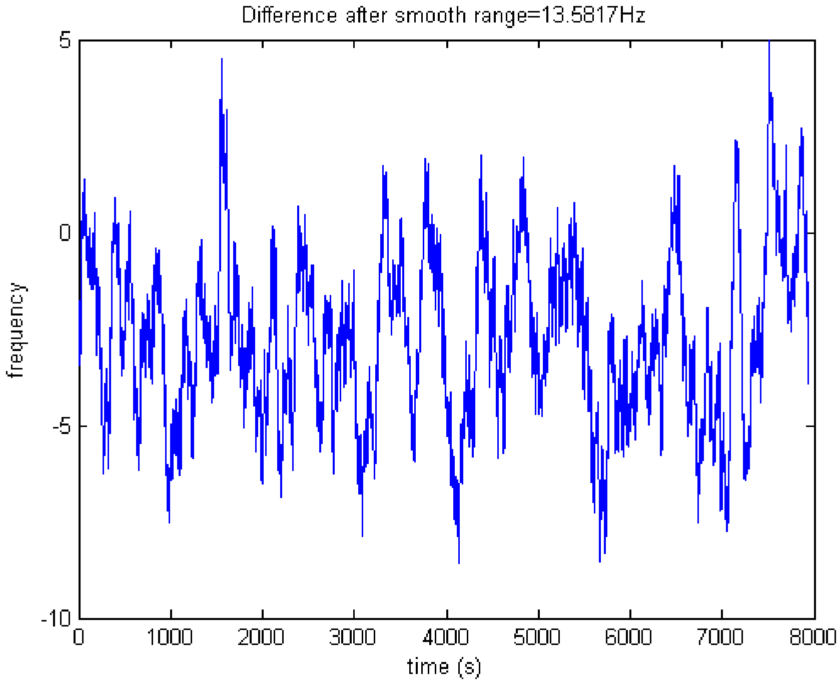

Fig. 5.34 The frequency estimation result for differential system output after moving average.

5.3 Temperature Compensation on the Frequency Measurement System

As we know, the frequency response of the AlN-based SAW device is temperature related [2, 190], and so is the proposed system. Although the differential configuration discussed above can help the system partially by canceling the effect of environment temperature change, it cannot remove the distinction of the two ‘so-called identical’ systems. Therefore, the temperature experiments based on our frequency detection system were conducted here to increase the system stability in large scale due to the environment temperature change.

A temperature control system is setup for the proposed frequency measurement system shown in Fig. 5.35. A heater connected to the power supply is placed under the device to control the temperature. By controlling the voltage of power supply, the temperature of the heater can be adjusted. Consequently, the temperature of devices can be controlled. The temperature will be read through a temperature sensor which is connected to a hand-held thermometer and recorded manually.

In the experiment, the temperature is changed from 24^{o}C (room temperature) to 32.0 ^{o}C. The frequency counter is employed to collect data where 6 measurements were taken for every 0.1 ^{o}C. The results are shown in Fig. 5.36. With the second frequency estimation algorithm, the differential output is calculated and shown in Fig. 5.37. The enlarged view is shown in Figs. 5.38 and 5.39, respectively. One can observe that the differential configuration works well in the interval from 24 ^{o}C to 26.5^{o}C, while requires compensation for higher temperature. Using Matlab data fitting toolbox, the temperature coefficients (from 27 ^{o}C - 32 ^{o}C) can be estimated as follows, the coefficient for the differential output is 2276 Hz/ ^{o}C, the coefficient for channel 1 is 18027 Hz/ ^{o}C, and the coefficient for channel 2 is 15750 Hz/ ^{o}C.

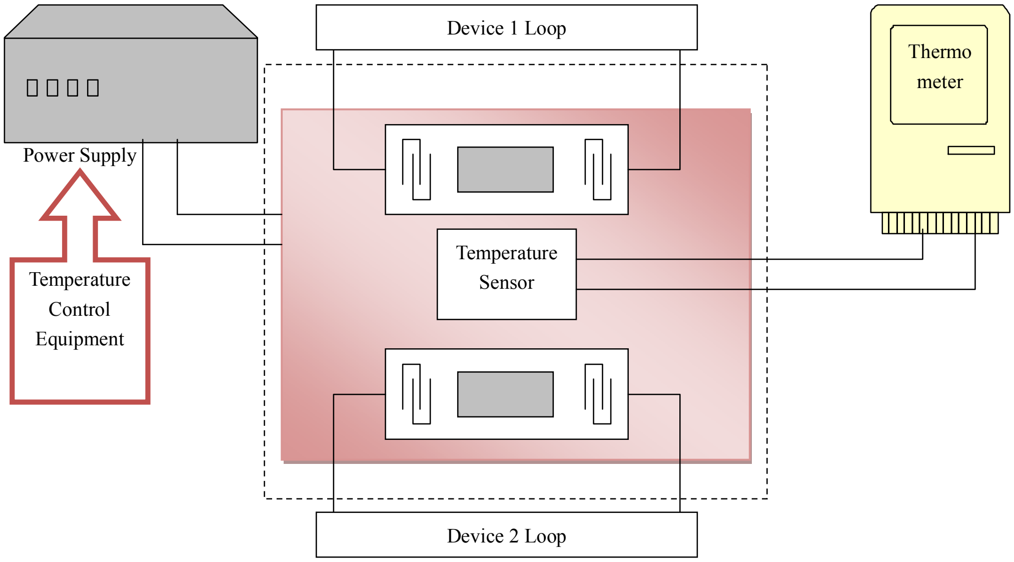

Fig. 5.35 The frequency measurement system and its temperature control system

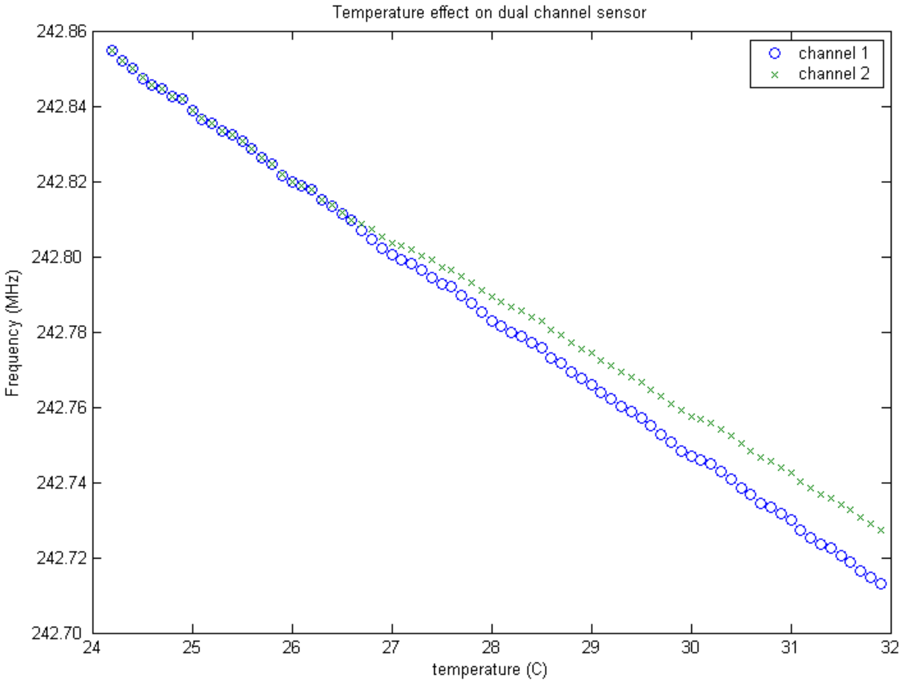

Fig. 5.36 The frequency measurements for two channels when the temperature is changed

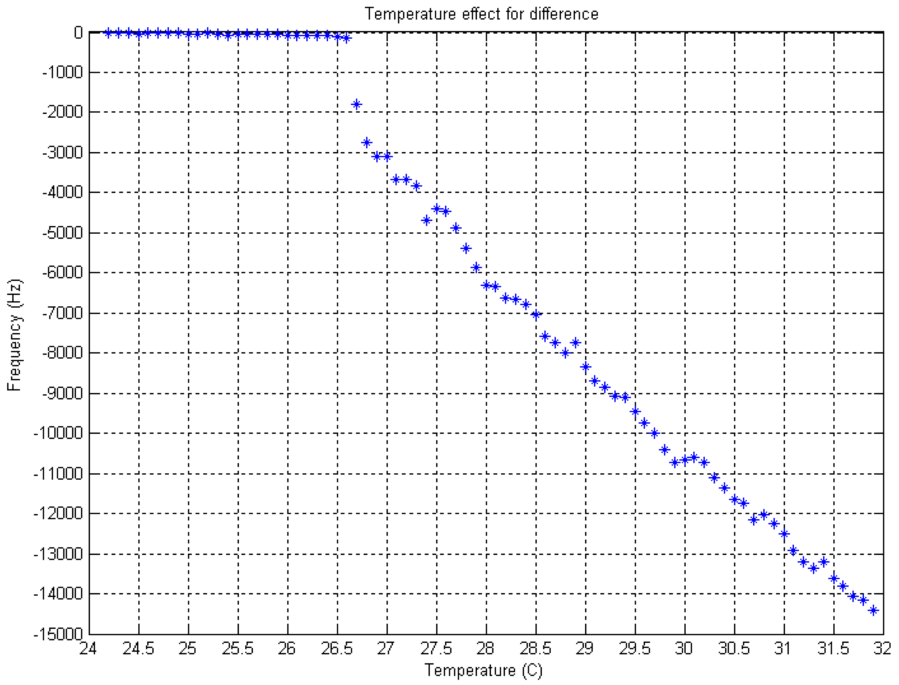

Fig. 5.37 The frequency estimation result on differential system output

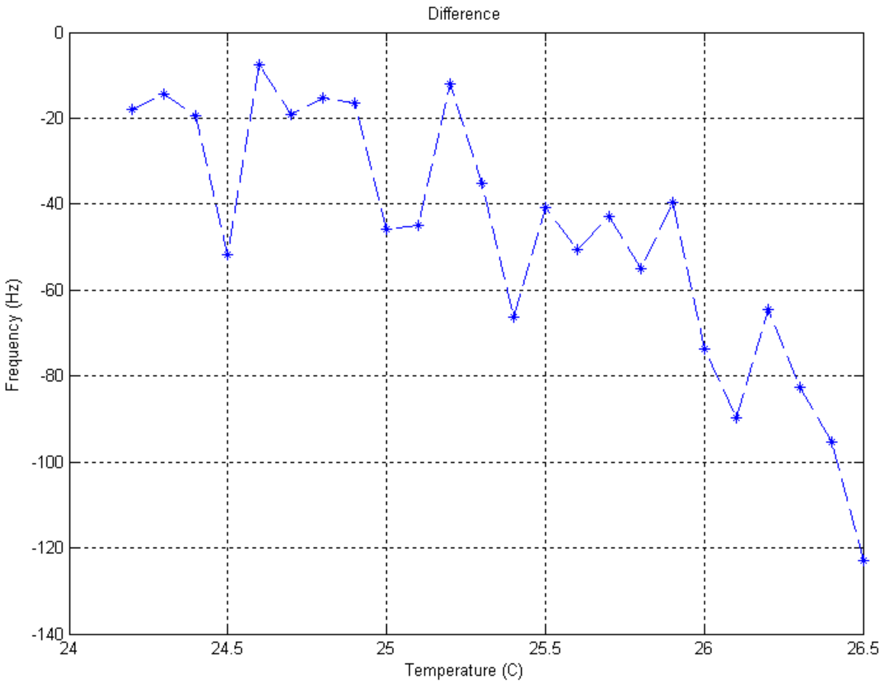

Fig. 5.38 The frequency estimation result on differential system output (enlarged view in 24℃-26℃)

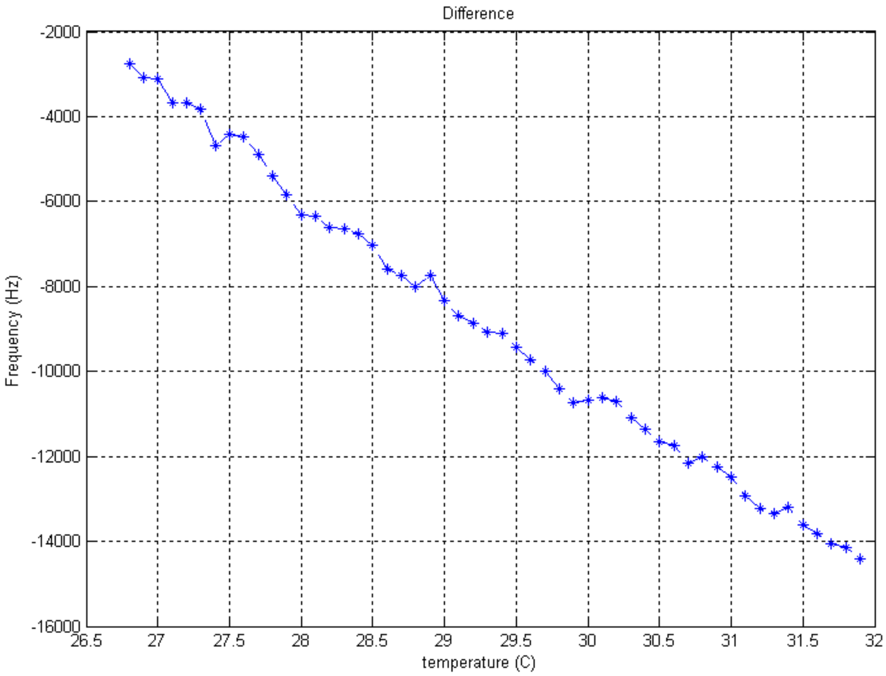

Fig. 5.39 The frequency estimation result on differential system output (enlarged view in 26.5℃-32℃)

Another experiment was conducted with different initial oscillation frequency. The results are shown in Figs. 5.40 and 5.41. Using Matlab data fitting toolbox, the temperature coefficients (from 26 °C - 40 °C) are obtained as follows, differential coefficient is 2722 Hz/ °C, channel 1 coefficient is 19710 Hz/ °C, and channel 2 coefficient is 16980 Hz/ °C. The Comparison between these two temperature experiments are shown in Figs. 5.42 and 5.43. The results indicate that different oscillation frequency results in different temperature coefficient which should be counted in the compensation algorithm.

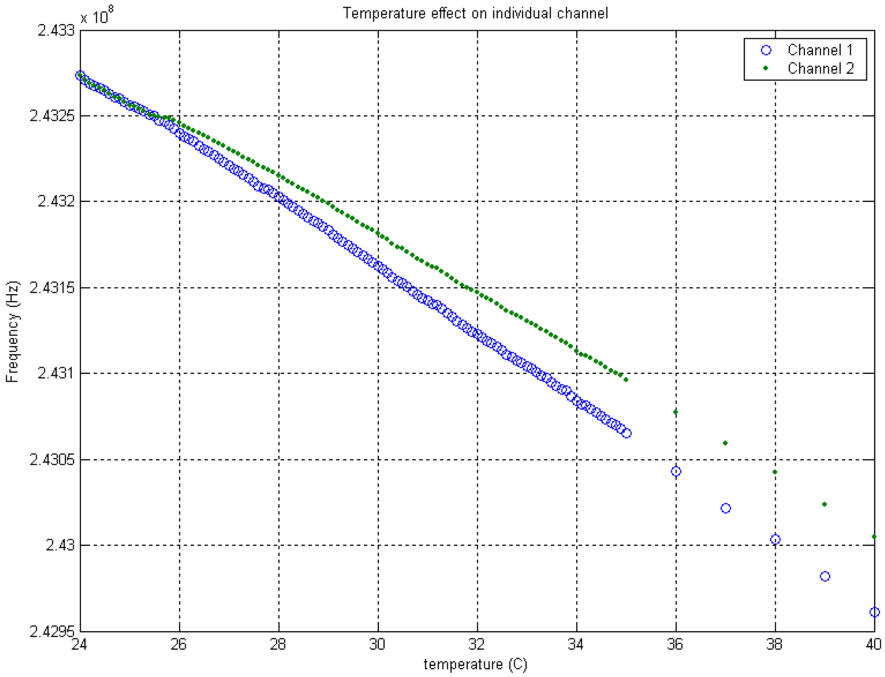

Fig. 5.40 The frequency measurements for two channels when the temperature is changed

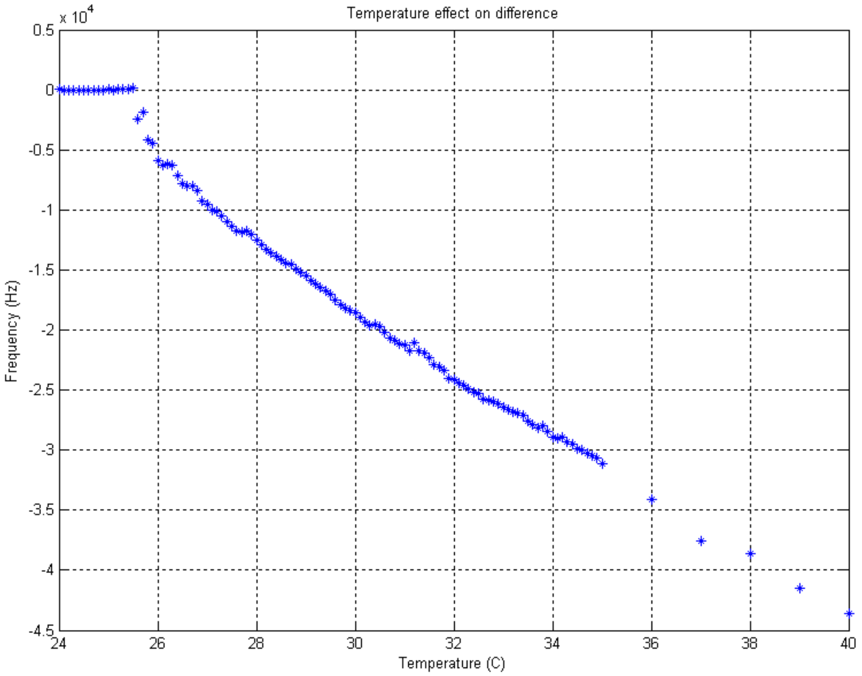

Fig. 5.41 The frequency estimation result on differential system output

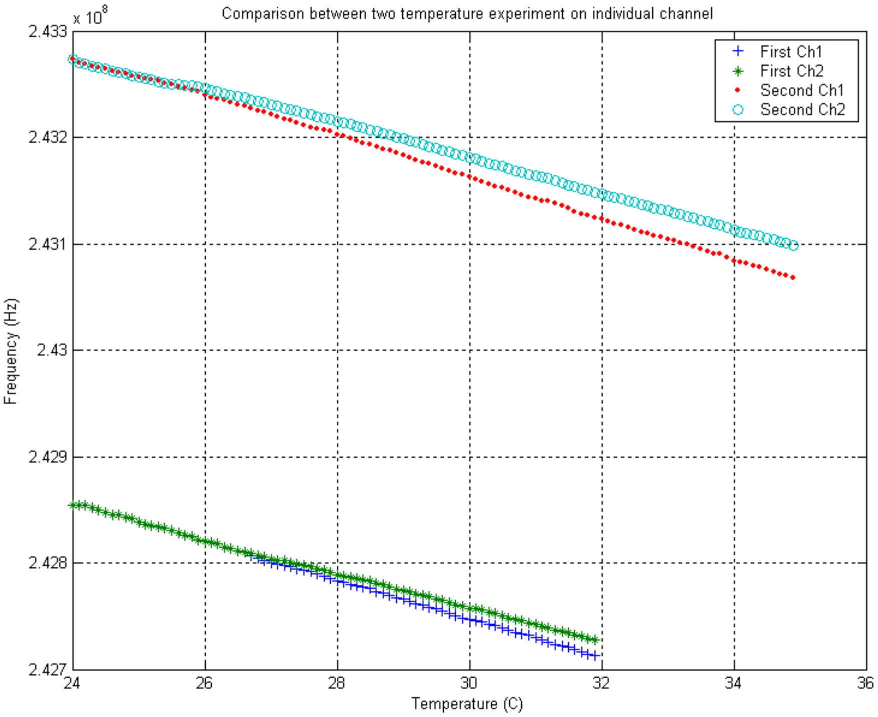

Fig. 5.42 The comparison between two temperature experiments on individual channels

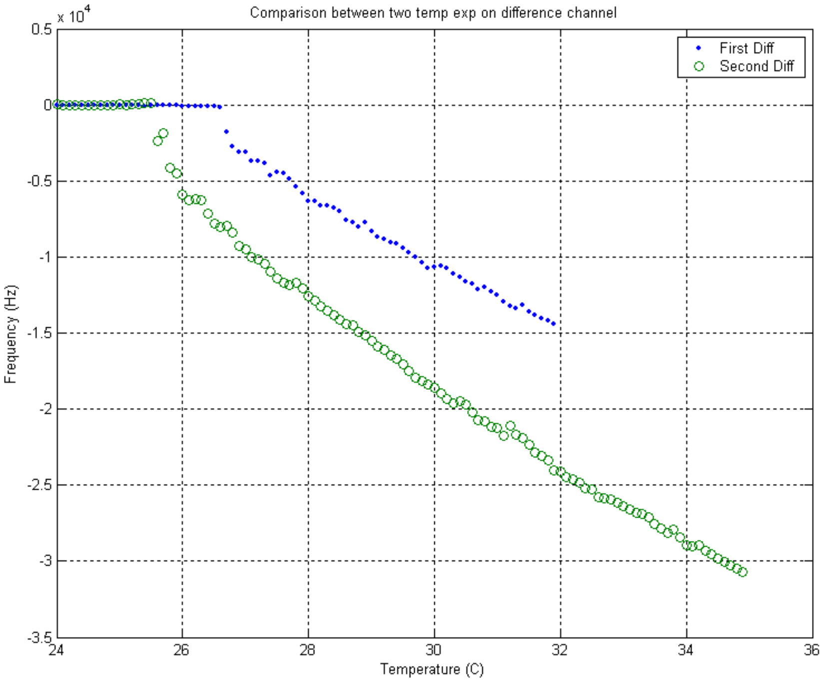

Fig. 5.43 The comparison between two temperature experiments on differential output

With the experiment data, the relationship between channel 1 and differential output can be fitted using piecewise linear function. Then the coefficients are interpolated using the data from different oscillation frequency. The final frequency estimation result will be subtracted by the temperature effects. By applying the compensation algorithm, the frequency estimation results are shown in Figs. 5.44 and 5.45 (Temperature experiment 1 data is in use). After compensation, the differential result will be much more stable than the original differential output which results in the resolution of the system increasing to 0.12 nN.

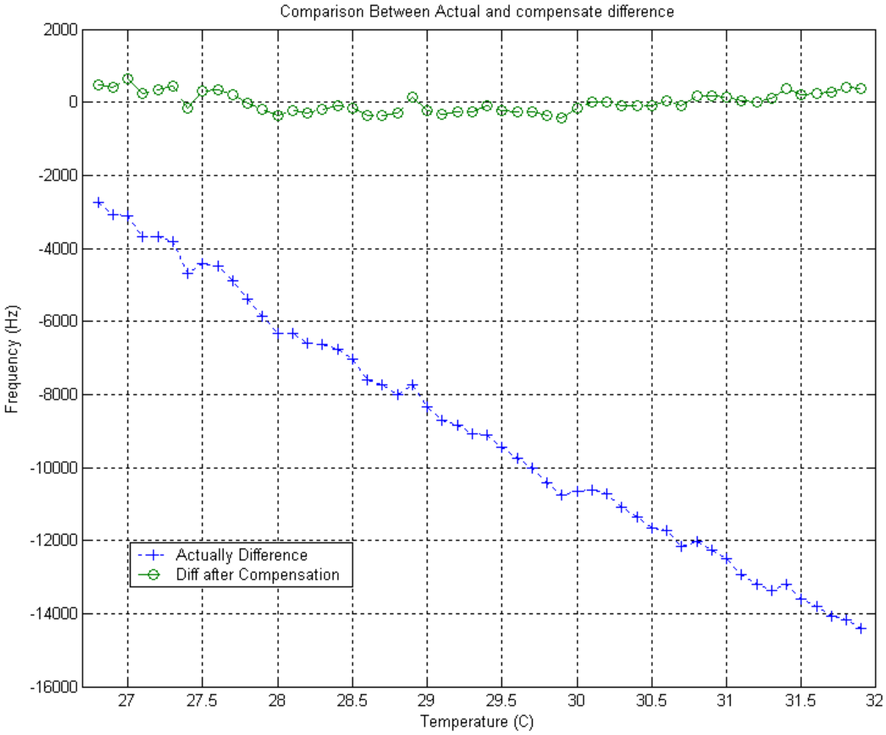

Fig. 5.44 Comparison on the differential output results before and after temperature effect compensation

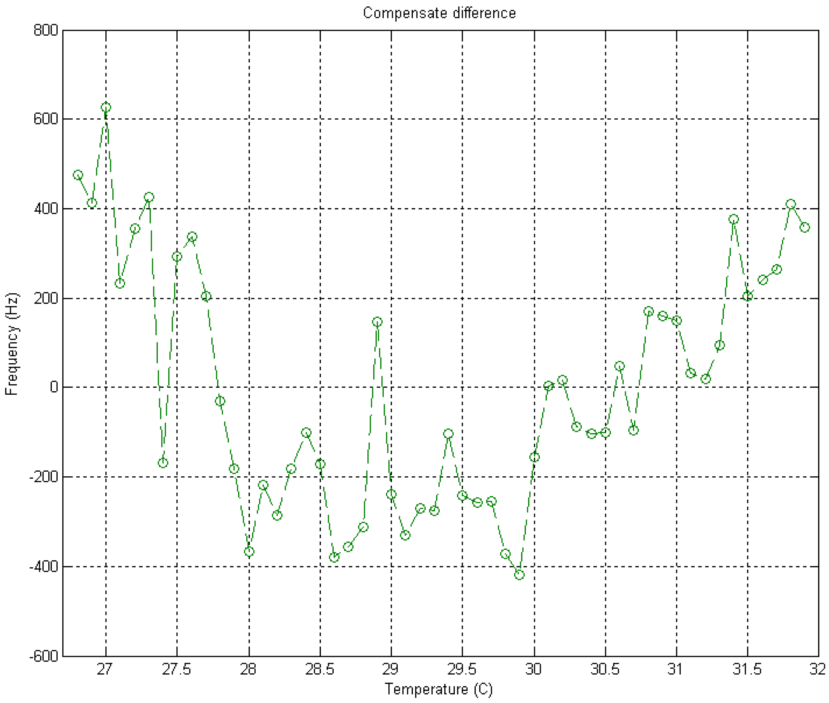

Fig. 5.45 The frequency estimation result on differential system output after temperature effect compensation

We also compare the proposed frequency measurement approach with the phase measurement approach [17]. The phase detection approach is applied and the results are shown in Fig. 5.46 and Fig. 5.47. Using Matlab data fitting toolbox, we can obtain the temperature coefficients as follows, the coefficient for differential channel is 1.21 degree/℃, the coefficient for channel 1 is 6.26 degree/℃, and the coefficient for channel 2 is 7.47 degree/℃. Comparing with frequency temperature coefficient, the ratio between the frequency and phase results for channel 1 is 2.712 (Hz/mD) and the ration between the frequency and phase results for channel 2 is 2.639 (Hz/mD).

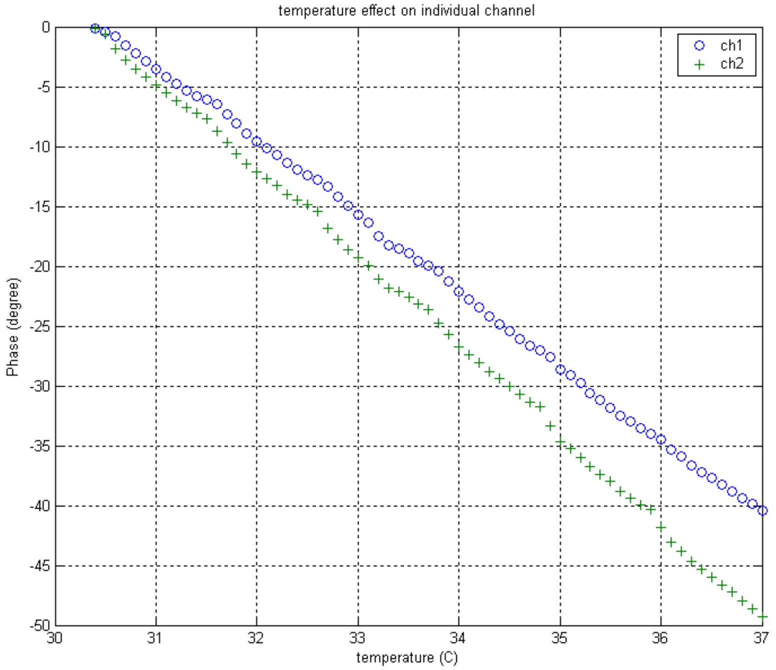

Fig. 5.46 The phase estimation results on individual channels

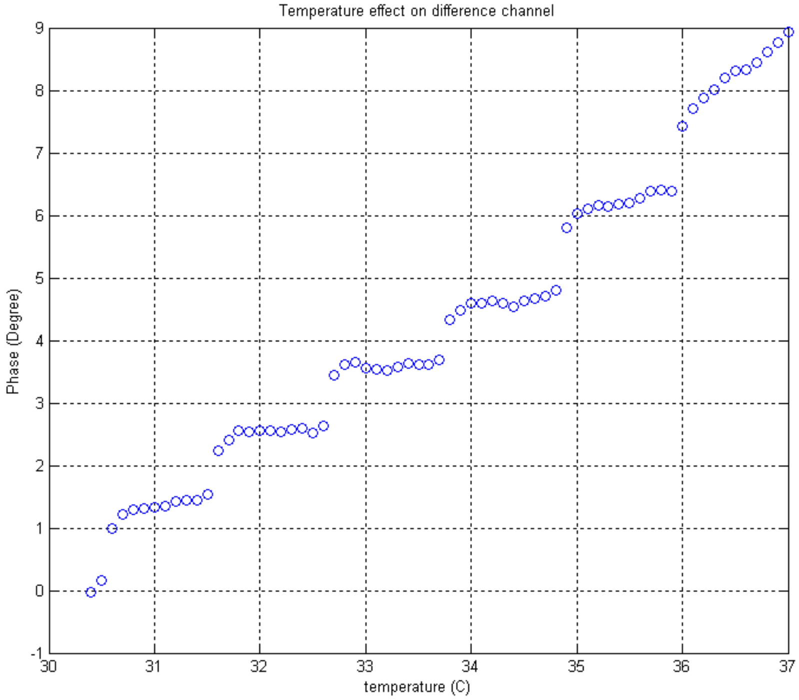

Fig. 5.47 The phase estimation results on differential system output

For the temperature experiment 2, the comparisons between the frequency method and phase method are shown in Figs. 5.48, 5.49 and 5.50. The ratio between the frequency and phase results for the differential output is 3.4 (Hz/mD). The comparison results are shown in Fig. 5.51.

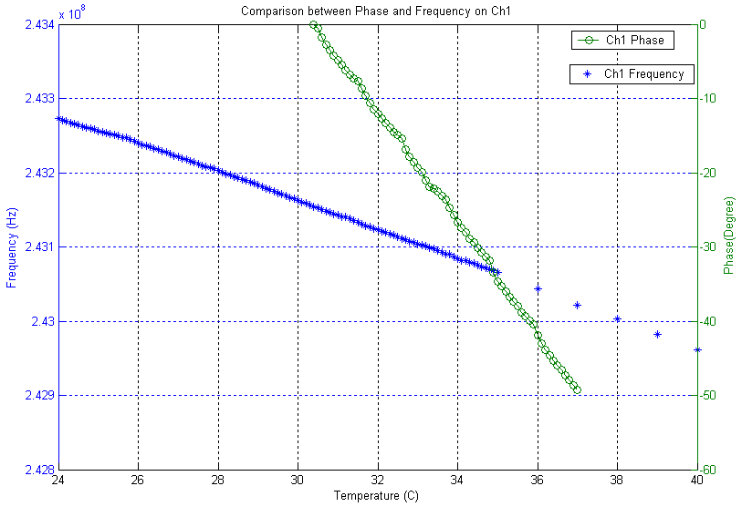

Fig. 5.48 The comparison between frequency and phase estimation methods on channel 1

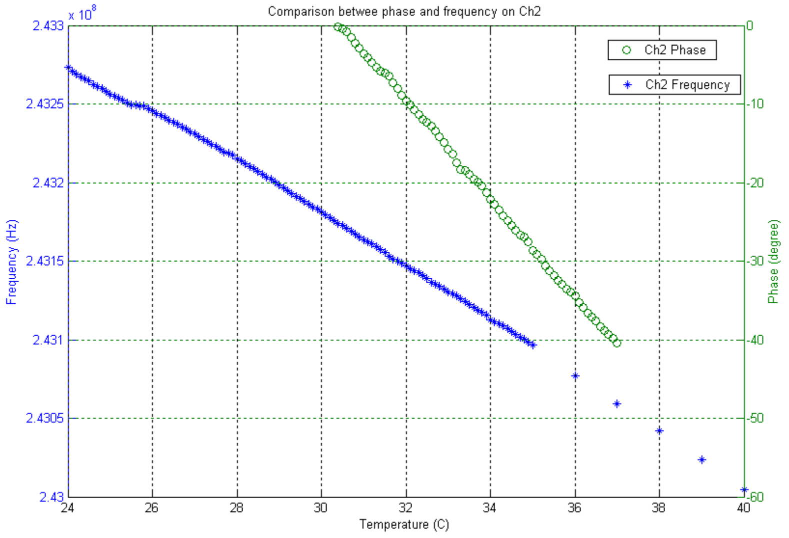

Fig. 5.49 The comparison between the frequency and phase estimation methods on channel 2

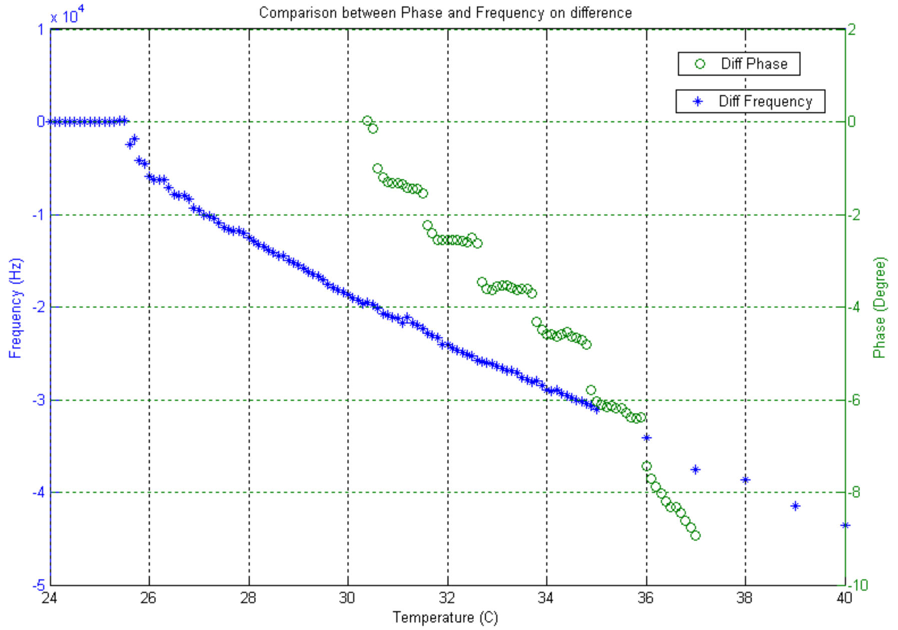

Fig. 5.50 The comparison between the frequency and phase estimation methods on the differential output

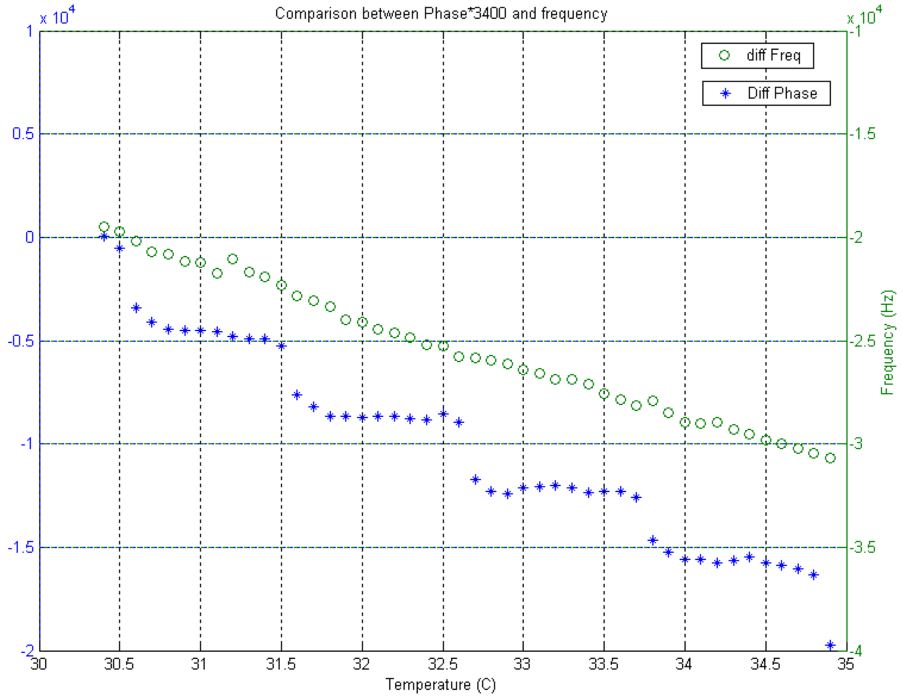

Fig. 5.51 The comparison between frequency and phase (multiplying the ratio coefficient 3400) on differential output

5.4 Portable Electrical Circuit Design

The prototype system consisting of separate components is difficult to be installed on the surgical robot. A practical solution is to integrate all separate components into one small printed circuit board (PCB) and attach it to the robot arm.

Similar to the prototype system, the system schematic of the whole differential system is shown in Fig. 5.52. A pair of differential devices is employed in two oscillation loops. The oscillation frequency is 242MHz for SAW mode and 255MHz for the SH/SAW mode. To prevent the system working in other frequency band, a low pass filter and a high pass filter are placed in each loop. The 1 db pass band for these two filters is from 225MHz to 265MHz. When the device is working in SAW mode, the loop insertion loss is about 30db+3 db (power splitter) + 2.2db (switches)+ 2 (filters)=37.2 db. When the device is working in SH-SAW mode, the loop insertion loss is about 50db+3db+ 2.2db+ 2=57.2db. Therefore, we need 2 amplifiers (each gain is 20db) for the SAW mode, one additional amplifier for the SH-SAW mode. Two switches are used to control the number of amplifiers. Two SMA terminators connected to the loop to export the output signal. A small circuit using mixer is employed to convert the frequency to voltage. The design diagram is shown in Fig. 5.53 or Fig. 5.54. The difference between design 1 and design 2 is the number of the output. So design 1 is easier to be realized but the design 2 is more flexible to process the results.

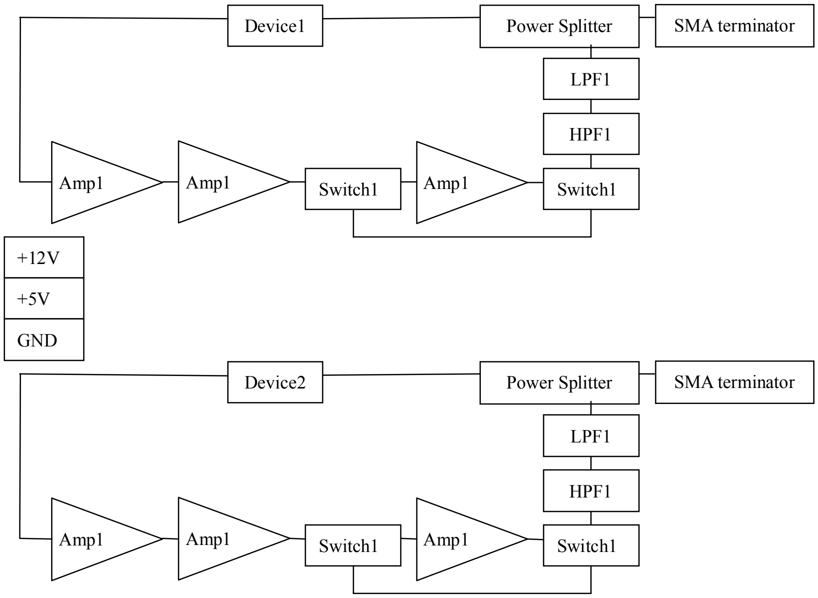

Fig. 5.52. The system diagram of the differential frequency measurement system using PCB

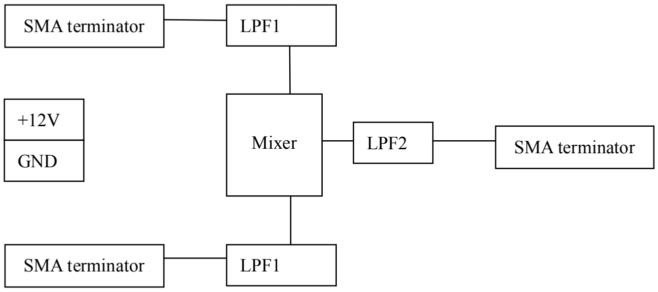

Fig. 5.53. The system diagram of frequency conversion design 1

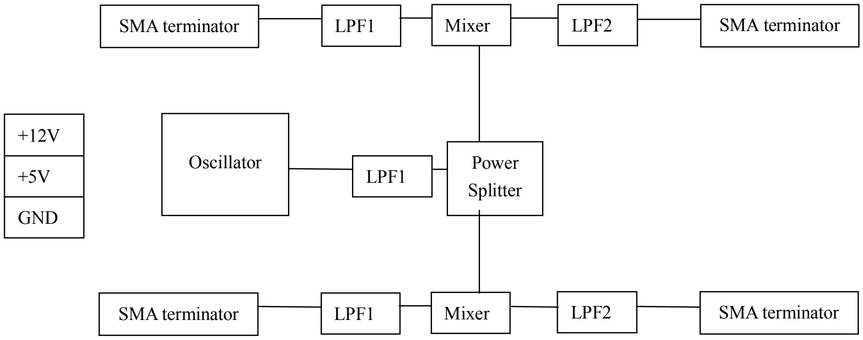

Fig. 5.54. The system diagram of frequency conversion design 2

The components selection is shown in Table 5.3. All components are bought from http://www.minicircuits.com and http://digikey.com. The PCB is fabricated by http://apcircuits.com.

Table 5.3 The components for the portable electric PCB

Amplifier	Ram6	6	MINICIRC
Amplifier(backup)	Ram8	2	MINICIRC
Power splitter	ADP-2-1	3	MINICIRC
Switch	RSW-2-25P	4	MINICIRC
LPF1	SALF-265	5	MINICIRC
LPF2	SCLF-5	3	MINICIRC
HPF1	PHP-250	2	MINICIRC
Transformer	ADT1.5-1	4	MINICIRC
Terminator	J502-ND	7	DIGIKEY
SMA adapter	J633-ND	2	DIGIKEY
C bypass	PCE3014CT-ND (0.1 uF)	4	DIGIKEY
C bypass	478-1230-1-ND(18000pF)	12	DIGIKEY
C block	478-1234-1-ND(39000pF)	8+4	DIGIKEY
Resistor	RHM100FCT-ND	4	DIGIKEY
Resistor	RHM536FCT-ND	8	DIGIKEY
Resistor	RHM121FCT-ND	2	DIGIKEY
Mixer	TBD	3	MINICIRC
PCB PROD	TBD	3	APCIRC

There are two versions of PCB designed in this work a test version and a compact version. The test version PCB is bigger than the compact version PCB and therefore suitable for test, measurement and evaluate in the lab environment while the compact version PCB is for robotic use.

The schematic plot of test version PCB Design is show in Fig. 5.55. The dimension of PCB is 3.0 inch X 3.0 inch. The PCB is designed with the software of Altium Designer ® 6. The PCB design file is shown in Fig. 5.56. The 3D effect figures are shown in Fig. 5.57 and Fig. 5.58. When it works in SAW mode, the signal spectrum is shown in Fig. 5.59 that indicates the oscillation circuit is working properly.

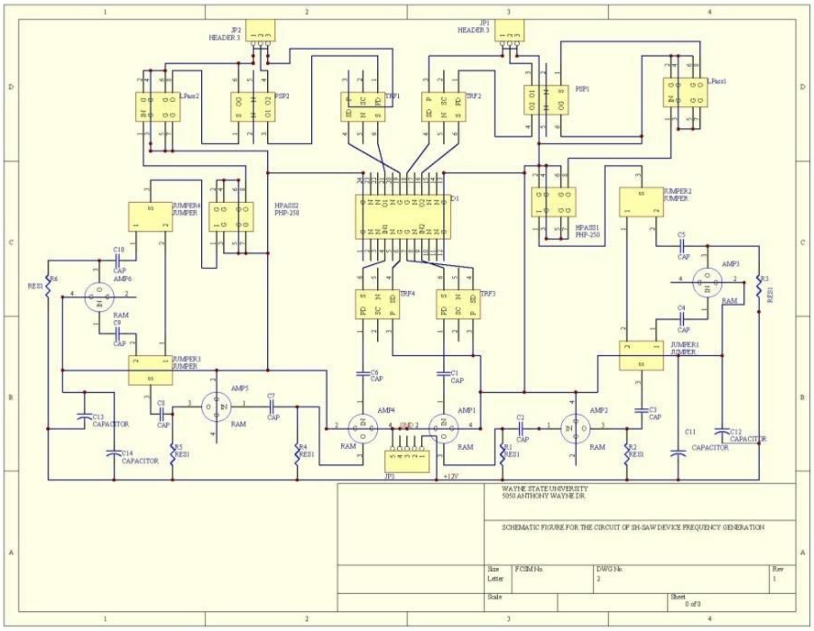

Fig. 5.55 The schematic plot for the test version PCB design

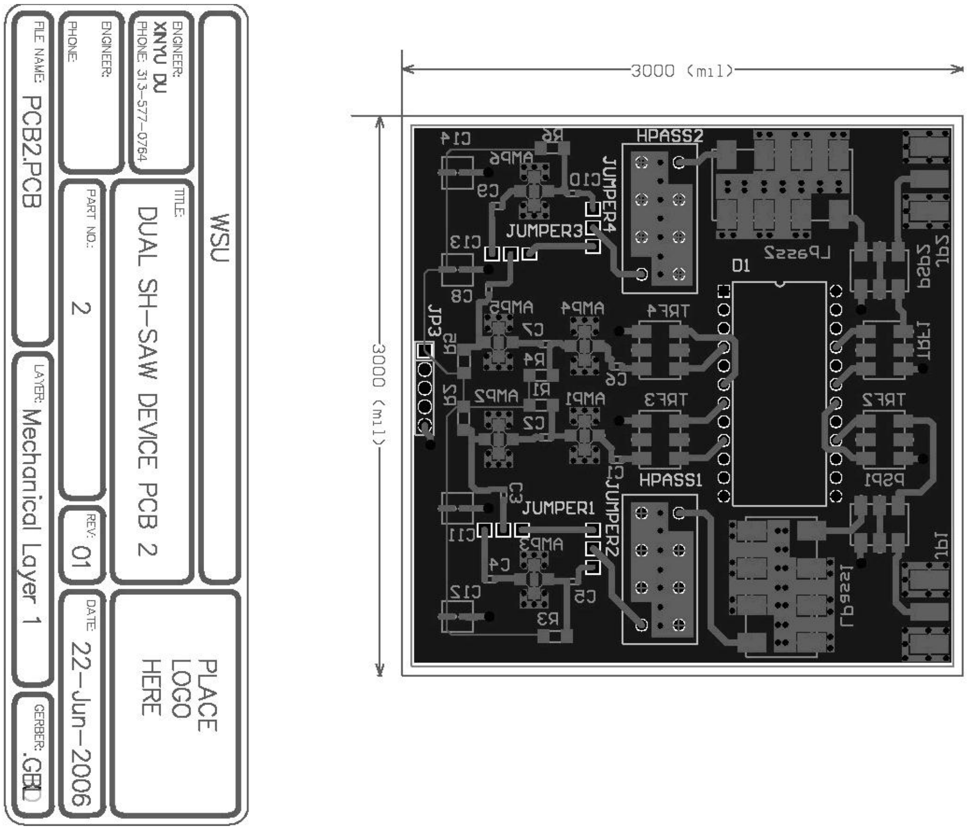

Fig. 5.56 The PCB design file for test version PCB

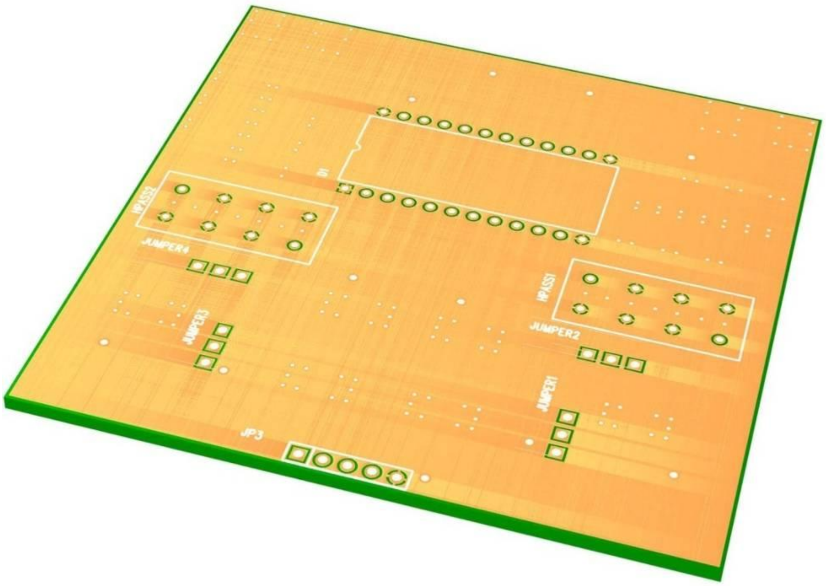

Fig. 5.57 The top view of 3D effect for the test version PCB

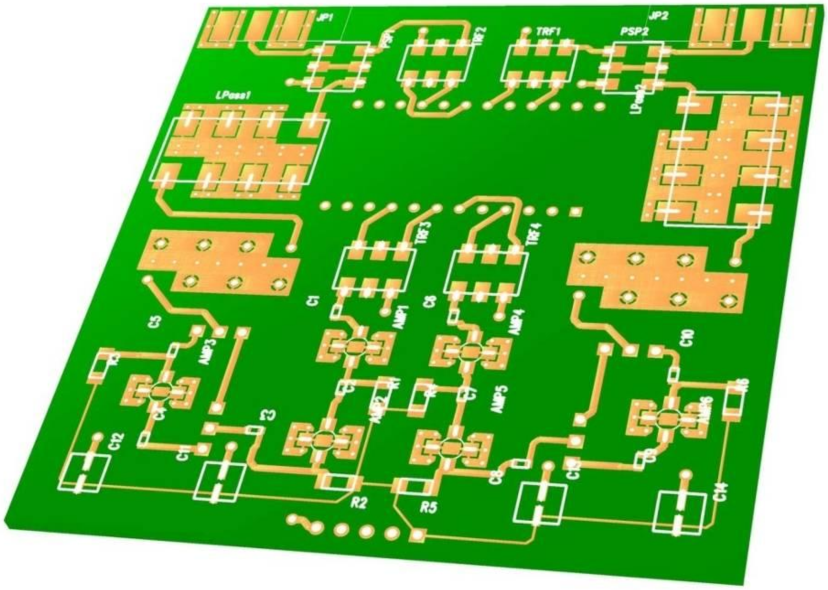

Fig. 5.58 The rear view of 3D effect for the test version PCB

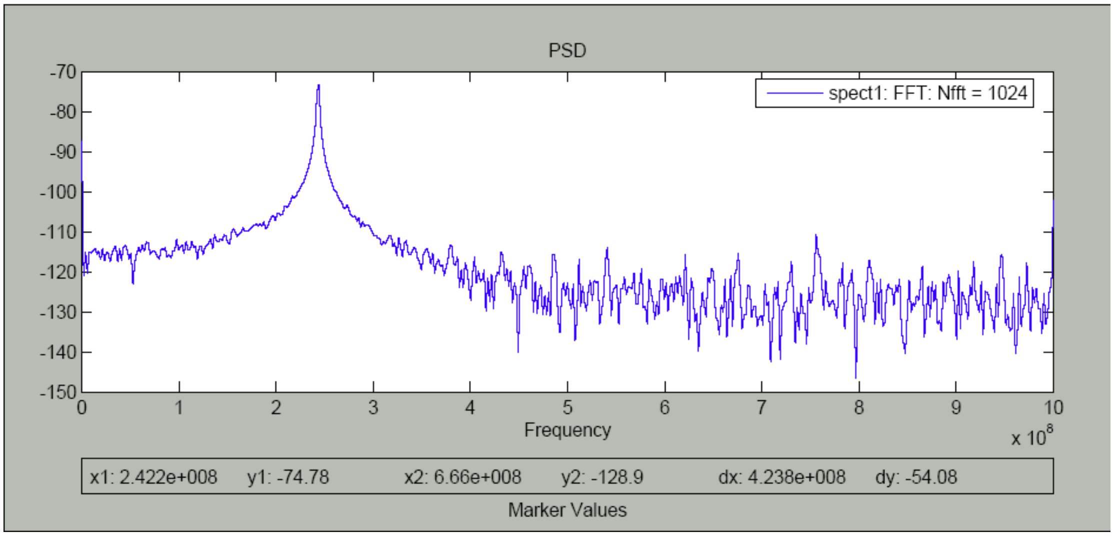

Fig. 5.59 The signal spectrum measured from the test version PCB

The compact version PCB is redesigned based on the test version PCB. All electric components are placed and aligned to reduce the size. The area of the compact version PCB is 58% of the size of the test one. We remove the all switches to reduce size and prevent more electromagnetic radiation. Thus the working mode will be selected automatically: when there is no water on the surface of device, the insertion loss of SAW mode is less than the second mode for our device. So the system works in SAW mode. On the other hand, the insertion loss of the second mode is less than SAW mode. Subsequently, the system works in the SH-SAW mode. The RF shield cover is added to meet EMC requirements. Furthermore, more through holes are added into the design to increase the electromagnetic property of the system. The resulted schematic figure and PCB design files are shown in the Fig. 5.60 and Fig. 5.61, respectively. After elaborative testing most devices are working properly.

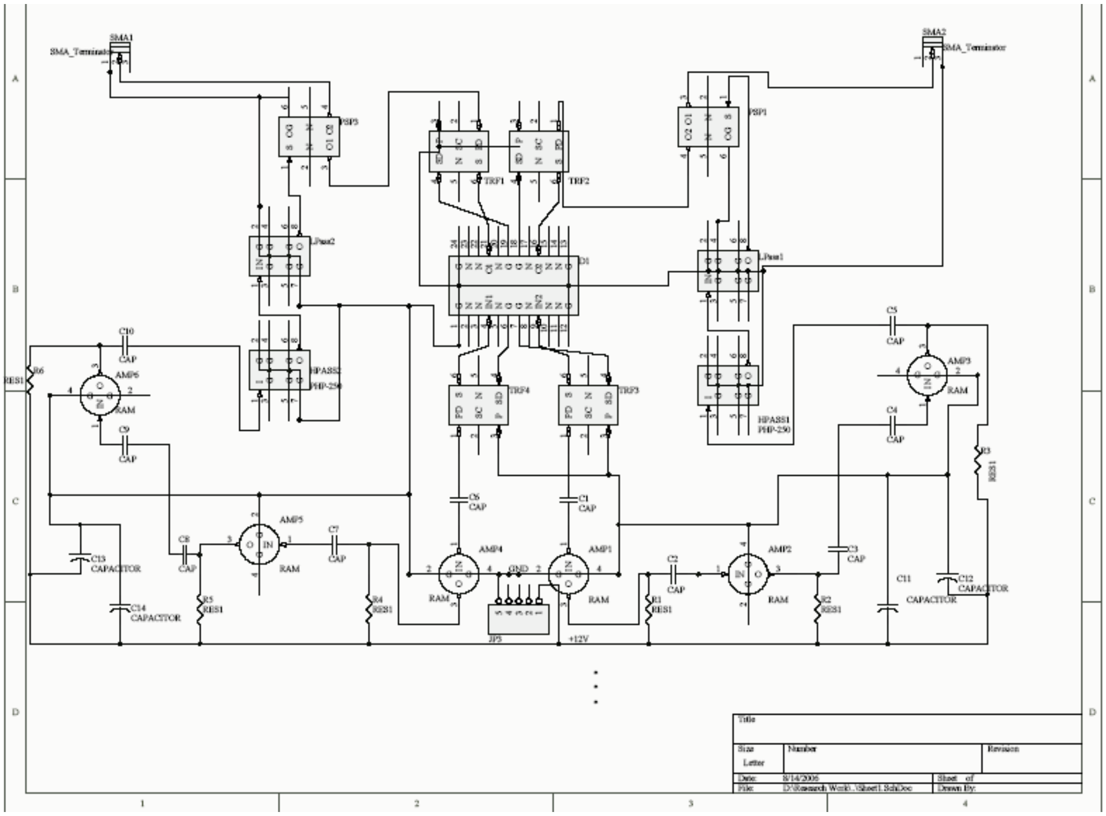

Fig. 5.60 The schematic plot for the compact version PCB design

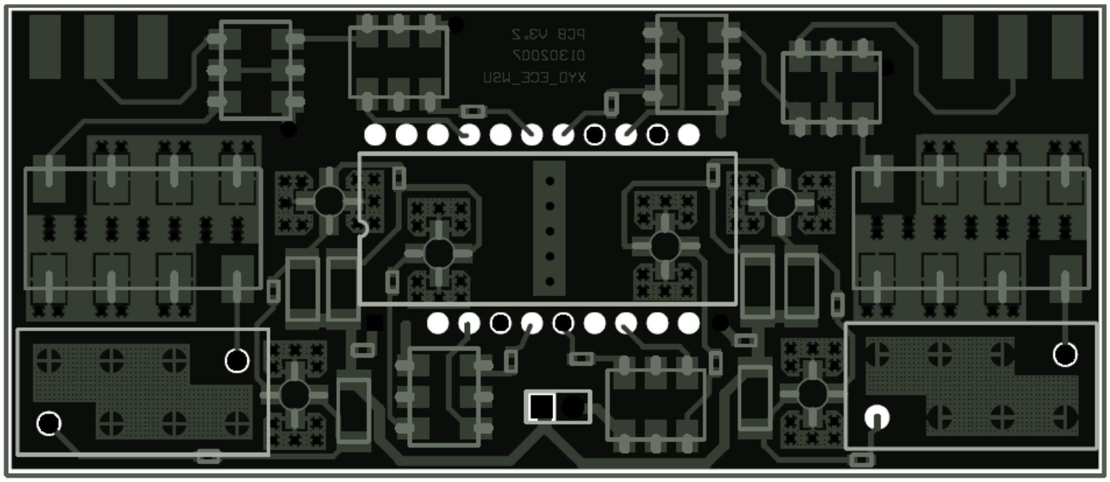

Fig. 5.61. PCB design file for compact version PCB

An auxiliary PCB was also designed to test our PCB (shown in Fig. 5.62). There are 3 parts of the auxiliary PCB, One is to test the device performance, another is to test the mixer performance and the center part is to test the electrical switch. The test PCB works properly. The experiment proved the mixer can produce a low frequency sin wave signal with the difference frequency of two inputs when its inputs are the signal from the signal generator and the signal from one output port of test or compact version PCB.

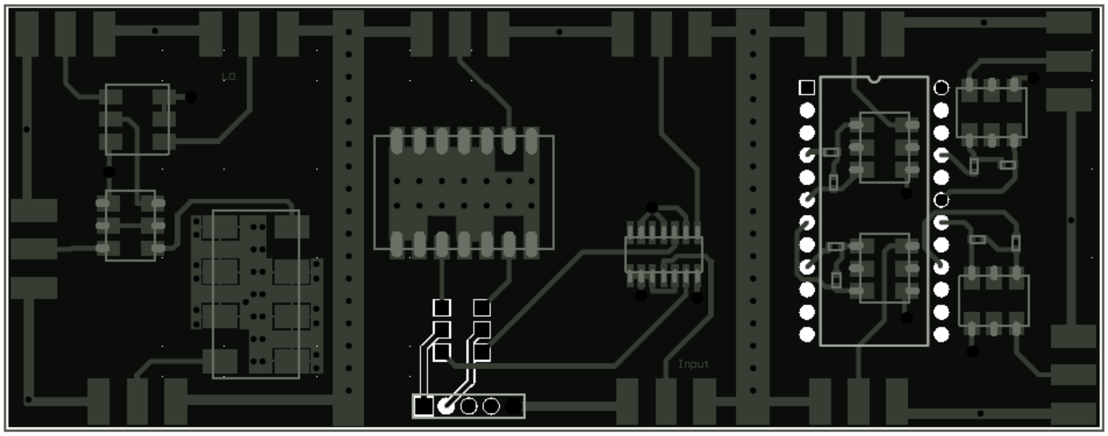

Fig. 5.62. The auxiliary PCB design file

CHAPTER 6 CONCLUSIONS AND FUTURE WORK

6.1 Summary of the Technical Contributions

A novel prototype pressure sensor based on AlN SAW/ SH-SAW device is proposed in this work. The core component AlN-based SAW/SH-SAW device is designed, fabricated, analyzed and evaluated. The data acquisition (DAQ) system including prototype and portable peripheral circuits and signal processing algorithms are explored afterwards..

The SAW device used in the proposed pressure sensor employs AlN as the piezoelectric material and the insulator. With a delay-line IDT structure design, the SAW mode and SH-SAW mode are expected to be excited. Comparing to the previous design in bacterial sensing application, the new scheme inherits the basic features of dual model AlN devices but also greatly improves its applicability in aqueous environment for surgical robotic applications.

In order to validate the new design, both theoretical and computational analyses are performed. In the aspect of theoretical analysis, the delta function model and structural mechanics models are employed. The qualitative results point out the impaction of design parameters and validate the device design. Since the geometry of the device is too complex to make the analytical derivation, the FEM analysis is implemented using COMSOL Multiphysics ® in this work. Due to the computer hardware limitation the FEM analysis is performed using two types of approximations. First the 2D plane strain approximation is in use with the real device dimensions. The device with insulator and without insulator is modeled, meshed and simulated. The simulation results from frequency domain analysis on insertion loss show good agreement the experimental measurement in terms of the shape and center frequency. These results reveal the existence of the SAW mode and prove the correctness of the design. Another trial is the 3D simplified model approximation. Different mode and wave propagation can be observed from the simulation results. It is also found that the different reduced dimensions affect the simulation results greatly as well as the material constants. The FEM analysis performed in this work lays a solid foundation for providing an opportunity in the future to reduce the design time and fabrication cost in the conventional design and fabrication processes for micro electro mechanical systems.

The proposed design scheme of the AlN-based device is fulfilled in the SSIM clean room. The crystalline epitaxial AlN thin film is successfully grown on the surface of A-plane Al_2O_3 as well as on the top being an insulator using our PSMBE system. The crystal structure is monitored during the deposition by RHEED and checked with XRD after deposition. The aluminum IDT is evaporated using lift-off photolithography techniques. In order to cover the IDT with a layer of AlN, several masks and holders are designed and fabricated to facilitate the insulator deposition. The frequency response from the network analyzer shows the effectiveness of the new design. Comparing to the previous trials on different photoresist and SiO_2 the AlN insulator has the advantages on low attenuation (-5 to 3 db vs. 10 db in SiO_2) and superb stability (1.5 µm crystal vs. 500nm in SiO_2, or 780 nm in photo resist).

We also investigate the DAQ system. A prototype DAQ system is setup using separate components. The differential system shows great system detection stability.

An enhanced zero crossing method based on oscilloscope and time-shift method based on the frequency counter are employed, respectively, to detected the frequency shift due to external load change. Based on the prototype system, the environment temperature impaction is measured and identified. The compensation algorithm is developed to improve the system robustness. With the proposed measurement system and the temperature compensation algorithm the system sensitivity is 8.16 kHz/nN and the resolution in a temperature-variant environment becomes 0.12 nN. To the end, the portable peripheral circuit is designed based on the prototype system.

6.2 Future Work on the AlN-Based Pressure Sensor

The pressure sensor proposed in this work has small dimension, excellent durability, high sensitivity and applicability working in aqueous environment. Although some substantial progresses have been made, it is still worth putting in more efforts in the future.

The insertion loss of the device is still relatively low comparing to the device based on other piezoelectric materials such as $LiNbO_3$, Quartz, etc. One possible change is to employ the resonator IDT structure instead of the delay line structure. Multiple-device array is also a potential scheme to increase the insertion loss. These kinds of optimization can be implemented using FEM simulation platform. With more powerful computers or work stations, a 3D model with the real size is able to accurately predict the device performance when design parameters are changed. By applying the statistical method Taguchi method [191], the most impact factors from numerous geometric or physic parameters can be revealed. The Taguchi method is developed by

Genichi Taguchi and broadly applied to experiment design in the field of engineering, biotechnology and marketing field [192-193]. The first step of Taguchi method is to define the process objective, i.e. maximize the insertion loss in this application. The second step is to determine the design parameters, that the number of design freedom. Then create the orthogonal arrays for all design parameters to indicate the number and conditions for experiment. When the trial experiments are conducted, the performance data will be collected and used to complete orthogonal arrays. At last the data is analyzed to predict the optimal performance and the parameter influence.

Even though the parameters are analyzed, it's still not easy to tune these most important parameters to achieve the best design solution manually since the scope of the parameter is large. An automatic way is to employ the commercial software Isight® [194] which is the product of Dassault Systèmes to seek the optimal solution. With the help of Isight® add-on components, the parameters to be tuned can be automatically feed into Comsol Multiphysics®. The result from Comsol Multiphysics® then flows into Matlab® to calculate the performance index e.g. the insertion loss. By pre-defining the objective value, Isight® can search the parameters in the predefined scope until the optimal and robust one is finally found.

To better serve the surgery's needs, the pressure information at certain measured locations should be converted to the area textile information, e.g. normal tissue, tumor etc. Such conversions can be made by fuzzy expert systems [195] or machine learning algorithms [196-197]. As a robotic probe, the 3D textile reconstruction for the sensing space is desired. How to effectively select the measurement location is an interesting topic. A new emerging algorithm, compressed sensing [198-199] is a possible solution. Through preliminary exploring the signal sparsity, the measurement points can be dramatically reduced. The complete signal will be reconstructed after transmitting to the computer. Compressed sensing is already successfully applied to the similar scene the robotic controls [200].

APPENDIX 1. ALN DEPOSITION EXPERIMENT STEPS

1. Loading Procedure. The substrate will be loaded to the main chamber in this step.

    (1) Clean the substrate properly.

    (2) Unscrew the load-lock door. Open N2 valve at the load lock. When the pressure in the load-lock reaches 760 Torr, the load-lock door will open. Close N2 valve and place sample holder inside. Make sure the holder is facing towards down.

    (3) Close the load-lock door. Turn on the roughing pump, open the roughing valve and turn on the turbo pump at once.

    (4) Close the ion pump valve.

    (5) After the pressure in the load-lock goes off scale, turn off the turbo pump and close the roughing valve.

    (6) Open the valve between the load-lock chamber and main chamber.

    (7) Using the load-lock fork, place the substrate & holder into the main chamber.

    (8) Retract loading fork and close the valve between the load-lock chamber and main chamber.

    (9) Open the cryo-pump valve.

    (10)Turn on the ion pressure gauge G1 or G2.

    (11)Turn off turbo pump, close the roughing valve. After 20 minutes, turn off the roughing pump.

(12)Turn on the RGA valve and the separate pumping system for RGA.

(13)When the pressure in the Main chamber reaches vacuum more than 10^{-7} Torr. Turn on RGA and perform degassing process.

(14)When the pressure in the chamber is 10^{-8} Torr or less then open the ion pump valve.

2. Chamber Baking and Substrate degassing. The water in the chamber and inside the substrate will be removed in this step.

(1) Turn on the affinity water cooling unit. Open the cooling water output valves and input valves for all sources and heater.

(2) Close all shutters.

(3) If desired, turn on the substrate rotation. Switch on motor power toggle. Start the QuickStart software in computer. Select EXITS, DUMB TERMINAL. Enter, Send commands, Exit. Open Commands, Select Constant Velocity, rotation=20 steps/sec. OK.

(4) Switch on the thermocouple unit and pyrometer.

(5) Raise substrate and lower heater to within 3 mm of each other.

(6) Press Power ON for HP6675A DC power supply. Set current and voltage value (start from 15A/20V) to for desired temperature level. For substrate degassing, 90V (798^{o}C) is selected. Note that the relation between voltage and temperature is not constant but depending on the environment.

(7) Turn on the power switch for RGA.

(8) Start RGA software, Select Utilities, RS232 Setup, Com5, connect. Select Head, Channel, Electron Multiplier, Gain=1078, Reference Mass=28, Voltage=1351, ON, OK. Select Scan, Mass Spec Parameters, Mass scan range=1-60, Scan rate=3, Scaling factor =1, Points per AMU=10. Select Utilities, Analyze, GO.

(9) Open the valve between turbo pump and electron gun. Start the turbo pump and let it run at higher 70000 rpm to get the desired vacuum. Open the main shutter and closed the observation shutter.

(10)When pressure gauge reading < 15, close the turbo pump valve and immediately open the gate valve between the main chamber and the electron gun.

(11)Turn on the RHEED power supply and increase the voltage slowly up to 30 kV. Increase the current slowly to 1.4A.

(12)Be sure the substrate is raised to maximum height (to the stopper).

(13)Open the RHEED screen.

(14)Start the KSA program in the computer.

(15)Turn ON electron beam on the hand held control panel.

(16)Adjust sample height, x, y axis position and get the RHEED pattern.

3. Pre-sputtering. The source will be cleaned by plasma. No deposition happens by closing all shutters.

(1) All shutters should be closed.

(2) Turn ON the RFX power supplies for the desired sources.

(3) Close ion pump valve, RGA valve and turn off the ion pressure gauge. Close the cryo-pump gate valve by 50%.

(4) Turn on the main N_2 and Ar line, and turn on the desired sources. Turn on only Ar lines to the mass-flow controller (set at 40 sccm).

(5) Adjust the cryo-pump gate valve so that the left hand side baratron gauge reading is 0.05 torr.

(6) Set the initial power as 100 W for all RF controllers. Press START. Check if Reflect=0.

(7) With plasma at all sources, open the cryo-pump valve to get 1.2-1.3 mTorr of pressure on the right hand side baratron gauge.

(8) Closed the observation shutter and wait for 15 minutes to one hour for sputtering.

4. Buffer Layer Deposition and Annealing. The buffer layer will help to increase the AlN quality by reducing the lattice mismatch [201].

(1) Adjust the substrate heater temperature as desired (45V, 400^{o}C).

(2) Starting the deposition. Set the substrate holder bias to 12 V (VSET=12, ISET=1).

(3) Open the observation shutter.

(4) Switch ON for the main N_2 gas toggle. Switch ON for two N_2 flow controller switches.

(5) Open the shutters for sources and main shutter.

(6) Adjust the cryo-pump gate valve to obtain 1.2-1.3 mTorr of pressure. The buffer layer deposition lasts about 15mins

(7) Close all shutters. Switch off for the main N_2 gas toggle and two follow controller switches. Switch OFF for the main Ar gas toggle and flow controller switches

(8) Stop RF controllers for all sources

(9) Open cryo-pump gate valve fully.

(10) Increase the substrate heater voltage to 77V. When temperature reaches 695^{o}C, begin to time annealing. Annealing is no more than 10 minutes.

5. Film deposition

(1) Close ion pump gate valve, RGA valve. Turn OFF IG1 pressure gauge. Set ON for substrate bias. Adjust the substrate temperature at 643^{o}C, 70V.

(2) Switch ON for the main Ar gas toggle and all sources toggle. Switch ON for the Ar flow controller.

(3) Adjust the cryo-pump gate valve to set the pressure 0.05 torr for left hand side baratron gauge.

(4) Start RF power supplies. Set power 200W.

(5) With plasma on all sources, open the cryo-pump gate valve to get the pressure of 1.2-1.3 mTorr at right hand side baratron gauge.

(6) Switch ON for the main N_2 gas toggle and N_2 flow controllers.

(7) Open the main shutter and all shutters for sources.

(8) Close the observation shutter. The deposition is started.

6. End of Deposition.

(1) Close all shutters and turn off bias and RF power supplies.

(2) Switch OFF for the N_2 main gas toggle and flow controllers.

(3) Stop RF power supplies.

(4) Switch OFF for the main Ar gas toggle and flow controllers. Switch OFF for the toggles for all sources.

(5) Open cryo-pump and ion pump valves, and wait until temperature drops to 50°C. Turn off heater controllers and coolant water.

(6) Stop holder rotation.

(7) Shutdown the pyrometer temperature unit and thermocouple temperature unit.

(8) Turn on roughing pump. Open the load-lock to roughing pump valve. Start the turbo pump when pressure in load-lock chamber <75 Torr.

(9) When the load-lock pressure is less than 10^{-4} Torr, stop the turbo pump. Close roughing pump valve. Open the load-lock chamber to the main chamber gate valve.

(10)Push the substrate carrier into the chamber and lift the substrate out of the holder.

(11)Retract the substrate carrier arm.

(12)Close the load-lock chamber to the main chamber gate valve.

(13)Make sure that the turbo pump has been off more than 20 minutes. Loosen the two load-lock access door screws and N_2 gas valve to the load-lock chamber.

(14)Remove the substrate holder with substrate for the load-lock chamber.

APPENDIX 2 THE PROCEDURES FOR AL IDT DEPOSITION

1. Clean the substrate by acetone and IPA manually and DI water by VERTEQ super clean 1600. Clean the mask and spin head by acetone.

2. Dehydrate the substrate on hotplate for 10 minutes at 150°C.

3. Center the substrate on the chuck of photoresist spinner 2 and check vacuum. Dispense 3 ml LOR3A on the substrate and start spinning at once at 400 rpm for 5 seconds and then at 4500 rpm for 45 seconds.

4. Bake the substrate on the hotplate for 5 minutes at 180°C.

5. Center the substrate on the chuck of photoresist spinner 2 and check vacuum. Dispense 3 ml Shipley 1811 on the substrate and start spinning at once at 600 rpm for 5 seconds and then at 4000 rpm for 40 seconds.

6. Bake the substrate on the hotplate for 90 seconds at 115°C.

7. Install the photomask and load the substrate into MA6 mask aligner. Make sure the dark side of photomask towards the substrate. Align the photomask, substrate and baseline substrate (if necessary). Set the program to SOFT and time parameter to 8 seconds.

8. Develop the substrate by immersing in CD 26 for 45-50 seconds.

9. Rinse and dry the substrate for 2 minutes with DI water then cleaned in the VERTEQ super clean 1600.

10. Check with the microscope. If the lines and undercuts are clear, continue.

11. Bake the wafer on hotplate for 5 minutes at 90^{o}C.

12. Deposit Al with 1500 nm thickness using E-beam evaporation. The tooling factor is set 40% and the active process and material is set to aluminum.

13. Remove the residual photoresist with Shipley 1165 remover for 3 hours at 55^{o}C. Then immerse the substrate into ultrasonic bath with DI water for 5 minutes.

REFERENCES

[1] D. S. J. Ballantine*, et al.*, *Acoustic wave sensors: theory, design, and physico-chemical applications*. San Diego: Academic Press, 1997.

[2] G. Hu, *Acoustic wave sensing system based on AlN dual-mode sensors and digitalphase detection approach*. Detroit: Wayne State University Ph. D. Thesis, 2008.

[3] K. Ahmed*, et al.*, "Current status of robotic assisted pelvic surgery and future developments," *International Journal of Surgery,* vol. 7, pp. 431-440, 2009.

[4] S. Bann*, et al.*, "Robotis in surgery," *Journal of the American College of Surgeons,* vol. 196, pp. 784-795, 2003.

[5] B. Davies, "A review of robotics in surgery," *Proceedings of the Institution of Mechanical Engineerings, Part H: Journal of Engieering in Medicine,* vol. 214, pp. 129-140, 2000.

[6] L. R. Kavoussi*, et al.*, "Comparison of robotic versus human laparoscopic camera control," *Journal of Urology,* vol. 154, pp. 2134-2136, 1995.

[7] G. H. Ballantyne, "Telerobotic gastrointestinal surgery: phase 2-safety and efficacy," *Surgical Endoscopy,* vol. 21, pp. 1054-1062, 2007.

[8] A. Carpentier*, et al.*, "Computer-assisted cardiac surgery," *Lancet,* vol. 353, pp. 379-380, 1999.

[9] MAXIM, "Demystifying piezoresistive pressure sensors," *MAXIM Applicaiton Note 871,* 2001.

[10] M. Yamada*, et al.*, "A switched-capacitor interface for capacitive pressure sensors," *IEEE Transactions on Instrumentation and Measurement,* vol. 41, pp. 81-86, 1992.

[11] B. M. Dutoit*, et al.*, "Flat electromagnetic pressure sensor for harsh environments," *Sensors and Acutators A,* vol. 91, pp. 51-56, 2001.

[12] A. Talbi*, et al.*, "A study of surface acoustic wave pressure sensor in ZnO/Quartz structure," in *IEEE International Conference on Sensors*, Vienna, Austria, 2004, pp. 550-553.

[13] M. Jungwirth*, et al.*, "Micromechanical precision pressure sensor incorporating SAW delay lines," *Acta Mechanica,* vol. 158, pp. 227-252, 2002.

[14] W. Wang*, et al.*, "optimal design on SAW sensor for wireless pressure measurement based on reflective delay line," *Sensors and Actuators A,* vol. 139, pp. 2-6, 2006.

[15] D. W. Branch and S. M. Brozik, "Low-level detection of a bacillus anthracis simulant using love-wave biosensors on 36 degrees YX LiTaO3," *Biosensors & BIoelectronics* vol. 19, pp. 849-859, 2004.

[16] J. Xu*, et al.*, "Angular dependence of surface acoustic wave characteristics in AlN thin films on a-plane sapphire substrates," *Applied Physics A,* vol. 83, pp. 411-415, 2006.

[17] G. Hu*, et al.*, "Digital phase detection approach and its application for AlN dual-mode differential surface acoustic wave sensing," *Sensors and Actuators B,* vol. 132, pp. 272-279, 2008.

[18] C. Caliendo*, et al.*, "K+ detection using shear horizontal acoustic modes," in *IEEE Ultrasonics Symposium Proceedings*, Honolulu, HI, USA, 1990, pp. 383-387.

[19] J. Enderlein*, et al.*, "Mass sensitivity of temperature-stabilized surface acousitc wave delay lines on GaAs," *sensors and Actuators B: Chemical,* vol. 24, pp. 65-68, 1995.

[20] C. Caliendo*, et al.*, "Surface acoustic wave humidity sensor," *Sensors and Actuators B,* vol. 15, pp. 288-292, 1993.

[21] M. Penza and V. I. Anisimkin, "Surface acoutic wave humidity sensor using polyvinyl-alcohol film," *Sensors and Actuators A,* vol. 76, pp. 162-166, 1999.

[22] M. R. Risch, "Precision pressure sensor using quartz SAW resonators," *sensors and Actuators,* vol. 6, pp. 127-133, 1984.

[23] Q. Jiang*, et al.*, "Analysis of surface acoustic wave pressure sensors " *Sensors and Actuators A,* vol. 118, pp. 1-5, 2005.

[24] D. Hauden*, et al.*, "Temperature sensor using SAW delay line," in *IEEE ultrasonics symposium*, 1981, pp. 148-151.

[25] L. Rayleigh, "On waves propagating along the plane surface of an elastic solid," in *London Math. Soc.*, 1885, pp. 4-11.

[26] R. Weigel*, et al.*, "Microwave acoustic materials, devices and applications," *IEEE Transactions on microwave theory and techniques,* vol. 50, pp. 738-749, 2002.

[27] G. Lippman, "Principe de la conservation de l'electricite (in French)," *Annales de chimie et de physique,* vol. 24, p. 145, 1881.

[28] R. White and F. Voltmer, "Direct piezoelectric coupling to surface elastic waves," *Applied Physics Letters,,* vol. 7, pp. 314-316, 1965.

[29] E. A. Ash and E. G. S. Paige, *Rayleigh-Wave theory and application*. New York: Springer-Verg, 1985.

[30] H. Wohltjen and R. Dessy, "Surface acousitc wave probe for chemical analysis " *Anal. Chem.,* vol. 51, pp. 1458-1475, 1979.

[31] C. S. Lam, "A review of the recent development of temperature stable cuts of quartz for SAW applications," *J. Ningbo Univ. (NSEE),* vol. 17, pp. 117-123, 2004.

[32] Y. Kobayashi*, et al.*, "1.9-GHz-Band surface acoustic wave devie using second leaky mode on LiTaO3," *Jpn. J. Appl. Phys.,* vol. 35, pp. 2987-2990, 1996.

[33] S. S. Lee and R. M. White, "Piezoelectric cantilever acoustic transducer," *J. Micromech. Microeng.,* vol. 8, pp. 230-238, 1998.

[34] M. E. Motamedi and R. M. White, *Acoustic Sensors in Semiconductor Sensors*. New York: Wiley, 1994.

[35] Q. Wang, *Micromachined ultrasonic transducers with piezoelectric AlN thin films*. Detroit: Wayne State University Ph. D. Thesis, 2005.

[36] T. Suetsugu*, et al.*, "AlN epitaxial growth on atomically flat initaly nitrided a-Al_2O_3 wafer," *Applied surface Science,* vol. 117/118, pp. 540-545, 1997.

[37] K. Tsubouchi and N. Mikoshiba, "Zero-Temperature-Coefficient SAW Devices on AlN Epitaxial Films," *IEEE Transactions on Sonics and Ultrasonics,* vol. SU-32, pp. 634-644, 1985.

[38] E. F. Mccullen*, et al.*, "Electrical characterization of Metal/AlN/Si thin film hydrogen sensors with Pd and Al gates," *Journal of Applied Physics,* vol. 93, pp. 5757-5762, 2003.

[39] F. Serina*, et al.*, "Pa/AlN/SiC thin film devices for selective hydrogen sensing," *Applied Physics Letters,* vol. 79, pp. 3350-3352, 2001.

[40] B. G. Streetman and S. Banerjee, *Solid State Electronic Devices (5th ed.)*. New Jersey: Prentice Hall, 2000.

[41] *Band Gap*. Available: http://en.wikipedia.org/wiki/band_gap

[42] Y. V. Danylyuk, *Growth and characterization of AlN, InN, Al1-xInxN semiconductors films and nanostructures*. Detroit: Wayne State University Ph. D. Thesis, 2005.

[43] M. E. Levinshtein*, et al.*, *Properties of advanced semiconductor materials: GaN, AlN, InN, BN, and SiGe*. New York: John Wiley and Sons, 2001.

[44] J. H. Edgar, Ed., *Properties of group III nitrides*. London: Inspec, IEE, 1994, p.^pp. Pages.

[45] (2011, *Aluminum Nitride Property*. Available: http://www.ioffe.ru/SVA/NSM/Semicond/AlN/mechanic.html

[46] S. Datta, *Acoustic surface wave devices*. Eaglewood Cliffs, NJ: Prentice-Hall, 1986.

[47] O. Ambacher, "Growth and applications of group III-nitrides," *Journal of Physics D: Applied Physics,* vol. 31, pp. 2653-2710, 1998.

[48] N. W. Ashcroft and N. D. Mermin, *Solid State Physics*. New York: Brooks Cole, 1976.

[49] J. Xu, *AlN thin film based acoustic wave sensors for biosensing applications*. Detroit: Wayne State University Ph. D. Thesis, 2006.

[50] N. Grandjean and J. Massies, "GaN and $Al_xGa_{1-x}N$ molecular beam epitaxy monitored by reflection high-energy electron diffraction," *Applied Physics Letters,,* vol. 71, pp. 1816-1818, 1997.

[51] M. A. Megahed and S. M. El-Ghazaly, "Analysis of anisotropic planar structures on high temperature superconductor sapphire anisotropic substrates," *IEEE Transactions on Microwave Theory and Techniques,* vol. 43, pp. 1989-1992, 1995.

[52] R. A. Serway and J. W. Jewett, *Principles of physics: a calculus-based text*: Thomson Brooks, 2005.

[53] D. I. Anderson, "Elastic wave propagation in layered anisotropic media," *Journal of Geophysical Research* vol. 66, pp. 2953-2963, 1961.

[54] G. Fischerauer*, et al.*, "Design of mobile phone IIDT-type SAW filters with block-like distribution of transducers," *IEEE Transactions on Microwave Theory and Techniques,* vol. 42, pp. 1380-1386, 1994.

[55] K.-y. Hashimoto and M. Yamaguchi, "Delta function model analysis of SSBW spurious response in SAW devices," in *IEEE International Frequency Control Symposium*, 1993, pp. 639-644.

[56] B. Boulet, *Fundamentals of signals and systems*. Boston, MA: Charles river media, 2006.

[57] V. Adams and A. Askenazi, *Building better products with finite element analysis*. Santa Fe, NM, USA: OnWord Press, 1999.

[58] G. E. Dieter, *Mechanical Metallurgy*. New york: McGraw-Hill, 1989.

[59] A. A. Kaufman and A. L. Levshin, *Acoustic and elastic wave fields in geophysics III*. Amsterdam, Netherlands: Elsevier, 2000.

[60] B. A. Auld, *Acoustic fields and waves in solids*. New York: Wieley, 1973.

[61] G. E. Mase, *Continuum mechanics*. New York: McGraw-Hill, 1970.

[62] G. T. Mase and G. E. Mase, *Continuum Mechanics for Engineer*. Boca Raton: CRC Press, 1999.

[63] J. D. N. Cheeke, *Fundamental and applications of ultrasonic waves*. Boca Raton, Fiorida: CRC Press, 2002.

[64] D. Royer and E. Dieulesaint, *Elastic waves in solids*. Berlin, German: Springer, 1996.

[65] K.-y. Hashimoto, *Surface acoustic wave devices in telecommunications*. Berlin: Springer, 2000.

[66] L. D. Landau and E. M. Lifshitz, *Theory of elasticity*. New York Pergamon, 1986.

[67] M. J. Turner*, et al.*, "Stiffness and deflection analysis of complex structures," *Journal of Aeronautical Sciences,* vol. 23, pp. 805-824, 1956.

[68] R. W. Clough, "The finite element method in plane stress analysis," presented at the Second ASCE Conference on Electronic Computation, Pittsburgh, PA, 1960.

[69] J. H. Argyris and S. Kelsey, "Energy theorems and structural analysis," *Aircraft Engineering,* vol. 26 and 27, 1955.

[70] S. S. Rao, *The finite element method in engineering*. Burlington, MA, USA: Elsevier Butterworth-Heinemann, 2005.

[71] O. C. Zienkiewic, "The finite element method: From intuition to generality," *Applied Mechanics Reviews,* vol. 23, pp. 249-256, 1970.

[72] C. G. Armstrong, "Special issue: automatic mesh generation," *Advances in Engineering Software,* vol. 13, pp. 217-337, 1991.

[73] J. E. Akin, *Finite elements for analysis and design*. London: Academic Press, 1994.

[74] P. L. George, *Automatic generation of meshes*. New York: Wiley, 1991.

[75] E. R. Arantes and E. Olivera, "Theoretical foundations of the finite element method," *International Jouranl of Solids and Structures,* vol. 4, pp. 929-952, 1968.

[76] R. L. Taylor, "On completeness of shape functions for finite element analysis," *International Jouranl of Numerical Methods in Engineering,* vol. 4, pp. 17-22, 1972.

[77] S. Kalantar-zadeh*, et al.*, "Simulation of a Love mode surface acoustic wave transducer," in *IEEE Ultrasonics Symposium*, Caesars Tahoe, Nevada USA, 1999, pp. 161-164.

[78] S. D. Yu, "Simulation of surface acoustic wave devices," *IEEE Transactions on Ultrasonics, Ferroelectrics, and Frequency control,* vol. 51, pp. 616-623, 2004.

[79] G. Tobolka, "Mixed matrix representation of SAW transducers," *IEEE Transactions on Sonics and Ultrasonics,* vol. SU-26, pp. 426-428, 1979.

[80] D. P. Chen and H. A. Haus, "Analysis of metal-strip SAW grating and transducers," *IEEE Transactions on Sonics and Ultrasonics,* vol. SU-26, 1985.

[81] K. Wong and W. Tam, "Analysis of the frequency response of SAW filters using finite-difference time-domain method," *IEEE Trans. Microwave. Theory,* vol. 53, pp. 3364-3370, 2005.

[82] L. P. Derbesse*, et al.*, "2-D unstructured simulation of acoustic scattering phenomena," in *IEEE Ultrasonics symposium*, San Juan, Puerto Rico, 2000, pp. 573-576.

[83] G. Seriani and E. Priolo, "Spectral element method for acoustic wave simulation in heterogeneous media," *Finite Elements in Analysis and Design,* vol. 16, pp. 337-348, 1994.

[84] A. H.-D. Cheng and D. T. Cheng, "Heritage and early history of the boundary element method," *Engineering Analysis with Boundary Elements* vol. 29, pp. 268-302, 2005.

[85] M. M. EL Gowini and W. A. Moussa, "A reduced three dimensional model for SAW sensors using finite element analysis," *Sensors,* vol. 9, pp. 9945-9964, 2009.

[86] P. Ventura*, et al.*, "A new efficiency combined FEM and periodic green's functions formalism for the analysis of periodic SAW structures," in *IEEE Ultrasonics Symp.*, 1995, pp. 263-268.

[87] Baghai-Wadjii*, et al.*, "Green's function applications in SAW devices," in *IEEE Ultrasonics Symp.*, 1991, p. 11.

[88] P. Ventura*, et al.*, "Numerical methods for SAW propagation characterization," in *IEEE Ultrasonics Symposium*, 1998, pp. 175-186.

[89] M. Mayer*, et al.*, "Analysis of acoustomigration and acoustic loss in SAW filters employing FEM/BEM," in *IEEE Ultrasonics Symposium*, Rotterdam, Netherlands, 2005, pp. 450-454.

[90] K. J. Gamble and D. C. Malocha, "Simulation of short LSAW transducers including electrode mass loading and finite finger resistance," *IEEE Transactions on Ultrasonics, Ferroelectrics, and Frequency control,* vol. 49, pp. 47-56, 2002.

[91] K. Hashimoto*, et al.*, "Fast analysis of SAW propagation under multi-electrode type gratings with finite thickness," in *IEEE Ultrasonics symposium*, Toronto, Canada, 1997, pp. 279-284.

[92] J. Lin*, et al.*, "Fast, precise and full extraction of the COM parameters for multi-electrode-type gratings by periodic green's function method," *IEEE Transactions on Ultrasonics, Ferroelectrics, and Frequency control.,* vol. 49, pp. 1735-1738, 2002.

[93] P. Ventura and W. Steichen, "FEM/BEM analysis of a generalized periodic array," *IEEE Transactions on Ultrasonics, Ferroelectrics, and Frequency control,* vol. 54, pp. 2052-2059, 2007.

[94] T. D. Kenny*, et al.*, "FEM/BEM impedance and power analysis for measured LGS SH-SAW devices," presented at the 2004 IEEE International Ultrasonics, Ferroelectrics and Frequency Control 50th Anniversary Conference, Montreal, Canada, 2004.

[95] M. Hofer*, et al.*, "Finite element simulation of bulk- and surface acoustic wave (SAW) interaction in SAW devices," in *IEEE Ultrasonics Symposium*, Munich, German, 2002, pp. 53-56.

[96] M. Hofer*, et al.*, "Finite-element simulation of wave propagation in periodic piezoelectric SAW structures," *IEEE Transactions on Ultrasonics, Ferroelectrics, and Frequency control,* vol. 53, pp. 1192-1201, 2006.

[97] L. L. Brizoual and O. Elmazria, "FEM modeling of AlN/diamond surface acoustic waves devices," *Diamond & Related Materials,* vol. 16, pp. 987-990, 2007.

[98] J. Heikkila*, et al.*, "3D simulations of difference frequency effects on a blood vessel in ultrsound-stimulated vibro-acoustography," presented at the 2004 IEEE Ultrasonics Symposium, Montreal, Canada, 2004.

[99] O. Hikino*, et al.*, "Diffraction simulation of SAW filters using SAW source distribution," in *IEEE ultrasonics symposium*, San Antonio, TX, USA, 1996, pp. 159-163.

[100] M. M. EL Gowini and W. A. Moussa, "A finite element model of a MEMs-based surface acoustic wave hydrogen sensor," *Sensors,* vol. 10, pp. 1232-1250, 2010.

[101] M. Z. Atashbar*, et al.*, "3D FE simulation of H2 SAW gas sensor," *Sensors and Actuators B,* vol. 111-112, pp. 213-218, 2005.

[102] A. L'Etang and Z. Huang, "FE simulation of laser generated surface acoustic wave propagation in skin," *Ultrasonics,* vol. 44, pp. 1243-1247, 2006.

[103] J. Wang*, et al.*, "Numerical simulation of laser-generated ultrasound in non-metallic material by the finite element method," *Optics & Laser Technology,* vol. 39, pp. 806-813, 2006.

[104] J. Wang*, et al.*, "Simulation on thermoelastic stress field and laser ultrasound waveform in non-metallic materials by using FEM," *Applied Physics A,* vol. 84, pp. 301-307, 2006.

[105] M. Emam, "Finite element analysis of composite piezoelectric beam using comsol," Master of Science, Mechanical Engineering, Drexel University, 2008.

[106] G. Scheerschmidt*, et al.*, "Finite element analysis of resonant frequencies in surface acoustic wave devices," in *COMSOL Users Conference*, Birmingham, 2006.

[107] S. J. Ippolito*, et al.*, "A finite element approach for 3-dimensional simulation of layered acoustic wave transducers," in *Conference n Optoelectronic and Microelectronic Materials and Devices*, 2002, pp. 541-544.

[108] S. Krishnamurthy*, et al.*, "3D modeling and simulation of SH-SAW devices using the finite element method," presented at the IEEE sensors 2007 conference, Atlanta, Georgia, USA, 2007.

[109] S. Harma and V. P. Plessky, "Extraction of frequency-dependent reflection, transimission, and scattering parameters for short metal reflectors from FEM-BEM simulations," *IEEE Transactions on Ultrasonics, Ferroelectrics, and Frequency control.,* vol. 55, pp. 883-889, 2008.

[110] Gvrtrade, "FEMSAW-An expremely accurate and powerful 2D FEM/BEM simulation tool for SAW devices," ed.

[111] P. Ventura*, et al.*, "The effect of the fabrication process in propagation and reflectivity in an IDT," in *IEEE ultrasonics symposium*, San Antonio, TX, USA, 1996, pp. 281-284.

[112] G. Bu*, et al.*, "Surface acoustic wave velocity in single-crystal AlN substrates," *IEEE Transactions on Ultrasonics, ferroelectrics and frequency control,* vol. 53, pp. 251-254, 2006.

[113] E. Ruiz*, et al.*, "Electronic structure and properties of AlN," *Phys. Rev. B.,* vol. 49, pp. 7115-7123, 1994.

[114] K. Shimada*, et al.*, "First-principles study on electronic and elastic properties of BN, AlN, and GaN," *J. Appl. Phys.,* vol. 84, pp. 4951-4958, 1998.

[115] A. F. Wright, "Elastic properties of zinc-blende and wurzite AlN, GaN, and InN," *J. Appl. Phys.,* vol. 82, pp. 2833-2839, 1997.

[116] R. Kato and J. Hama, "First-principles calculation of the elastic stiffness tensor of aluminiumnitride under high pressure," *J. Phys. Condens. Matter,* vol. 6, pp. 7617-7632, 1994.

[117] K. Kim*, et al.*, "Elastic constants and related properties of tetrahedrally bonded BN, AlN, GaN, and InN," *Phys. Rev. B.,* vol. 53, pp. 16310-16326, 1996.

[118] S. V. Davydov, "Evaluation of physical parameters for the group III nitrates: BN, AlN, GaN and InN," *Semiconductors* vol. 36, pp. 41-44, 2002.

[119] L. E. McNeil*, et al.*, "Vibratioal spectroscopy of aluminum nitride " *J. Amer. Ceram. Soc.,* vol. 76, pp. 1132-1136, 1993.

[120] C. Deger*, et al.*, "Sound velocity of $Al_xGa_{1-x}N$ thin films obtained by surface acoustic-wave measurements," *Appl. Phys. Lett.,* vol. 72, pp. 240-2402, 1998.

[121] K. Tsubouchi*, et al.*, "AlN material constants evaluation and SAW properties on AlN/Al_2O_3 and AlN/Si," in *IEEE Ultrason. Symp.*, 1981, pp. 375-380.

[122] G. Carlotti*, et al.*, "The elastic constants of sputtered aluminum nitride films," in *IEEE Ultrason. Symp.*, 1995, pp. 353-356.

[123] A. Kampfe*, et al.*, "X-ray and single crystal values of the elastic constants and determination of machining residual stresses in AlN," *High Temperature Material Processes,* vol. 2, pp. 309-326, 1998.

[124] G. Bu*, et al.*, "Electromechanical coupling coefficient for surface acoustic waves in single crystal, bulk aluminum nitride," *Appl. Phys. Lett.,* vol. 84, pp. 4611-4613, 2004.

[125] A. J. Noreika*, et al.*, "Dielectric properties of reactively sputtered films of aluminum nitride," *J. Vac. Sci. Technol.,* vol. 6, pp. 194-197, 1969.

[126] G. A. Slack and T. F. McNelly, "Growth of high purity AlN crystals," *J. Crystal Growth,* vol. 34, pp. 263-279, 1976.

[127] R. Smith*, et al.*, "Analysis of interdigital surface wave transducers by use of an equivalent circuit model," *IEEE Trans. Microwave Theory Tech. ,* vol. MTT-17, pp. 856-864, 1969.

[128] B. A. Auld, *Acoustic Fields and Waves in Solids* vol. II. New York: Wiley, 1973.

[129] (2011, *Sapphire*. Available: http://www.mt-berlin.com/frames_cryst/descriptions/sapphire.htm

[130] T. C.-T. Ting, *Anisotropic Elasticity: Theory and Applications*: Oxford University Press, 1996.

[131] A. N. Norris, "Euler-Rodrigues and Cayley formulas for rotation of elasticity tensors," *Mathematics and Mechanics of Solids,* vol. 13, pp. 465-498, 2008.

[132] N. U. Piezoelectric device laboratory. Available: http://piezo.nbu.edu.cn/crystal/classes/CrystalConstrant.html

[133] G. Xu and Q. Jiang, "A finite element analysis of second order effects on the frequency response of a SAW device," *J. Intel. Mat. Syst. Struct.,* vol. 12, pp. 69-77, 2001.

[134] S. J. Ippolito*, et al.*, "A finite-element analysis for simulation of layered SAW devices with XY LiNbO$_3$ substrate " in *Smart Structures, Devices and Systems*, Melbourne, Australia, 2002, pp. 120-131.

[135] COMSOL, *COMSOL 4.1 Documentations*, 2011.

[136] M. I. Rocha-Gaso*, et al.*, "Mass sensitivity evaluation of a love wave sensor using the 3D finite element method," in *IEEE International Frequency Control Symposium*, 2010, pp. 228-231.

[137] S. Zhgoon*, et al.*, "3D finite element modeling of real size SAW devices and experimental validation," in *IEEE International Ultrasonics Symposium*, 2008, pp. 1932-1935.

[138] F. Briegleb and A. Geuther, "About MgN and the affinity of nitrogen gas with metals," *Ann. Chem.,* vol. 123, p. 228, 1862.

[139] H. Funk and H. Boehland, "Zur darstellung von metallnitride aus ammoniumfluoromethallaten und ammoniak," *Z. Anorg. Allgem. Chem,* vol. 334, pp. 155-162, 1964.

[140] H. Isobe*, et al.*, "Synthesis of AlN Grains and Liquid-Phase-Epitaxy (LPE) Growth of AlN Films Using Sn-Ca Mixed Flux," *Japanese Journal of Applied Physics Part 2: letters,* vol. 44, pp. L488-L490, 2005.

[141] B. Abdallah*, et al.*, "Deposition of AlN films by reactive sputtering: Effect of radiofrequency substrate bias," *Thin solid films,* vol. 515, pp. 7105-7108, 2007.

[142] B. Abdallah*, et al.*, "Thickness and substrate effects on AlN thin film growth at room temperature," *EPJ Applied Physics,* vol. 43, pp. 309-313, 2008.

[143] R. D. Vispute*, et al.*, "Pulsed laser deposition: a novel growth technique for wide-bandgap semiconductor research," *Silicon Carbide and Related Materials -1999 PTS, Material Science Forum,* vol. 338-3, pp. 1503-1506, 2000.

[144] R. D. Vispute*, et al.*, "High quality optoelectronic grade epitaxial AlN films on alpha-Al_2O_3, Si and 6H-SiC by pulsed laser deposition," *Thin solid films,* vol. 299, pp. 94-103, 1997.

[145] K. Dovidenko*, et al.*, "Aluminum nitride films on different orientations of sapphire and silicon," *Journal of Applied Physics,* vol. 79, pp. 2439-2445, 1996.

[146] R. D. Vispute*, et al.*, "Pulsed laser deposition and processing of wide band gap semiconductors and related materials," *Journal of Electronic Materials,* vol. 28, pp. 275-286, 1999.

[147] Y. G. Roman and A. P. M. Adriaansen, "Aluminium nitride films made by low pressure chemical vapour deposition: Preparation and properties," *Thin solid films,* vol. 169, pp. 241-248, 1989.

[148] W. Hageman*, et al.*, "Growth of AlN n etched 6H-Sic (0001) substrates via MOCVD," *physica Status Solidi A,* vol. 188, pp. 783-787, 2001.

[149] T. Shibata*, et al.*, "AlN epitaxial growth on off-angle R-plane sapphire substrates by MOCVD," *Journal of Crystal Growth,* vol. 229, pp. 63-68, 2001.

[150] Y. Taniyasu and M. Kasu, "MOVPE growth of single-crystal hexagonal AlN on cubic diamond," *Journal of Crystal Growth,* vol. 311, pp. 2825-2830, 2009.

[151] S. B. Thapa*, et al.*, "Structural and spectroscopic properties of AlN layers grown by MOVPE," *Journal of Crystal Growth,* vol. 298, pp. 383-386, 2007.

[152] N. Grandjean and J. Massies, "Real time control of $In_xGa_{1-x}N$ molecular beam epitaxy growth," *Applied Physics Letters,,* vol. 72, pp. 1078-1080, 1998.

[153] J. Smalc-Koziorowska*, et al.*, "Mismatch relaxation by stacking fault formation of AlN islands in AlGaN/GaN structures on m-plane GaN substrates," *Applied Physics Letters,* vol. 99, p. 061901, 2011.

[154] V. Mansurov*, et al.*, "Reflection high energy electron diffraction investigation and comparison of the initial stage during molecular beam epitaxy of AlN on Si (111) and Si (110) substrates," *Journal of Vacuum Science & Technology B,* vol. 29, p. 03c129, 2011.

[155] S. Mikrouli*, et al.*, "Control of the polarity of molecular-beam epitaxy grown GaN thin films by the surface nitridation of Al2O3 (0001) substrates," *Applied Physics Letters,* vol. 80, pp. 2886-2888, 2002.

[156] I. Gherasoiu*, et al.*, "Growth mechanism of AlN by metal-organic molecular beam epitaxy," *Journal of Applied Physics,* vol. 96, pp. 6272-6276, 2004.

[157] F. S. Ohuchi and P. E. Russell, "AlN thin-films with controlled crystallography orientations and their microstructure," *Journal of Vacuum science & Technology a-Vacuum surfaces and Films,* vol. 5, pp. 1630-1634, 1987.

[158] C. R. Aita, "Basal orientation aluminum nitride grown at low temperature by RF diode sputtering," *Journal of Applied Physics,* vol. 53, pp. 1807-1808, 1982.

[159] G. W. Auner*, et al.*, "Epitaxial growth of wide bandgap semiconductors by plasma source molecular beam epitaxy," presented at the Diamond and Related Materials V: GaN and Related Materials, San Jose, CA, 1995.

[160] J. A. Thornton, "Magnetron sputtering: basic physics and application to cylindrical magnetrons.," *J. Vac. Sci. Technol.,* vol. 15, pp. 171-177, 1978.

[161] G. W. Auner*, et al.*, "Epitaxial growth of AlN by plasma source molecular beam epitaxy," in *wide band gap electronic materials*, ed Dordrecht: Kluwer, 1995, pp. 329-334.

[162] P. Zatyko, *Plasma source molecular beam epitaxy*. Detroit: Wayne State University Master Thesis, 1998.

[163] L. W. Rosenberger, *Modification and characterization of aluminum nitride surfaces for an acoustic wave biosensor*. Detroit: Wayne State University, Ph. D. Thesis, 2007.

[164] H. R. Kaufman and R. S. Robinson, *Operation of broad beam ion sources*. Alexandria, Virginia: Commonwealth Scientific, 1987.

[165] H. Conrads and M. Schmidt, "Plasma generation and plasma sources," *Plasma Sources Sci. Technol.,* vol. 9, pp. 441-454, 2000.

[166] C. Horwitz, "Hollow cathode reactive sputter etching- A new high-rate process," *Applied Physics Letters,* vol. 43, pp. 977-979, 1983.

[167] A. V. Crewe*, et al.*, "A high resolution scanning transmission electron microscope," *Journal of Applied Physics,* vol. 39, pp. 5861-5868, 1968.

[168] D. L. Spears and H. I. Smith, "High-resolution pattern replication using soft x-rays," *Electron Letters,* vol. 8, pp. 102-104, 1972.

[169] H. I. Smith*, et al.*, "X-ray lithography: A complementary technique to electron beam lithography," *J. Vac. Sci. Technol.,* vol. 10, pp. 913-917, 1973.

[170] H. I. Smith, "Fabrication techniques for surface-acoustic-wave and thin-film optical devices," in *Proceedings of the IEEE*, 1974, pp. 1361-1387.

[171] R. C. Jaeger, *Introduction to microelectronic fabrication*. Upper Saddle river: Prentice Hall, 2002.

[172] D. Daly, *Microlens Arrays*. London: Taylor & Francis, 2001.

[173] R. E. Tibbets and J. S. Wilczynski, "High performance reduction lenses for microelectronic circuit fabrication," *IBM J. Res. Devel.,* vol. 13, pp. 192-196, 1969.

[174] H. J. Schuetze and K. E. Hennings, "Large-area masking with patterns of micron and submicron element size," *SCP and Solid State Technol.,* vol. 9, pp. 31-35, 1966.

[175] A. Bahr, "Fabrication techniques for surface-acoustic-wave devices," in *Proc. Int. specialists Seminar on Component Performance and Systems Applications of Surface Acoustic Wave Devices*, Aviemore, Scotland, 1973, pp. 22-23.

[176] N. K. Sheridon, "Production of blazed holograms," *Applied Physics Letters,,* vol. 12, pp. 316-318, 1968.

[177] M. J. Beesley and J. G. Castledine, "The use of photoresist as a holographic recording medium," *Appl. Opt.,* vol. 9, pp. 2720-2724, 1970.

[178] D. Monsma and I. Applebaum, "A reliable lift-off process," Harvard University, Marcuslab2002.

[179] H. I. Smith*, et al.*, "A high yield photolithographic technique for surface wave devices," *J. Electrochem Soc.,* vol. 118, pp. 821-825, 1971.

[180] A. Pohl, "A review of wireless SAW sensors," *IEEE Trans. Ultrasonics, Ferroelectrics and Frequency Control,* vol. 47, pp. 317-332, 2000.

[181] E. O. Brigham, *The Fast Fourier Transform*. New York: Prentice-Hall, 2002.

[182] J. Schoukens*, et al.*, "The interpolated fast Fourier transform: a comparative study," *IEEE Transactions on instrumentation and measurement,* vol. 41, pp. 226-232, 1992.

[183] C. Offelli and D. Petri, "Interpolation techniques for real-time multifrequency waveform analysis," *IEEE Transactions on Instrumentation and Measurement,* vol. 39, pp. 106-111, 1990.

[184] V. Friedman, "A zero crossing algorithm for the estimation of the frequency of a single sinusoid in white noise " *IEEE Transactions on Signal Processing,* vol. 42, pp. 1565-1569, 1994.

[185] R. Pintelon and J. Schoukens, "An improved sine-wave fitting procedure for characterizing data acquisition channels," *IEEE Trans. on Instrumentation and Measurement,* vol. 45, pp. 588-593, 1996.

[186] A. Routray*, et al.*, "A novel Kalman filter for frequency estimation of distorted signals in power systems," *IEEE Trans. on Instrumentation and Measurement,* vol. 51, pp. 469-479, 2002.

[187] M. Aiello*, et al.*, "A chirp-z transform-based synchronizer for power system measurements," *IEEE Trans. on Instrumentation and Measurement,* vol. 54, pp. 1025-1032, 2005.

[188] H. K. Kwok and D. L. Jones, "Improved instantaneous frequency estimation using an adaptive short-time Fourier transform," *IEEE Trans. on Signal Processing,* vol. 48, pp. 2964-2972, 2000.

[189] P. M. Ramos and A. C. Serra, "Comparison of frequency estimation algorithms for power quality assessment," *Measurement,* vol. 42, pp. 1312-1317, 2009.

[190] K. S. Kao*, et al.*, "The characteristics of surface acoustic waves on AlN/LiNbO3 substrates," *Applied Physics A: Materials Science & Processing,* vol. 76, pp. 1125-1127, 2002.

[191] R. K. Roy, *Design of Experiments Using the Taguchi Approach: 16 Steps to Product and Process Improvement*. New York: John Wiley & Sons Inc, 2001.

[192] I. N. Vucchkov and L. N. Boyadjieva, *Quality Improvement with Design of Experiments: A Response surface Approach*. Dordrecht: Kluwer Academic Publishers, 2001.

[193] J. L. Rosa*, et al.*, "Electrodeposition of copper on titanium wires: Taguchi experimental design approach," *Journal of Materials Processing Technology,* vol. 209, pp. 1181-1188, 2009.

[194] D. Systemes. (2011, *Isight*. Available: http://www.simulia.com/products/isight.html

[195] G. J. Klir and B. Yuan, *Fuzzy Sets and Fuzzy Logic, Theory and Applications*. Upper Saddle River, NJ: Prentice Hall, 1995.

[196] R. O. Duda*, et al.*, *Pattern Classification*. New York: John Wiley & Sons Inc, 2001.

[197] C. M. Bishop, *Pattern Recognition and Machine Learning*. New York: Springer, 2006.

[198] E. Candes and M. Wakin. (2008) An introduction to compressive sampling. *IEEE Signal Processing Magazine*. 21-30.

[199] R. Baraniuk. (2007) Compressive sensing. *IEEE Signal Processing Magazine*. 118-121.

[200] S. Bhattacharya and T. Basar, "Sparsity based feedback design: a new paradigm in opportunistic sensing," in *American control conference*, 2011, pp. 3704-3709.

[201] J. Y. Lee*, et al.*, "Effects of buffer layer annealing on ZnO thin films grown by using atomic layer deposition," *Journal of the Korean Physical Society,* vol. 55, pp. 2556-2559, 2009.

ABSTRACT

DESIGN AND FABRICATION OF A PROTOTYPE ALUMINUM NITRIDE-BASED PRESSURE SENSOR WITH FINITE ELEMENT ANALYSIS AND VALIDATION

by

XINYU DU

May 2012

Advisors: Dr. Hao Ying and Dr. Gregory Auner

Major: Electrical Engineering

Degree: Doctor of Philosophy

Since 1985 when the first robot PUMA 560 was employed to place a needle during a brain CT biopsy, surgical robots have become ubiquitous in clinical surgeries. Despite its advantages and success in surgeries, the interactions between the robot and the surgeons remain deficient, especially for the pressure sensing which plays an important role. Inspired by our previous work on bacterial sensing, in the current work I have designed, fabricated, analyzed, and evaluated an innovative prototype pressure sensor based on Aluminum Nitride (AlN) Surface Acoustic Wave (SAW) and Shear Horizontal (SH)-SAW. This AlN-based device has unique superiorities over other SAW devices, including relatively lower cost, higher sensitivity, intrinsically higher reliability, more compact size, and faster response. In this novel design a sandwich-like structure is adopted and the AlN thin film on the top is used as the insulated layer to make the device applicable in aqueous environment. The delta function analysis and structural mechanics analysis have been performed to validate the proposed design scheme qualitatively. So as to make a quantitative and comprehensive analysis, the numerical computational analysis using finite element method (FEM) has been carried out using

the software package COMSOL Multiphysics®. The 2D plane-strain simulation and 3D simplified model simulation have been executed to analyze the device performance with or without insulator. A good agreement has been achieved between the simulation and the experimental measurements, which validates the design scheme and establishes the effectiveness of the device. This SAW/SH-SAW device has been fabricated in the WSU SSIM clean room. The crystalline AlN thin film is deposited on A-plane sapphire with 2 μm thickness using the PSMBE system. The aluminum interdigital transducer (IDT) is evaporated on the AlN thin film with predefined delay-line pattern using the BJD-1800 vacuum deposition system. Another layer of AlN thin film with 1 μm thickness is deposited on the top of the IDT area with some customized masks to make the device insulated.

Furthermore, the differential frequency measurement system has been set up using electronic components to evaluate the system. Several signal processing algorithms are developed and compared to acquire system output. The thermal stability of the differential system is also studied and temperature compensation is developed to improve system robustness. The portable electrical circuit involving the frequency measurement system is finally designed and evaluated. Such a sensor could serve as a key component in artificial skin or be equipped on the end of a surgical robotic arm in the future.

AUTOBIOGRAPHICAL STATEMENT

Xinyu Du

Education

07/2001, B.S. Automation Department, Tsinghua University, Beijing, China

07/2004, M.S. Automation Department, Tsinghua University, Beijing, China

Professional Experience

05/2010—Now Lead Project Engineer in Electrical and Control Integration Lab, General Motors Co., Warren, MI (contract with Kelly Services and Patni Inc.)

09/2007—04/2010 Graduate Teaching Assistant, ECE Department, Wayne State University, Detroit, MI.

09/2004—08/2007 Graduate Research Assistant, ECE Department, Wayne State University, Detroit, MI.

Honors and Awards

1. Ralph H. Kummler Award for Distinguished Achievement in Graduate Student Research, Wayne State University 2010
2. Outstanding Teaching Assistant Service Award, Wayne State University 2010
3. Travel award for excellence in graduate student research, Wayne State University, 2005, 2008
4. Best Student Paper Award finalist, the 24th North American Fuzzy Information Processing Society Conference, Ann Arbor, MI, June 22-25, 2005.

Publications

3 Journal Papers and 9 Conference Papers were published during Ph. D. Studies